THERMAL TRANSPORT IN TWO-DIMENSIONAL AND WIDE BAND GAP MATERIALS

A DISSERTATION

SUBMITTED TO THE DEPARTMENT OF

ELECTRICAL ENGINEERING

AND THE COMMITTEE ON GRADUATE STUDIES

OF STANFORD UNIVERSITY

IN PARTIAL FULFILLMENT OF THE REQUIREMENTS

FOR THE DEGREE OF

DOCTOR OF PHILOSOPHY

Runjie (Lily) Xu
August 2020

This dissertation is online at: http://purl.stanford.edu/sj080yf2289

I certify that I have read this dissertation and that, in my opinion, it is fully adequate in scope and quality as a dissertation for the degree of Doctor of Philosophy.

Eric Pop, Primary Adviser

I certify that I have read this dissertation and that, in my opinion, it is fully adequate in scope and quality as a dissertation for the degree of Doctor of Philosophy.

Srabanti Chowdhury

I certify that I have read this dissertation and that, in my opinion, it is fully adequate in scope and quality as a dissertation for the degree of Doctor of Philosophy.

Krishna Saraswat

Approved for the Stanford University Committee on Graduate Studies.

Stacey F. Bent, Vice Provost for Graduate Education

This signature page was generated electronically upon submission of this dissertation in electronic format. An original signed hard copy of the signature page is on file in University Archives.

Abstract

The semiconductor industry has seen much interest in materials beyond silicon. Among these, two-dimensional (2D) nanomaterials are known to exhibit distinct evolution of chemical and physical properties as the material thickness is scaled from bulk to atomic layers. Wide band gap (WBG) materials have also attracted attention due to their promising applications in power electronics and short wavelength photonics.

This work begins by summarizing the thermal properties of 2D materials, including thermal conductivity, thermal boundary conductance, and thermoelectric properties.

We then study thermal and electrical transport in WTe_2, which is a semimetallic 2D material. Thermal properties of WTe_2 devices are extracted from the device electrical characteristics using an analytical model. We also use finite element simulations to estimate the current density improvements by novel heat dissipation structures, including capping layers such as hexagonal boron nitride (h-BN). This work demonstrates that WTe_2 can carry high current density despite its low thermal conductivity, which shows its potential applications as a thermal barrier or electrode in phase-change memory.

Next, we discuss thermal conductivity of crystalline AlN and the influence of atomic-scale defects. AlN plays a key role in modern power electronics and deep-ultraviolet photonics. In these devices, heat dissipation is important during high-power and high-temperature operation. Using the 3ω characterization method, we measure temperature dependent thermal conductivity of AlN single crystals, between 100 and 400 K. Experimental data are compared with analytical models. We also investigate size effects and accumulated thermal conductivity of AlN thin films, which are widely used as buffer layer or capping layer in power electronic devices or light-emitting diodes. This work improves the understanding of AlN thermal conductivity and demonstrates how this material influences heat dissipation in wide band gap devices.

We also study the temperature reduction of GaN devices with polycrystalline diamond top capping layer by Raman thermometry. Experimental results are compared with an analytical model and finite element simulations. These results provide a fundamental understanding of how to improve heat dissipation in GaN transistors.

Combined, these studies shed light into the fundamental thermal properties of 2D and WBG materials. In addition, these results also serve as the foundations to design 2D and WBG devices and systems with better heat dissipation capabilities.

To my family

Acknowledgements

First, I would like to thank my advisor Prof. Eric Pop. I am extremely grateful for the opportunity to work in Eric's group. Eric is my mentor not only in Ph.D. research but also in my personal growth. I have also developed my writing and presentation skills under his guidance.

I would like to thank Prof. Debdeep Jena (DJ) and Prof. Huili (Grace) Xing from Cornell University. I did summer research in DJ's group in 2013 when they were at University of Notre Dame. They guided me to do research when I had zero experience. I also collaborated with DJ and Grace's students for my AlN project. They have always been very supportive.

I would like to thank Prof. Srabanti Chowdhury for the support and involvement in our collaborations. I would like to thank Prof. Krishna Saraswat, Prof. Roger Howe and Prof. Debbie Senesky for serving on my dissertation defense and reading committees. I am also very grateful for insightful advice from Prof. Yoshio Nishi, who was my co-advisor in my 1st year of Ph.D. study.

I want to express my gratitude to three colleagues in PopLab: Dr. Michal (Mike) Mleczko, Dr. Miguel Muñoz Rojo and Dr. Aditya Sood. I have worked closely with them and learned a lot from them.

I have had lots of discussion on theoretical models and simulations with Alex Gabourie, Cagil (Chuck) Koroglu, Dr. Feng Xiong and Dr. Zuanyi Li. I have received tremendous support on experiments from Victoria Chen, Michelle Chen and Dr. Feifei Lian.

To everyone in PopLab at Stanford: Dr. Eilam Yalon, Dr. Sam Vaziri, Stephanie Bohaichuk, Dr. Chris English, Dr. Ning Wang, Dr. Kirby Smithe, Dr. Saurabh Suryavanshi, Dr. Sanchit Deshmukh, Dr. Chris Neumann, Isha Datye, Connor McClellan, Connor Bailey, Ryan Grady, Kirstin Schauble, Asir Khan, Crystal Nattoo, Katie Neilson,

Mahnaz Islam, Sumaiya Wahid, Sebastian Fernandez, Jung-Soo Ko, Paul Walter, Andrew Yu, Dr. Yong Cheol Shin, Dr. Kevin Brenner, Dr. Alwin Daus, Bozo Vareskic, and our admin Chet Frost, it has been a pleasure working and hanging out with you guys.

I would like to acknowledge all my collaborators: Dr. S. M. Islam (Moudud) and Jonathan McCandless from Cornell University, Mohamadali Malakoutian from UC Davis, Prof. Natalio Mingo and Dr. Ankita Katre from LITEN, CEA-Grenoble, Dr. Michael Barako, Prof. Kenneth Goodson and Dr. Ananth Yalamarthy from Mechanical Engineering Department at Stanford.

I want to thank all my advisors and mentors before I came to Stanford. I want to thank Prof. Tian-Ling Ren and Prof. Zhiping Yu from Tsinghua University, Prof. Mildred Dresselhaus and Dr. Albert Liao from MIT, for your mentorship, your supports and your wisdom. Prof. Dresselhaus passed away three years ago, but she is always been my role model. She is the inspiration for several generations of researchers and scientists.

I want to thank all my friends for their support and all those memorable wine tastings in Napa Valley.

To my tuxedo cat Jojo, whom I adopted two months before my graduation, I love your overloaded cuteness.

To my parents, grandparents, aunts, uncles and cousins, I could not finish my Ph.D. study without your love and support. I would also like to give special acknowledgement to my younger cousin Isabelle. We grew up together, learnt together and now we are pursuing Ph.D. degrees together.

Table of Contents

List of Tables

List of Figures

Chapter 1

Introduction

This chapter introduces the thermal limitations of semiconductor materials and devices. We discuss the fundamental physics of thermal transport and thermal properties. We also discuss various thermal measurement methodologies to study different materials and devices.

1.1   Limitations of Moore's Law Scaling

Electronic devices are components for controlling the flow of electrical currents for the purpose of information processing and system control, including transistors and diodes. Integrated circuits (ICs) are built with billions of transistors. Moore's Law observed that the number of transistors of an IC doubles approximately every two years, for the previous five decades.[1] Although dimension scaling appears to have slowed down, transistor numbers in integrated circuits are still growing. The resulting improvements in performance are more gradual than the speed-ups resulting from frequency increases. The primary reason for the breakdown of dimension scaling is that at small sizes, current leakage causes greater challenges, and also causes the chip to heat up, which increases energy costs and lead to potential failure.

1.2   Thermal Transport

Understanding the fundamental limitations of Moore's Law has become increasingly important and thermal limitation is one of them. Thermal limitation depends on how

much power is allowed for a system (or chip's) operation, and how much increase in temperature the chip can stand. The thermal limitation also depends on how fast heat is removed away from the chip.

High temperature in integrated circuits should be avoided because of several reasons. First, material properties degrade at high temperature. For example: mobility of both electrons and holes decrease significantly when temperature is increasing, because electron and hole scattering increases at high temperature (shown in Figure 1.1(a)).[2]
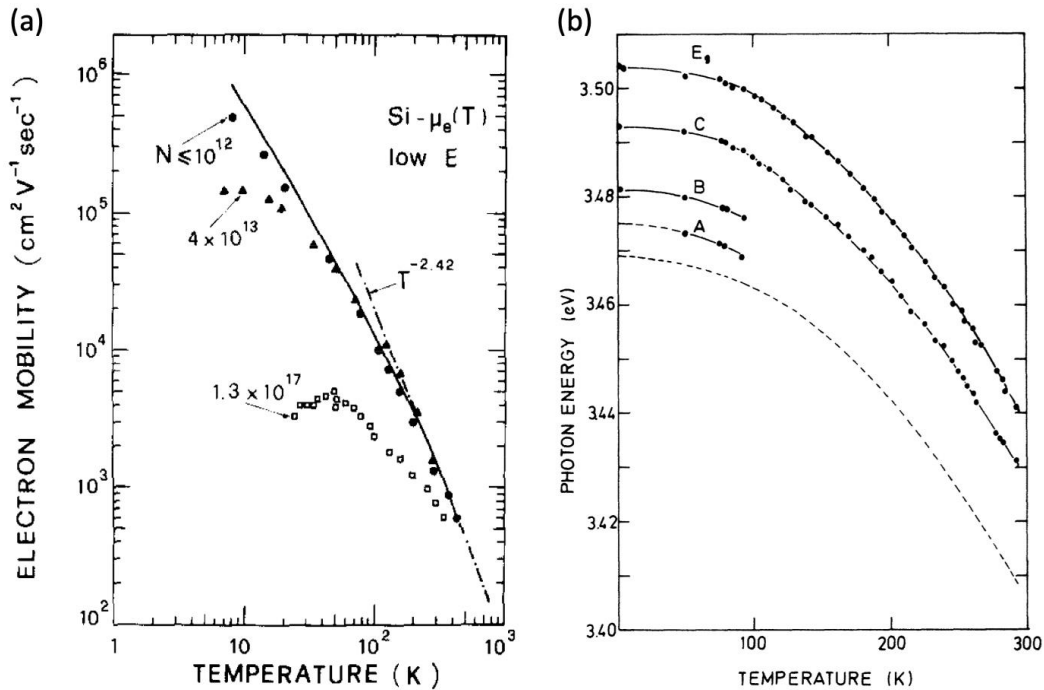
Figure 1.1. (a) Si electron mobility versus temperature. Figure reproduced after Ref. 1. (b) GaN band gap versus temperature. Figure reproduced after Ref. 2.

Band gaps also decrease when temperatures increase (shown in Figure 1.1(b)).[3] For example: GaN is a direct band gap semiconductor which is commonly used in blue light-emitting diodes (LEDs) and other optoelectronic devices.[4,5] When those devices are under operation, the temperature increases because of Joule heating, which leads to band gap

2

reduction. Therefore, there is a shift in the output wavelength of the laser, which causes undesired changes in device properties. In transistors, leakage current increases exponentially as the temperature increases, which decreases their on/off ratio and causes additional power consumption.[6] The reliability of semiconductor devices and interconnects is also related to temperature. Mean time to failure (MTTF) decreases exponentially as temperature increases, described by Arrhenius relationship as:[7]

$$\text{MTTF}(T) = A e^{\frac{E_a}{k_B T}} \tag{1.1}$$

where A is a non-thermal constant, E_a is an activation energy, k_B is the Boltzmann constant, and T is the absolute temperature.

Other properties also change with temperature, such as mechanical failure due to thermal expansion which causes unevenly distributed stress in the device and leads to mechanical breakdown.

1.2.1 Thermal Conductivity

Thermal conduction has become very important in micro- and nano-scale materials and devices. As the dimension of those materials become comparable to the mean free paths (MFP) of different energy carriers, it is crucial to understand the carrier interactions and how they affect thermal conductivities.

In a crystalline material, phonons, which are quantized lattice vibrations, play an important role in heat conduction. In electrically conductive materials, such as metals,

electrons dominate heat conduction. The electronic thermal conductivity (k_e) is related to the electrical conductivity by the Wiedemann-Franz Law (WFL):

$$k_e = \sigma L T \tag{1.2}$$

where σ is the electrical conductivity, L is the Lorenz number and T is the temperature. For most metals, the Lorenz number is approximately the same,[8] which is around $L \approx 2.45 \times 10^{-8}$ WΩ/K^2. In heavily doped semiconductors, electronic thermal conductivity also plays an important contribution to the total thermal conductivity.

Figure 1.2 shows thermal conductivities of some crystalline materials and amorphous materials from 1 K to 1000 K, and Figure 1.3 shows the most relevant scattering mechanisms: phonon-phonon scattering, boundary scattering which is significant in thin films, and defect scattering. For three-dimensional (3D) materials, the thermal conductivity can be described as $k \approx \frac{1}{3} C v \lambda$, where C is specific heat, v is the average phonon velocity, λ is the phonon MFP.[9] At low temperature, k increases with temperature because C rises as $\sim T^{d/n}$, where d is the dimension (e.g. $d = 3$ for a three-dimensional material) and n is the exponent in the phonon dispersion (frequency $\omega \propto q^n$, where q is the phonon wave vector).[8,10] At higher temperature the heat capacity is a constant (approaching the Dulong-Petit limit), so the temperature dependence of the MFP dominates. Therefore, for crystalline materials, their thermal conductivity values decrease at high temperature because of phonon-phonon scattering.
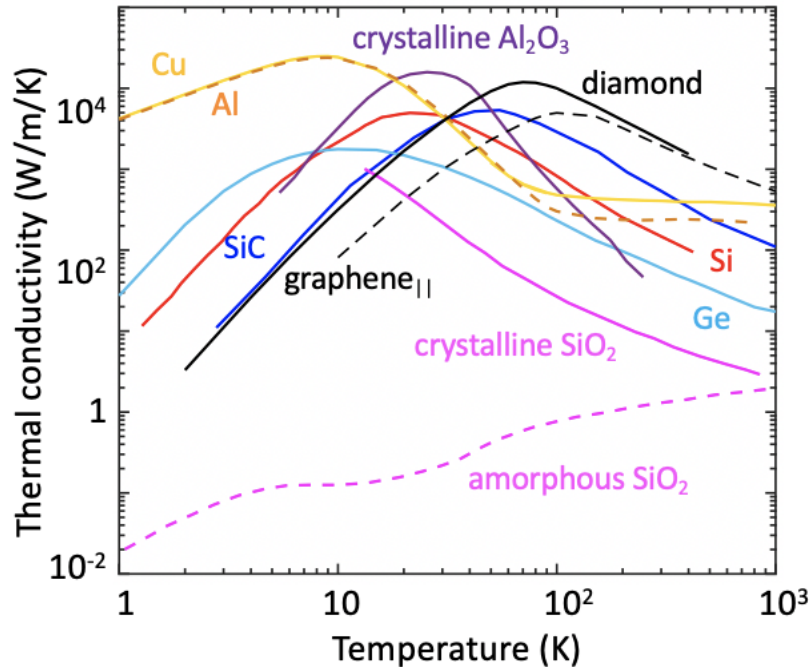
Figure 1.2. Temperature dependent thermal conductivity of several common materials, including Cu, Al, Al$_2$O$_3$, SiO$_2$, crystalline Si, Ge, diamond and graphene.[11]
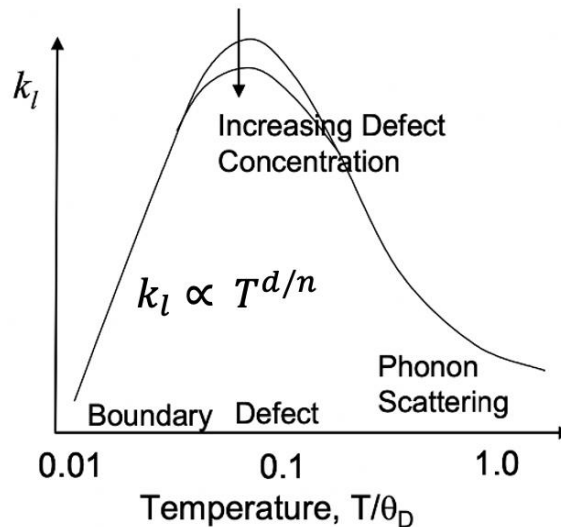
Figure 1.3. Thermal conductivity versus temperature for crystalline materials, including the effects of specific heat, boundary scattering, defect scattering and phonon scattering. The temperature axis is normalized with respect to the Debye temperature, Θ_D.[9,10]

1.2.2 Thermal Boundary Conductance

Thermal boundary conductance (TBC) is a property indicating the ability to conduct heat across the interface of two solids in intimate contact. The TBC often plays an important

role in calculating total thermal resistance of nanoscale devices. The thermal boundary

resistance (TBR = 1/TBC) is the inverse of the TBC.
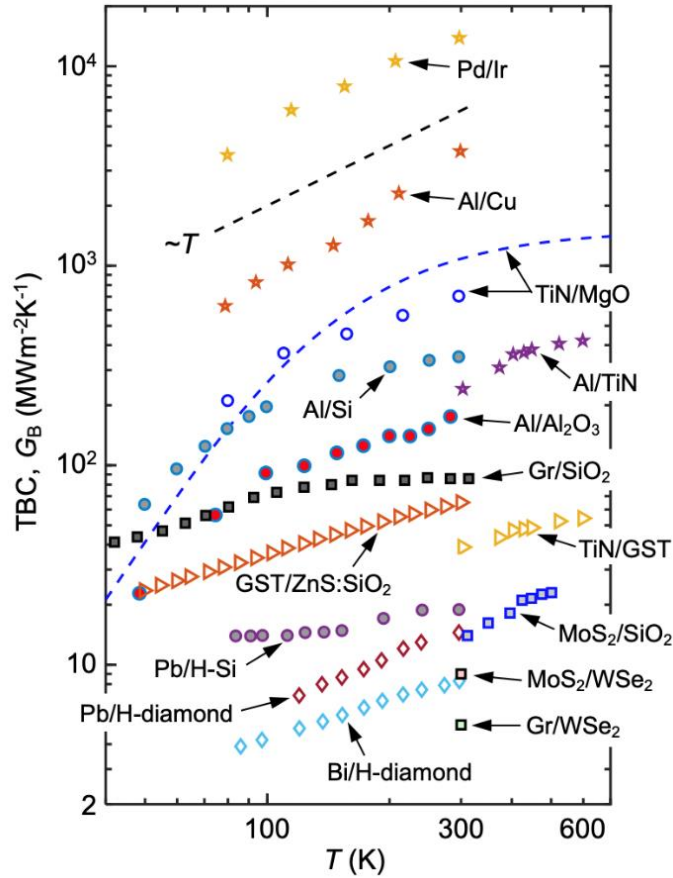
Figure 1.4. Temperature dependent thermal boundary conductance across various material interfaces. Black dashed line is ~T trend. Blue dashed line is Diffuse Mismatch Model for TiN/MgO, which is the upper limit of phonon-mediated TBC. The two highest data sets are electron-mediated metal-metal interfaces, all others are phonon-mediated. Figure reproduced after Ref.12, with recent updates (courtesy Eric Pop, unpublished).

Temperature dependent TBC values of many different interfaces[12] are shown in Figure

1.4. Higher TBC value indicates better heat conduction between two materials. Upper

limit is represented by the interfaces between metals, for example: Pd – Ir and Al – Cu

interfaces. Metal interfaces have higher TBC values because thermal transport across

these interfaces is mediated by high densities of electrons. Small TBC values are due to

large Debye temperature mismatches, imperfect surfaces or contamination (trapped liquid or air) at the interfaces. In practice, a quantity known as the Kapitza length is often used to describe what a TBC value corresponds to, in term of a thin film material thickness. For example: the TBC between monolayer MoS_2 and SiO_2 is equivalent to a Kapitza length ~90 nm of SiO_2 at room temperature,[13] and the TBC between AlN and Al corresponds to a Kapitza length ~2.2 µm of AlN at room temperature.[14] This highlights the importance of the temperature drops at dissimilar material interfaces, especially in nano- and microscale films and devices.

1.3 Thermal Limitations in Semiconductors

Different applications require different thermal properties. For example, heat sinks and heat spreaders need high thermal conductivity and large TBC. A Si substrate is usually a good heat sink, its thermal conductivity is from 100 to 140 $Wm^{-1}K^{-1}$ at room temperature, depending on doping.[15-17] SiC is widely used as a substrate in power electronics, it also has very high thermal conductivity. Crystalline diamond has a very high thermal conductivity above 2000 $Wm^{-1}K^{-1}$ at room temperature.[15] It becomes very popular to be used as substrates or capping layers in power electronic devices, but the disadvantage is the high cost to grow this material. On the other hands, low thermal conductivity and small TBC are good for heating purposes, for example: thermoelectric devices or thermal confinement in phase change memory.[18]

1.3.1 Thermal Limitations in Two-Dimensional Materials and Devices

Two dimensional (2D) materials have a wide range of band gaps (shown in Figure 1.5).[19] h-BN is usually considered an excellent electrical insulator. Semiconductors includes MoS_2, WSe_2 and etc. WTe_2 is a semimetal, which is a material with a very small overlap between the bottom of the conduction band and the top of the valence band. Graphene is also a semimetal, although in graphene the conduction and valence bands "touch" at a single point, known as the Dirac point.
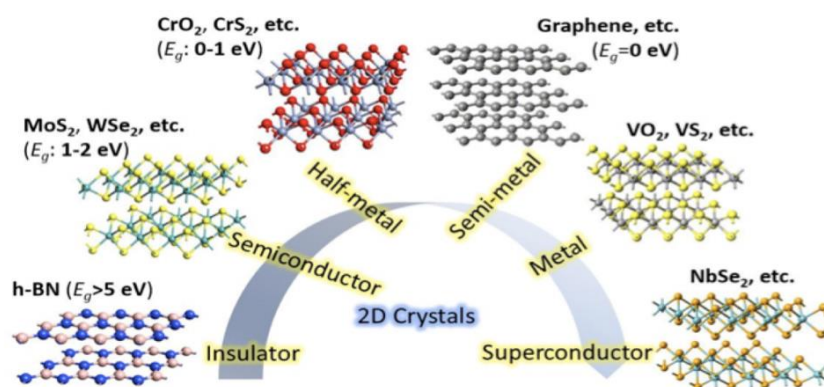
Figure 1.5. Various types of 2D materials from insulator to superconductor. Figure reproduced after Ref. 19.

One of the areas of focus in this dissertation is on the thermal properties of WTe_2. WTe_2 is the heaviest group 6 dichalcogenide (shown in Figure 1.6),[20] which leads to its low thermal conductivity. WTe_2 is a single-layer semimetal, it is unusual in nature. It could be potentially used as very thin electrodes in 2D material devices. Since WTe_2 could be used as electrodes instead of traditional metal contacts such as gold or Al or Cu, it is important to study its maximum current density, thermal properties and its breakdown behavior.

Figure 1.6. Periodic Table. Tungsten and tellurium are in red circles, which shows WTe_2 is the heaviest group 6 dichalcogenide. Figure reproduced after Ref. 20.

1.3.2 Thermal Limitations in Wide Band Gap Materials and Devices

Wide band gap materials (WBGs) often include GaN, Ga_2O_3, AlN, and BN. GaN is a well-known III-V semiconductor with 3.4 eV band gap.[21,22] Ga_2O_3 has a 4.9 eV band gap, and high-voltage transistors have been recently demonstrated with this material.[99] BN is a well-known electrical insulator, which is often used as dielectric layer in 2D devices.[23] AlN has a very large band gap, 6.2 eV.[24,25]

Wide band gap materials have potential applications in power electronics and optoelectronics. One of the applications is in short wavelength optoelectronics (shown in Figure 1.7), such as LEDs and lasers. The output wavelength is related to the band gap, thus wide band gap materials can be used to obtain shorter wavelength. For example: blue LED made from GaN, an advancement which received the Nobel Prize in 2014.[26]
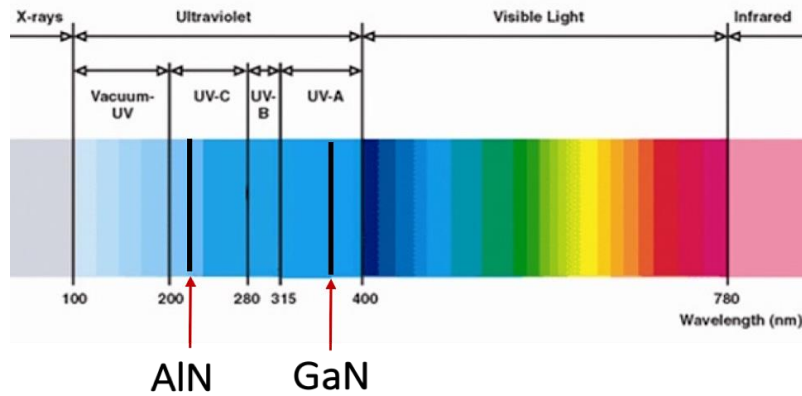
Figure 1.7. Light spectrum. AlN and GaN have band gaps in the ultraviolet regime.

Another very important application is GaN high electron mobility transistors (HEMT).

Figure 1.8(a) shows the device structure. Typical substrates include Si, SiC and sapphire.

SiC has high thermal conductivity but it is expensive. Sapphire is a cheaper material but

has smaller thermal conductivity (details in Section 4.1). Figure 1.8(b) shows the band

diagram between GaN layer and AlGaN layer. Two-dimensional electron gas (2DEG)

forms near the interface in the GaN layer.
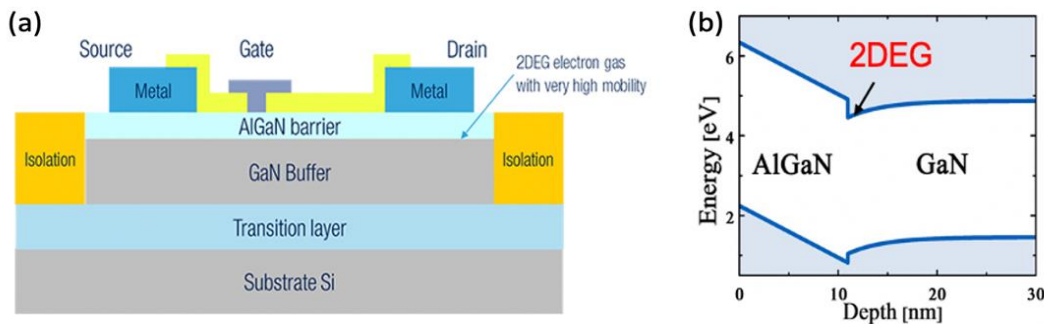
Figure 1.8. (a) Schematic of a GaN HEMT deivce. (b) Band alignment between AlGaN and GaN interface.

For GaN power electronics, high power and high voltage are applied onto these devices,

which lead to significant Joule heating. Therefore, it is very important to understand

thermal properties and heat dissipation in those devices. Also, in WBG optoelectronics,

heating leads to band gap reduction, which will cause wavelength shift. Thus, efficient heat sinks and heat spreaders are crucial.

1.4 Hierarchy of Measurement Methodologies

In the context of electronics, there is often no direct way to measure heat conduction or temperature, unlike electrical properties. Thus, all thermal measurements rely on measuring properties that change with temperature. To measure thermal conductivity, input power and temperature difference across the sample should be known. Thermal conductivity can be extracted based on Fourier Law of heat conduction:

$$Q = -k\Delta T \qquad (1.3)$$

where Q is the heat flux per unit area, k is the thermal conductivity of the material, and T is the temperature. Thermocouples can be used to measure temperatures of large samples, but for micro- and nano-scale samples, these present many difficulties.

Thermal measurement metrology can be classified into two general categories, optical methods and electrical methods. Figure 1.9 shows several examples of thermal measurement methods. There are several trade-offs between those measurement techniques. For example, a complex measurement setup such as Raman thermometry or 3ω measurement can be used on easily fabricated samples. On the other hand, complex heater and sensor lines need to be fabricated on the samples for simple measurements which only require multimeters and a power supply.

1.4.1 Optical Methods

Figure 1.9(a) shows a thermoreflectance measurement structure.[27] A reflective metal is used in this technique as the thermometer due to its temperature-dependent reflectance. A known power laser is used to heat up the metal surface and a probe laser is used to measure the change of reflectance of the metal. The time-dependent temperature decay is used to extract the thermal conductivity of the sample underneath the metal pad.
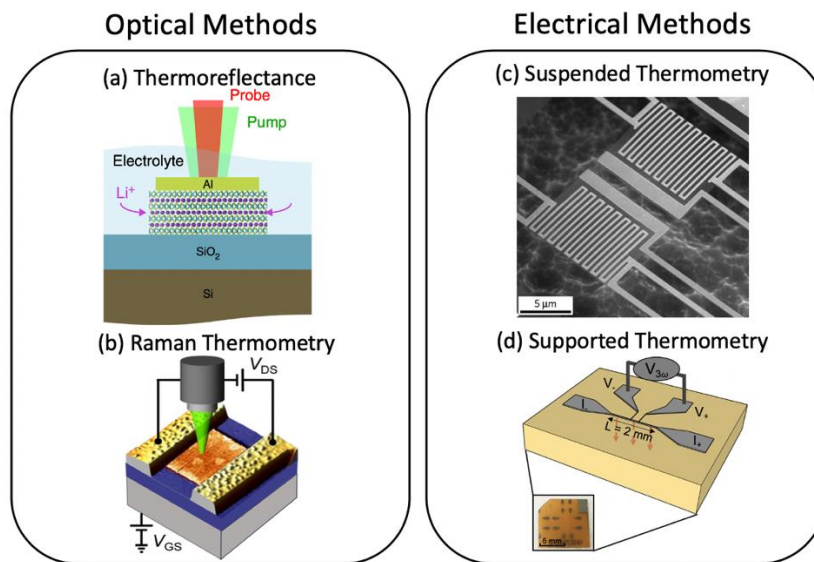
Figure 1.9. Thermal and thermoelectric measurement methods. (a) Thermoreflectance uses a laser to probe temperature changes in the cross-plane direction through changes in metal reflectance.[27,28] (b) Raman thermometry uses spectroscopic shifts to calculate temperature changes.[29] (c) Suspended electrical thermometry platform utilizes 1D heat conduction in the lateral direction to measure thermal properties.[30] (d) Supported thermometry can use steady-state and AC methods to probe lateral and cross-plane heat flow.[31, 14]

However, there is an additional interface between the metal pad and the sample, extra efforts are needed to subtract the contribution from this additional interface in order to extract the intrinsic thermal properties of the sample. This method is also not ideal to measure a complex device structure since this additional metal pads may cause undesired changes to the electrical properties of the devices.

A Raman thermometry schematic is shown in Figure 1.9(b).[32] When light interacts with atoms, the light can be scattered by the atomic vibrations. Most scattered light has the same frequency as the incident light, but some fraction of light has different frequencies due to interaction between incoming photons and the atomic vibrations of the sample. This phenomenon that the light is scattered with frequency change is called Raman scattering. When the scattered frequency is smaller than that of the incident light (due to phonon emission), it is called Stokes scattering. When scattered frequency is larger, it is called anti-Stokes (phonon absorption). Because this frequency modulation is specific to molecular vibrations and phonons in crystal, it is possible to analyze composition of material or crystal lattice information by analyzing spectrum of Raman scattered light. There are two main methods to extract temperature from Raman spectrum. The first one is to use peak position. At higher temperature, peaks shift to shorter wave numbers.[33] The second method is to use the ratio between anti-Stokes and Stokes peak to calculate temperature.[34]

Raman thermometry is a non-contact optical method and it does not require additional metals on the sample. It is often used to measure devices that are self-heated or heated by the Raman laser. One of the most important trade-offs is the spatial resolution, which corresponds to the diffraction limit of the laser, around 500 nm. Also, this method cannot be used on samples without Raman signal for a given laser wavelength.

1.4.2 Electrical Methods

Electrical methods can be broken down into two main categories, suspended and supported thermometry. Electrical methods use the changes in electrical resistance with temperature to extract temperature information of the samples. For suspended method (shown in Figure 1.9(c)), since the sample is not in contact with any substrate, there is no heat loss into the substrate that need to be subtracted.[30] However, a suspended thermal measurement structure is more difficult to fabricate than a supported platform. For a supported platform (shown in Figure 1.9(d)), more efforts are used to subtract the contribution of heat conduction into the substrate.[14, 31] Heat loss to the substrate is significant, especially for the samples on high thermal conductivity substrates (e.g. a silicon wafer). The large heat sinking substrate is useful for cross-plane thermal measurements (e.g. 3ω method). Most of the electrical techniques do not require complex system, but calibration is very important and difficult. Compared to optical methods, electrical methods cannot be used to measure spatial changes of thermal properties.

Each thermal measurement has its own advantages and disadvantages. Understanding how to select the optimal method based on the material properties and device structures is very important.

1.5 Organization and Scope of Work

Chapter 1 motivates the importance to study thermal properties including thermal conductivity and thermal boundary resistance in 2D materials and WBGs. This

dissertation will highlight the thermal study of one 2D material (WTe_2), and two WBGs (AlN and GaN). It will also summarize the thermal properties of 2D materials.

Chapter 2 reviews the thermal properties of 2D materials. Those thermal properties include thermal conductivity, TBC and thermoelectric property (Seebeck coefficient).

Chapter 3 examines the maximum current density, thermal properties, and breakdown behavior of WTe_2. To accomplish this, we use both analytical model and finite element simulation to compare with experimental I-V data. We discover that WTe_2 has larger maximum current density than Cu or Al interconnect and it has very low thermal conductivity due to its large molecular mass.

Chapter 4 discusses the fundamental thermal properties of AlN and how atomic defects affect its thermal conductivity. We will show how 3ω electro-thermal method works in this chapter. We use 3ω method to measure the temperature dependent thermal conductivity from 100 K to 400 K of single crystalline AlN samples. We also use a complex analytical model, which includes several scattering mechanisms to compare with experimental results.

Chapter 5 discusses the temperature reduction of GaN devices with polycrystalline diamond capping layer. Raman thermometry is used to monitor the temperatures, and simulations are used to compare with experimental results.

Chapter 6 summarizes the main contribution this dissertation. We discuss the future

directions of thermal studies of 2D materials and wide band gap materials.

Chapter 2

Thermal and Thermoelectric Properties of Two-dimensional Materials

Two-dimensional (2D) layered materials, including graphene, boron nitride, and transition metal dichalcogenides (TMDs), have attracted much interest for their unusual attributes and potential applications. In this chapter, we review recent progress as well as historical data of thermal and thermoelectric properties of such materials, from atomically thin (<1 nm) monolayers to bulk. Their bulk thermal conductivity is highly anisotropic, 10-300 times larger along the atomic layer planes than across them. In monolayers, the thermal conductivity could be reduced by interactions with adjacent materials due to scattering of phonons. The thermal interfaces of such materials are also poor heat conductors due to weak van der Waals interactions and, especially for TMDs, heavy atomic masses. The molar heat capacity is also higher in the TMDs with heavier atomic masses (e.g. WTe_2 rather than MoS_2) below room temperature. The thermopower (Seebeck coefficient) depends strongly on temperature and doping, being moderate (~50 µV/K) in semimetallic graphene, but very high (~1 mV/K) in TMDs with large band gaps at room temperature. This review also highlights much experimental data that is missing, particularly in the atomically thin limit (monolayer or few-layer) of TMDs, and such knowledge gaps could guide future research.

2.1 Introduction

Layered two-dimensional (2D) materials consist of sub-nanometer thin layers (the thickness of one to three atoms) characterized by strong in-plane covalent bonds, while the individual layers are held together by weak, cross-plane van der Waals interactions. These materials include graphite, hexagonal boron nitride (h-BN), black phosphorus (BP), and transition metal dichalcogenides (TMDs) like MoS_2, and it is their bonding anisotropy that ultimately leads to their unusual thermal properties. The atomically thin planes can "slide" over each other and, in bulk form, such layered materials have been used in lubricants (graphite, MoS_2)[35] and writing instruments (graphite)[36] for hundreds of years.

The term "2D material" typically applies to the single (mono-) layer separated from the bulk material, although few-layered samples (e.g. 2-5 layers) have also been often referred to as "2D". Single- or few-layer samples were originally separated as small (~10 μm) flakes from the bulk by mechanical exfoliation (e.g. with adhesive tape),[37] but have been more recently grown by chemical vapor deposition (CVD) as single layers over large (centimeter to meter) areas.[38,39]

2D materials present a unique set of physical, electrical, and thermal properties mostly derived from their layered nature and the weak, yet tunable, coupling between layers. Key properties include sub-nanometer thinness without dangling bonds, high and equal electron and hole mobility (graphene),[40] very high in-plane thermal conductivity (graphene, h-BN),[41] low cross-plane thermal conductivity (graphite, h-BN, MoS_2)[41,42]

and, in some cases, extremely low cross-plane thermal conductivity (comparable to air for disordered, layered WSe$_2$ or lower than air for layered, 2D heterostructures).[43,44] Some bulk layered materials such as WS$_2$ also have high Seebeck coefficient (> 500 µV/K),[45] yet many thermophysical properties remain unknown for individual monolayers. Perhaps more importantly, 2D materials span a very broad chemical space ranging from graphene and *h*-BN to TMDs with the form MX$_2$ (where M = transition metal; X = chalcogen).

2.2 Thermal Conductivity

The thermal conductivity (κ) of a material represents its ability to conduct heat. For diffusive thermal transport, when the size of the system is greater than the phonon mean free path (MFP), the heat flux is proportional to thermal conductivity and the temperature gradient, $Q = -\kappa \nabla T$. The thermal conductivity can be related to the specific heat, C, as $\kappa \approx (1/d)Cv\lambda$, where d is the dimension of the system, v is the properly averaged phonon group velocity, and λ is the MFP.[46,47] Furthermore, the thermal *conductance* is $G = \kappa A/L$ (and its inverse is the thermal resistance R_{th}), here written for an object of cross-sectional area, A, and length, L.

The analogy with electrical transport is quickly apparent: the temperature (in K) is analogous to voltage (in V), the thermal resistance (K/W) to the electrical resistance (Ω), and the heating power (in W) to current (in A). Similar to Ohm's Law ($\Delta V = IR$), the temperature rise of an object can be written as $\Delta T = PR_{th}$, where P is the heating power. Although it is tempting to assume that a material or device with large thermal conductivity (e.g. graphene) must have negligible temperature rise, this intuition often

fails when comparing devices with small dimensions as it is the *conductance* which must

be considered. The conductance of 2D devices can be very low. In addition, as we will

see, devices based on 2D materials are often limited by their interfaces, which is

quantified by their thermal boundary conductance (TBC) with the adjacent substrates or

contacts.

Nevertheless, since the thermal conductivity is an intrinsic material property, it is more

commonly used to describe and compare materials, while the thermal conductance

depends on dimensions and device geometry. Thus, in this section we summarize the

room-temperature thermal conductivities (in-plane and cross-plane) of several 2D

materials based on available experimental data, as shown in Figure 2.1. The data in

Figure 2.1 are shown as presently known ranges, with the understanding that these could

evolve as more studies become available. The upper end of these ranges is the most

crystalline material that has been measured, and the lower end corresponds to

polycrystalline or otherwise disordered samples.

2.2.1 In-Plane

Highly oriented pyrolytic graphite (HOPG) has room-temperature in-plane thermal

conductivity of $\kappa_{\parallel} \sim 300–2000$ Wm^{-1}K^{-1}, depending on its (poly)crystalline nature.[15,48]

The upper end of this range is comparable to the thermal conductivity of crystalline

diamond and among the highest of any known bulk material. Graphene is a single layer

of graphite and, due to its atomically thin nature, its thermal conductivity is strongly

dependent on the environment. Freely suspended graphene has $\kappa_{\parallel} \sim 1600 - 4000$ Wm^{-1}K^{-1}

due to its high phonon velocity, very long MFP ~250 - 600 nm, and lack of phonon scattering with adjacent layers.[41,49-51] (The upper end of this range corresponds to isotopically purified samples, with 0.01% ^{13}C instead of the 1.1% natural abundance.[52])

However, when graphene is supported by a substrate (e.g. SiO_2), its in-plane thermal conductivity is reduced to 600 - 700 $Wm^{-1}K^{-1}$ due to substrate scattering of phonons,[53-55] with phonon MFP of 100 nm.[41,49] If the top surface of graphene is also encased by SiO_2, phonons will suffer more scattering and the thermal conductivity is reduced to 80 - 400 $Wm^{-1}K^{-1}$,[56] depending on the number of layers. Moreover, when SiO_2-supported graphene is patterned into nanoribbons (GNRs), its thermal conductivity decreases to 40 - 220 $Wm^{-1}K^{-1}$ due to edge roughness scattering, and its value has a strong width-dependence.[57-59] These findings have demonstrated that the graphene thermal conductivity can be manipulated by its environment and dimensions. Nevertheless, since all these results were obtained for graphene on (or encased by) SiO_2, it is not yet known how other substrates (like SiN_x or h-BN) would affect its thermal conductivity.

The in-plane thermal conductivity of bulk h-BN is reported to be $\kappa_\parallel \approx 400$ $Wm^{-1}K^{-1}$ at room temperature,[48,60-62] and that of suspended and supported few-layer h-BN is 230 - 280 $Wm^{-1}K^{-1}$.[55,63-65] These values are smaller than those of graphite, which is presumably attributed to mass-difference (B vs. N) scattering and stronger phonon-phonon scattering in h-BN determined by phonon dispersion (i.e. shorter MFP). TMDs have yet smaller in-plane thermal conductivity than h-BN, due to smaller phonon group velocity and weaker covalent bonds, caused by heavier and larger constituent atoms. For example, the in-

plane thermal conductivity of bulk 2H-MoS_2 was found to be in the range $\kappa_\parallel = 74.3 - 110$ $Wm^{-1}K^{-1}$ for geologically-mined samples[48,66-68] and as low as 15 $Wm^{-1}K^{-1}$ for lab-grown samples.[69] Those of suspended mono- and few-layers are 13.3 - 84 $Wm^{-1}K^{-1}$ and 15.6 - 77 $Wm^{-1}K^{-1}$, respectively.[70-77] Similar to graphene, supported MoS_2 is expected to have lower thermal conductivity than suspended samples due to substrate scattering, and the measured values are 63 ± 22 $Wm^{-1}K^{-1}$ and 74 ± 10 $Wm^{-1}K^{-1}$ for mono and bilayer, respectively.[55] The apparent closeness of the supported thermal conductivity to the suspended may be a result of differing levels of crystal quality between studies.

Not unexpectedly, somewhat lower in-plane thermal conductivities were found in the heavier TMDs based on Mo and W, or Se and Te. Suspended mono- and bilayer WS_2 have thermal conductivity of 32 - 53 $Wm^{-1}K^{-1}$ at room temperature.[78] And bulk WS_2 has in-plane thermal conductivity around 120 - 124 $Wm^{-1}K^{-1}$.[68,79] For suspended and supported mono- or few-layer $MoSe_2$, its thermal conductivity range is $6.2 - 127$,[71,80,81] and 17 - 24 $Wm^{-1}K^{-1}$,[71] respectively with a bulk thermal conductivity measured to be between 20.3 - 30 $Wm^{-1}K^{-1}$.[55,82,83] Multiple studies show many-layer or bulk WSe_2[84,85] and WTe_2[86-89] samples to have comparable in-plane thermal conductivity, in the range of 1 - 15 $Wm^{-1}K^{-1}$,[68] ostensibly depending on sample quality and preparation, with the lower end of the range signaling larger disorder. However, two studies (from the same group) report measurements of bulk WSe_2 thermal conductivities to be between 40 - 42 $Wm^{-1}K^{-1}$.[68,89] The in-plane thermal conductivity of ReS_2 thick film is around 50 - 70 $Wm^{-1}K^{-1}$.[90] Notably, thermal conductivity data in the monolayer limit is presently

missing for the Se- and Te-based TMDs, no doubt in part due to their lack of environmental stability in such thin films.[86]

Another unusual layered 2D material of interest is black phosphorus (BP), with atomic structure as shown in Fig. 1d and 1h. Recent experiments have reported the in-plane thermal conductivity of BP flakes (ten to hundreds of nanometers thick) to be in the range of $\kappa_{\parallel,AC}$ = 6 to 36 Wm^{-1}K^{-1} in the armchair (AC) direction or $\kappa_{\parallel,ZZ}$ = 8 to 101 Wm^{-1}K^{-1} in the zigzag (ZZ) direction at room temperature,[91-103] and the value increases with thickness. Here too, the thinnest BP films are the least environmentally stable, thus the lowest end of this range was probably measured on partially amorphous or oxidized films. More importantly, the in-plane thermal conductivity of BP is anisotropic, which is also reflected in its phonon dispersion. The thermal conductivity anisotropy ratio between the zigzag and armchair direction is 1.5 to 2.[91-93,98,100-103]

2.2.2 Cross-Plane

The cross-plane thermal conductivity of 2D layered materials (as shown in Figure 2.1) is typically defined only in the bulk material. For monolayer samples, the quantity of interest for cross-plane thermal transport is the thermal boundary conductance (TBC), which is reviewed in the next section. The transition from monolayer to bulk behavior occurs in samples of thickness comparable to the MFP of the dominant phonons at a given temperature. Based on kinetic theory [42] and a phenomenological ballistic-diffusive model,[104] the MFP of cross-plane phonons is approximated to be ~10 nm., However, experiments show the MFP is of the order ~100 nm at room temperature for thin

graphitic[105,106] or MoS$_2$ films.[42] In other words, the cross-plane thermal conductivity of

thin graphitic or MoS$_2$ films is not a constant, but a function of the sample thickness,

from few nanometers thin up to ~0.5 µm thick.[42,105,106] The cross-plane transition to bulk

behavior in other layered 2D materials is not known today but, if MoS$_2$ and graphite

have a similar transition despite MoS$_2$ having heavier atomic masses, lower phonon

velocities, and generally a lower cross-plane thermal conductivity (Figure 2.1), other

TMDs, h-BN, and BP may also share the same behavior.
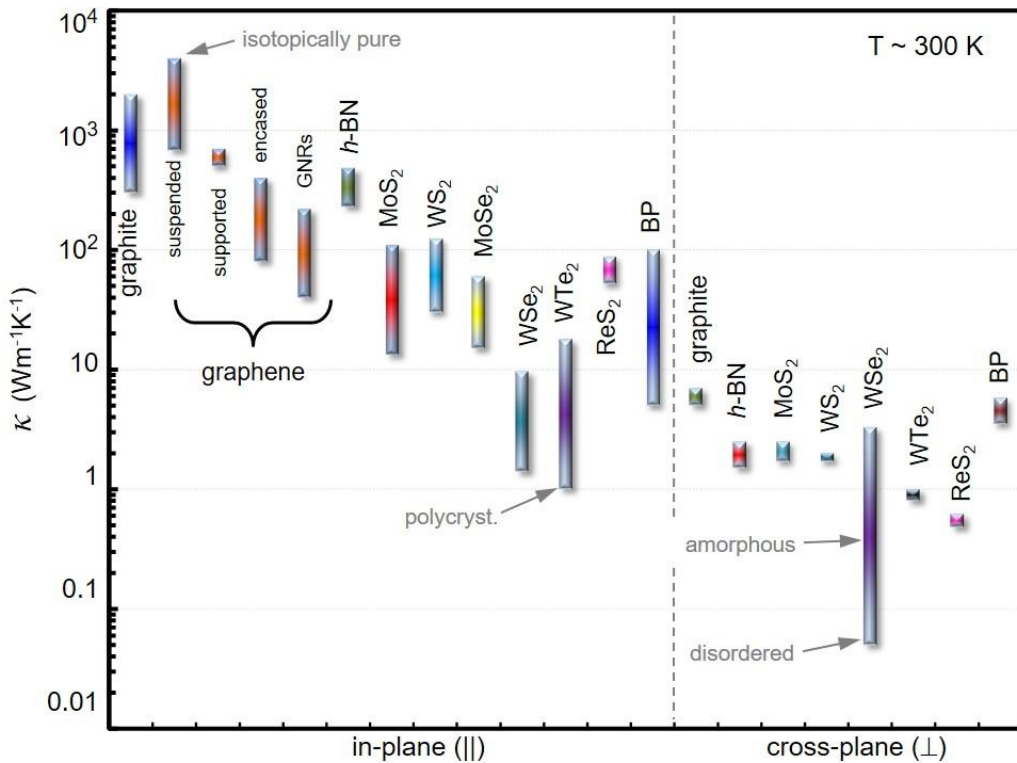
Figure 2.1. Measured room-temperature ranges of thermal conductivity κ for 2D materials, highlighting the strong in-plane vs. cross-plane anisotropy. In-plane thermal conductivity ranges are for graphite,[15] suspended graphene,[41,49-51] supported graphene,[53,54] encased graphene,[56] graphene nanoribbons (GNRs),[57-59] h-BN,[60,63-65] MoS$_2$,[66,70-74,107] WS$_2$,[78,79] MoSe$_2$,[71] WSe$_2$,[84,85] WTe$_2$,[86-88] and black phosphorus (BP).[91-97] Cross-plane thermal conductivity ranges are shown for bulk graphite,[15] h-BN,[108] MoS$_2$,[66,109] WSe$_2$,[43,109] ReS$_2$[90] and BP.[93,100] The lowest cross-plane thermal conductivity reported for disordered layered WSe$_2$ is about six times lower than the amorphous limit.[43] A few other special or limiting cases are pointed out by small arrows.

As previously mentioned, a unique attribute of layered 2D materials is their highly anisotropic nature, leading to a bulk cross-plane thermal conductivity $\kappa_\perp$ that is much lower (by orders of magnitude) than the in-plane thermal conductivity $\kappa_\parallel$. This behavior is due to much weaker cross-plane van der Waals interactions compared to the strong in-plane covalent bonds.

The presently known experimental data ranges of thermal conductivity in the cross-plane direction ($\kappa_\perp$) of several bulk 2D materials are shown in Figure 2.1. The accepted value for crystalline, HOPG is in the range of 5 to 7 Wm^{-1}K^{-1} at room temperature,[15,48] however the effective value of $\kappa_\perp$ is lower in films thinner than ~ 0.5 μm [52, 53] or in films with significant disorder. The cross-plane thermal conductivity of bulk h-BN is in the range $\kappa_\perp$ = 1.5 to 4.8 Wm^{-1}K^{-1},[48,61,62,108] that of 2H-MoS$_2$ is 1.7 to 5 Wm^{-1}K^{-1},[42,48,66-68,109] that of WS$_2$ is 1.7 to 2.8 Wm^{-1}K^{-1},[68,79] that of MoSe$_2$ is 1 to 2.6 Wm^{-1}K^{-1},[55,68] and that of black phosphorus is 3.5 to 6.5 Wm^{-1}K^{-1},[93,95,96,100] at room-temperature. Cross-plane thermal conductivity of WTe$_2$ and ReS$_2$ are 0.6 to 1.34 Wm^{-1}K^{-1}, [88,89] and 0.55 Wm^{-1}K^{-1},[90] respectively. Those low thermal conductivity values are due to their heavy molecular masses.

The cross-plane thermal conductivity data for WSe$_2$ merits additional discussion.[6, 51] For this material, one study showed that disordered yet layered crystals of WSe$_2$ can have cross-plane thermal conductivity that is six times lower than the amorphous limit of this material, and up to 30 times lower than the c-axis thermal conductivity of crystalline

WSe$_2$,[43] as displayed in Figure 2.1. The 0.05 Wm^{-1}K^{-1} cross-plane thermal conductivity measured in WSe$_2$ reprents the lowest measured value in a fully-dense, single-material solid at room temperature, and is comparable to that of air. This unusual behavior was attributed to the localization of lattice vibrations induced by random stacking of crystalline WSe$_2$ sheets, i.e. by controlling both order and disorder, and hence the thermal conduction channels, in this anisotropic material. Including the disordered WSe$_2$ measurement, the cross-plane thermal conductivity of WSe$_2$ is 0.05 to 2.45 Wm^{-1}K^{-1},[43,68,89,109] spanning almost two orders of magnitude. Interestingly, artificial heterostrutures, created by stacking crystalline monolayer graphene, MoS$_2$, and WSe$_2$, are able to achieve the lowest measured thermal conductivity in a fully-dense solid to date. By leveraging mismatches of mass densities and phonon density of states between 2D materials, the effective thermal conductivity is reduced to approximately a factor of three lower than air, in the range of 0.007 to 0.009 Wm^{-1}K^{-1}.[44]

2.3 Thermal Boundary Conductance

The thermal boundary conductance (TBC) and its inverse, the thermal boundary resistance (TBR), are used to describe the temperature discontinuity at an interface between two materials.[110] The TBC is also known as the Kapitza conductance,[111,112] although, strictly speaking, the term only applies for an atomically perfect and abrupt interface.[113] It relates the heat flux, Q, across the interface to the temperature drop, $\Delta T = Q/G$", where G" is the TBC in units of MWm^{-2}K^{-1}. Even atomically "perfect" interfaces have a finite TBC, because the temperature discontinuity is caused by phonon reflection and scattering at the interface.

Heat dissipation in 2D materials and devices is often limited by their interfaces with other materials, and this is particularly the case for monolayer or few-layer devices.[114,115] In fact, the interface dominates the internal (cross-plane) thermal resistance of a 2D film as long as TBC $< \kappa_\perp/t$ where t is the thickness of the film. Unlike the electrical conductivity and even the thermal conductivity of solids (which span approximately 20 and 5 orders of magnitude, respectively), the TBC between most materials spans a much narrower range, less than 4 orders of magnitude. Of course, this range refers to the TBC of intimately connected interfaces, not those between porous or otherwise rough interfaces, whose TBC could be much lower.[116]

Figure 2.2 summarizes the presently available data for the TBC of 2D materials with their environment, all at room temperature. Most such measurements are carried out either by a Raman opto-thermal method,[33,71,107] by time-domain thermoreflectance (TDTR, which necessitates a metal transducer like Al or Au on top),[66,109,117] or by the electrical 3ω method,[105,118] which requires encapsulating the sample in an insulator. Use of these approaches explains the limited interfaces of 2D materials probed thus far and the prevalence of interfaces with SiO_2, which is the most common insulator in nanoscale processing, formed by thermally oxidizing silicon substrate wafers.
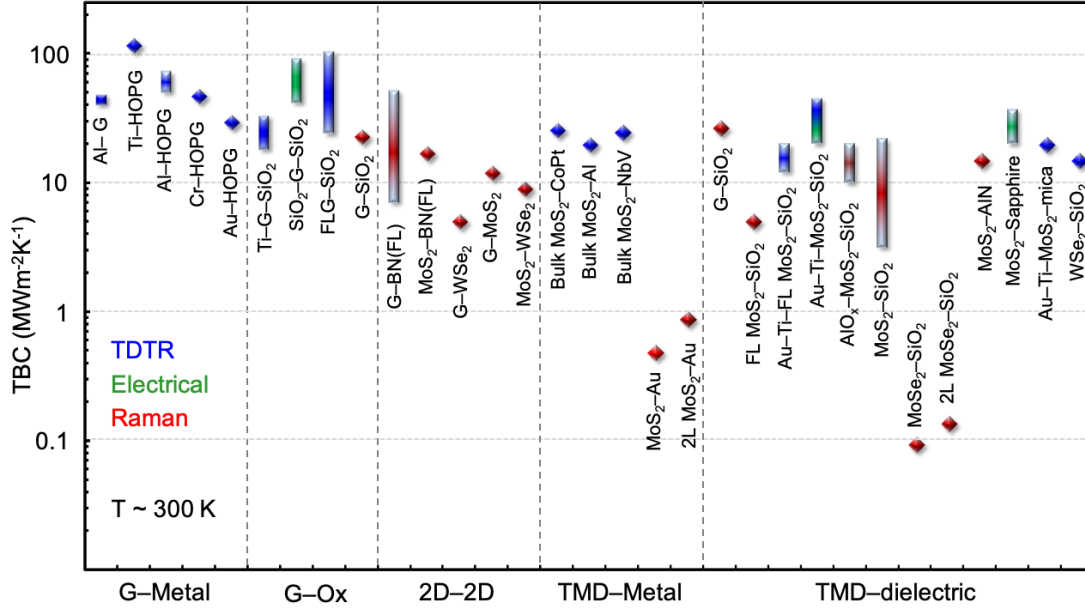
Figure 2.2. Room temperature thermal boundary conductance (TBC) of interfaces between graphene or graphite and metals,[119-121] graphene and oxides,[117,118,122,123] 2D and 2D materials,[44,124-126] TMDs and metals,[66,71] and TMDs with oxides.[33,71,107,127] All symbols and ranges are from experimental data, except "MoS$_2$–G" which is from molecular dynamics simulations,[125,126] displayed for comparison. G = graphene, FLG = few-layer graphene, HOPG = highly oriented pyrolytic graphite.

The ranges of data in Figure 2.2 are broadly grouped by TBC of graphene- or graphite-metal interfaces (G-Metal), graphene-SiO$_2$ interfaces (G-Ox), interfaces between dissimilar 2D materials (2D-2D), and interfaces of TMDs. All the G-Metal interfaces[119,120] and the G-Ox interfaces[35, 55, 56] are approximately in the range of 20-100 MWm^{-2}K^{-1}. Interestingly, the HOPG interface with various metals can be understood in terms of differences in adhesion.[120] Al and Ti have better adhesion to HOPG, yielding a smoother, continuous interface. In comparison, Cr and Au films have larger grains and weaker adhesion, leading to lower TBC.[120] This TBC range of 20 - 100 MWm^{-2}K^{-1} is roughly equivalent to the cross-plane thermal resistance of a graphite film between 60-300 nm thick (180 - 900 layers), or the thermal resistance of a SiO$_2$ film between 14 - 70 nm thick. Thus, it becomes immediately apparent how the thermal resistance of such

interfaces can fundamentally limit heat dissipation from all mono- and few-layer graphene devices in contact with typical insulators.[114,115]

The G-BN interface was measured by a combined electrical and Raman technique,[124] and the G-MoS$_2$ interface TBC range was estimated from MD simulations.[125,126] We included here these simulations for comparison, as there is no other experimental TBC data between dissimilar 2D materials, to our knowledge. The measured G-BN interface TBC was ~7.4 MWm^{-2}K^{-1}, lower than what might be expected for these smooth materials with light atomic masses, but within the common range of TBC for a variety of materials.[128] It is nevertheless possible that contamination of the interface by liquid or organic residues during fabrication (as the authors themselves have speculated[124]) could have limited heat flow in this measurement, and that the pristine G-BN interface TBC may be higher.

The TMD interfaces in Figure 2.2 deserve additional discussion. These are the results of several recent Raman optothermal measurements,[71,107,127] and a combined electrical-Raman measurement.[33] Although we subtract the contribution of the substrate thermal resistance from all reported values, the range of the TMD-SiO$_2$ interface TBC appears very large, with some values near 0.1 MWm^{-2}K^{-1},[71] which would be a record low for a solid-solid interface at room temperature.[128] It is important to note that purely optical measurements require accurate knowledge of the heating power in the MoS$_2$, dependent on the laser spot size and the absorption coefficient of MoS$_2$.[71,107,127] The electro-Raman measurement circumvents this through more accurate knowledge of the electrical input power.[33] In addition, the purely optical measurements were carried out on flakes

29

mechanically exfoliated onto their substrates, but the electro-Raman measurement was on monolayer MoS_2 grown directly (at high temperature by CVD) on the SiO_2 substrate.[39] Thus, it is possible that the exfoliated TMD samples measured by optical means did not have atomically smooth interfaces with their substrate and were potentially affected by interface roughness or by contamination during the transfer process.[71,107,127] The TBC of the interface between CVD-grown monolayer MoS_2 and SiO_2 reported from electro-Raman measurements was the highest, in the 8 to 15 $MWm^{-2}K^{-1}$ range.[33] This value is comparable to ~25 $MWm^{-2}K^{-1}$ obtained from TDTR measurements of the interface between Al or CoPt transducers and *bulk* MoS_2,[66] and probably more accurately represents the (upper) limit of such TMD interfaces.

By analogy to the earlier discussion, a TBC range of 1 - 10 $MWm^{-2}K^{-1}$ is roughly equivalent to the cross-plane thermal resistance of a MoS_2 film between 200 to 2000 nm thick, or the thermal resistance of a SiO_2 film between 140 to 1400 nm thick. Thus, it is extremely important to properly understand the lower end of the TBC range for the TMDs, and to take it into account when examining heat dissipation from TMD-based nanoelectronics.

In general, the expected range of TBC between two dissimilar materials has two limits. For a pristine but otherwise weakly bonded interface, the atoms of the two materials are in their equilibrium positions, as dictated by their interatomic interactions. The TBC is a consequence of only the lattice dynamics of the materials, and this limit can be understood in terms of the dissimilar vibrations on the two sides of the interface, and their

(inelastic) scattering at the interface.[110,111,129] This regime represents the upper limit of the

TBC, which could only be increased by applying higher incident pressure to the

interface.[130] The lower end of the TBC range is not well-defined, but could be understood

by considering imperfect interfaces due to surface roughness, wrinkling (especially for

2D monolayers), or contamination from impurities during the fabrication (e.g. 2D

material transfer) process. Thus, experimental data in Figure 2.2 strongly depend on the

"cleanliness" of the interface, with only the upper values approaching the fundamental

limit of a given interface.

Figure 2.3 also displays the temperature dependence of the TBC for several 2D material

interfaces. The TBC is a function of temperature, through the role of the heat capacity. At

temperatures below the Debye temperature ($T < \Theta_D$) the number of phonon modes

available to carry heat across the interface rises with the temperature ($C \propto T^{d/n}$ for a

phonon dispersion $\omega \sim q^n$ in d dimensions),[131] but the TBC becomes a constant, just like

the heat capacity, at $T > \Theta_D$. In Figure 2.3, as may be expected, "simple" interfaces tend

to have larger TBC, and more complex interfaces (e.g. Ti-G-SiO$_2$) tend to have lower

TBC. The latter is formed by two graphene interfaces in series, although it is not possible

to decouple the TBC of the Ti-G from the G-SiO$_2$ interface.

The TBC not only plays an important role in heat dissipation of 2D devices, but also

influences the device electrical performance. Better thermal interface can help heat

dissipation and lower the device operation temperature. For semiconductor devices, such

as field effect transistors (FET), lower temperature rise means less mobility degradation.

Similarly, for metal interconnects, better heat dissipation enables higher current density, improved reliability, and higher breakdown voltage.[86,132-134]
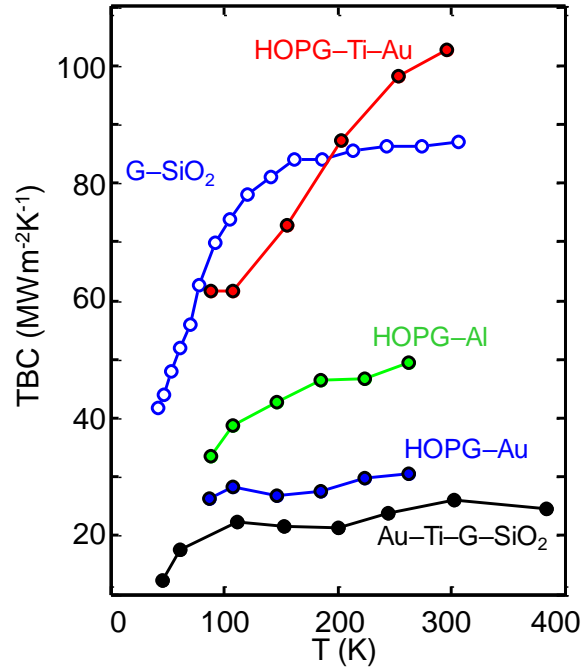
Figure 2.3. Experimentally measured temperature dependence of TBC, primarily available for graphite[120] and graphene[117,118] samples (HOPG = highly oriented pyrolytic graphite, G = graphene). The thermal boundary conductance increases with temperature as more phonon modes become available to carry heat across the interface.

2.4 Thermoelectric Properties

The reversible conversion between a temperature difference ΔT and an electric voltage ΔV is called a thermoelectric effect. Thermoelectric effects in materials can be grouped into three categories: the Seebeck effect is the generation of a voltage due to diffusion of charge carriers in a temperature gradient; its reverse, the Peltier effect, refers to the generation of a temperature gradient in the presence of current flow. In the Seebeck effect, the generated voltage is $\Delta V = (S_B - S_A)\Delta T$, where $S_{A,B}$ is the Seebeck coefficient (thermopower) of material A or B, and ΔT is the temperature difference. The third category is the Thomson effect, which can be seen as the continuous version of the

Seebeck effect: a spatial variation of S within a material due to a temperature gradient can create local electric fields, without the presence of a material junction.

The Seebeck coefficient of a material can be thought of as the specific heat per charge carrier, i.e. the energy per carrier per degree Kelvin. Metals tend to be poor thermoelectrics, because only a small fraction of carriers around the Fermi energy (E_F) can participate, and the thermopower $S \approx (k_B T/E_F)k_B/e$ is small, of the order 1 μV/K because $E_F \gg k_B T$, where e is the elementary charge. In semiconductors, on the other hand, the energy carriers can be "far" from E_F, and $S \approx (E_F - E)/(eT)$ can be large, of the order 0.1 - 1 mV/K. However, this implies that S in semiconductors scales inversely with doping, and will be largest in more insulating samples with lower conductivity σ.[135] Moreover, in semiconductors the thermopower can be negative ($S_n < 0$) for electrons but positive ($S_p > 0$) for holes.

Thermoelectric energy harvesters typically consist of alternating n- and p-type doped material "legs" which are arranged "electrically in series but thermally in parallel." This arrangement allows for all the thermoelectric segments to experience the same ΔT, but for their individual voltages (ΔV) to add up.[135] The efficiency of a thermoelectric energy converter can be expressed as the figure of merit $ZT = (S^2\sigma/\kappa)T$. Due to the inverse relationship of S and σ in semiconductors, this implies that the thermoelectric efficiency could be maximized at an intermediate doping level (which maximizes the power factor $S^2\sigma$) and for the lowest possible thermal conductivity κ. Thus, materials with highest ZT

are expected to be highly doped semiconductors with low (lattice) thermal conductivity, i.e. materials with heavier atoms and weaker interatomic bonds.

Based on the discussion above, one does not expect graphene, graphite, or WTe_2 to be good thermoelectric materials due to high κ (for graphene) and semimetallic nature (for both). However, 2D layered semiconductors (e.g. MoS_2 or SnSe, as we will see below) could have promising thermoelectric properties, particularly if the doping can be selected to maximize the power factor and ZT. Semiconducting 2D materials, as other low-dimensional materials, offer a large derivative of the electronic density of states around E_F, which can increase their thermopower S compared to bulk materials even at comparable σ.[136] In addition, 2D materials can be layered, thus increasing the number of interfaces and naturally decreasing the thermal conductivity ($\kappa_\perp$ in the cross-plane direction), one of the requirements for high ZT.

Figure 2.4 summarizes the experimentally determined ranges of thermopower for layered n- and p-type 2D materials, as they are known today (at room temperature). The data are organized by measurements along the "in-plane" direction, "cross-plane" direction (in highly anisotropic crystalline samples) or on "compressed polycrystalline bulk samples". As expected, the S of HOPG is low, as is that of WTe_2, both being semimetallic. Other thermopower values all correspond to semiconducting 2D materials, and the ranges given represent multiple studies carried out at different doping (carrier density) levels. In general, larger thermopower corresponds to lower σ (undoped material) and lower thermopower corresponds to higher σ (highly doped material). Data points represented by

34

diamonds were single measurements taken as a particular doping value. The experimental

data displayed include MoS$_2$,[136-145] WS$_2$,[45,146-149] MoSe$_2$,[45,150-156] WSe$_2$,[45,85,136,146,147,150-152,154,157] WTe$_2$,[87,150-152] MoTe$_2$,[150-152,158-160] SnSe,[161-166] SnS$_2$,[167] black phosphorus,[100,168-173] graphene,[53,124,174-176] as well as TiS$_2$ and its intercalated compounds.[177, 178]
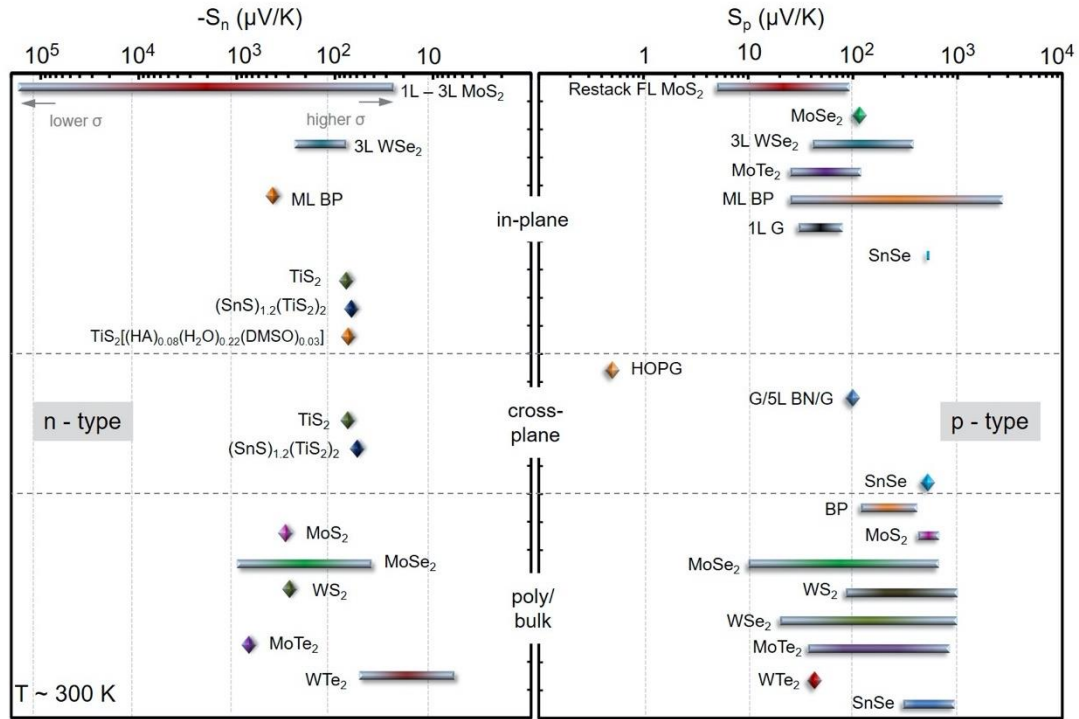
Figure 2.4. Room temperature Seebeck coefficients of various 2D materials: MoS$_2$,[136-145,179] WS$_2$,[45,146-149] MoSe$_2$,[45,150-156] WSe$_2$,[45,85,136,146,147,150-152,154,157] WTe$_2$,[87,150-152] MoTe$_2$,[150-152,158-160] SnSe,[161-166] SnS$_2$,[167] black phosphorus,[100,168-173] graphene,[53,124,174-176] and TiS$_2$ and its intercalated compounds.[177,178] The bars represent experimentally reported ranges, and the diamond symbols are individual data points. The lower end of a range of values correspond to higher doping, and the upper end to lower doping. The first two groupings represent in-plane and cross-plane measurements of the crystalline layered materials. The third grouping is for bulk 2D materials or their polycrystalline form which the directionality of the measurement was not reported.

For comparison, traditional bulk thermoelectric materials like Bi$_2$Te$_3$ have Seebeck

coefficient of approximately -228 µV/K (n-type) or 81 µV/K (p-type) at room

temperature.[180] Most 2D materials have comparable Seebeck coefficients to bulk Bi$_2$Te$_3$,

however available data for MoS$_2$, black phosphorus, and WSe$_2$ suggest that with

appropriate carrier modulation (i.e. doping) these 2D materials could have larger

electrical conductivity σ at the same thermopower S (compared to the bulk materials),[136]

ostensibly due to the low-dimensional thermoelectric enhancement discussed earlier.

Stacking 2D materials to create superlattice structures may lead to promising

thermoelectric properties, as the cross-plane thermal conductivity will be reduced by

interface phonon scattering. However, due to present difficulty in transferring and

stacking 2D films (while keeping such interfaces clean), only few data are available for

such structures. Figure 2.4 displays the experimental data for G-5L BN-G structures,[124]

and for intercalated TiS_2 compounds.[177]

Finally, Figure 2.5 displays recent data showing the measured thermopower of MoS_2 [136]

and WSe_2 [136,157] as a function of carrier density (here modulated with the presence of a

back-gate, rather than via chemical doping). As expected, the magnitude of $|S|$ decreases

at higher carrier densities, and therefore higher electrical conductance. The 2D power

factor is maximized for an electrical conductivity $\sigma \approx 10^5$ S/m, higher than can be

achieved with bulk materials.[136] For a typical mobility of ~30 $cm^2V^{-1}s^{-1}$ in a CVD-grown

monolayer TMD,[40,39,136] such an electrical conductivity corresponds to a carrier density of

~1.2×10^{13} cm^{-2}, well within the reach of experiments which rely on "electrostatic"

gating, but difficult to achieve by controlled chemical doping.
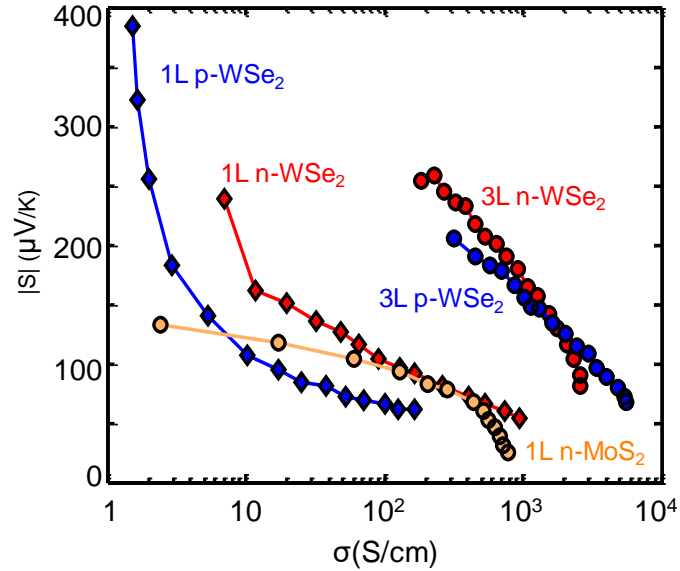
Figure 2.5. Experimentally measured dependence of thermopower S vs. electrical conductivity σ, where data are available, at room temperature.[136,157] Note that $S_n < 0 < S_p$. As expected, $|S|$ scales inversely with carrier density (n or p) and thus with electrical conductivity (σ).

2.5 Conclusion and Future Outlook

The thermal conductivities of 2D materials have strong anisotropy which is given by the structure of such materials and have a very large range (2 ~ 3 orders of magnitude) which is partly due to the huge difference of the molecule masses. And these may lead to different potential applications, such as heat spreader (e.g. graphene), heat isolation layer (e.g. amorphous or disordered WSe_2). 2D materials also have a large range of band gaps, from metal (graphene), semimetal (WTe_2), semiconductor (e.g. MoS_2, $MoSe_2$, $MoTe_2$, WS_2) to isolator (BN). By stacking those materials, we can further engineer their thermal (as well as electrical) properties, which do not exist in other 3D bulk materials in nature. TBC plays a much important role in 2D materials and devices comparing to conventional 3D material. As the dimension is scaling, the intrinsic thermal resistance is small, the all system is very sensitive to the contamination, or imperfect interfaces with other materials

and environment. Seebeck coefficient can be increased by gating the material and minimizing electrical conductivity, but these will harm the figure of merit (*ZT*). To realize 2D material based thermoelectrics, stacking will be important (which also required clean transfer method).

Chapter 3

Thermal Transport in WTe$_2$

This chapter presents the extracted thermal properties of WTe$_2$ devices by using electrical measurements. This chapter will discuss the fundamental material properties of WTe$_2$. High-field electrical measurements and electro-thermal modeling reveal that ultra-thin WTe$_2$ can carry remarkably high current density (approaching 50 MA/cm^2, higher than most common interconnect metals [181-183]) despite a very low thermal conductivity (of the order ~3 Wm^{-1} K^{-1}). These results suggest several pathways for air-stable technological viability of this broadly relevant layered semimetal.

Results in this chapter were published in M. Mleczko, R. Xu, et al., "High current density and low thermal conductivity of atomically thin semimetallic WTe$_2$." *ACS Nano*, **10**, (8),7507, 2016.

3.1 WTe$_2$ Material Properties

The preceding decade has seen much interest in two-dimensional (2D) nanomaterials, often exhibiting unique evolution of chemical and physical properties as material thickness is scaled from layered bulk to individual atomic or molecular monolayers.[184, 185,186,187] While semiconducting 2D materials have received much attention, layered 2D semimetals other than graphene have been relatively underexplored in the atomically thin limit. Materials like β-MoTe$_2$ and WTe$_2$ stabilize as semimetals in a distortion of the octahedral 1T (CdI$_2$ structure) geometry, with in-plane buckled chains formed by pairs of

Mo/W atoms dimerizing in intermetallic charge-exchange,[188-190] while van der Waals bonding dominates interlayer interaction. Whereas $MoTe_2$ may be synthesized in both 2H- and T_d- polytypes, or reversibly switched between the two as a function of temperature or strain,[191, 192] WTe_2 has been known since the 1960s to exclusively adopt the latter structure, irrespective of growth conditions [188, 193, 194] or conventionally achievable strain,[192] as the heaviest of the Group VI dichalcogenides. Despite the inaccessibility of a semiconducting phase, this semimetal has received renewed attention from the experimental observation of non-saturating magnetoresistance in bulk samples, in excess of 13,000,000% at 60 T.[195] This behavior was attributed to perfect compensation between balanced electron and hole populations at the Fermi surface below 150 K, projected to persist down to individual monolayers.[196, 197] Recent studies have also identified WTe_2 as a potential two-dimensional contact for planar devices, with a uniquely low electronic work function ($\Phi < 4.4$ eV) amongst 2D metals,[198] recently applied in realizing unipolar n-type transport in the nominally ambipolar semiconductor WSe_2.[199] Layer-dependent experiments of any kind are nonetheless limited,[200-203] owing to a lack of geological sources, challenges in precursor purification during bulk crystal growth,[194, 195] as well as observed degradation (oxidation) of thin layered tellurides with exposure to ambient oxygen and moisture.[200,204] In particular, Wang and colleagues studied magneto transport in uncapped flakes down to bilayer thickness,[203] reporting an insulating regime in sub 6-layer samples attributed to oxidation-induced disorder from ambient exposure.

3.1.1 Device Structure

Bulk crystals of WTe_2 were grown directly by Chemical Vapor Transport (CVT) of a commercial molecular powder (American Elements WTe_2, 99.5%), with no need for chemical or thermal precursor pre-treatment, using elemental iodine as a transport agent. We achieved a high yield of few-millimeter-sized crystals, exhibiting both ribbon- and platelet-like morphologies with clear evidence of layered structure under mechanical cleavage or Scanning Electron Microscope (SEM) inspection (shown in Figure 3.1).
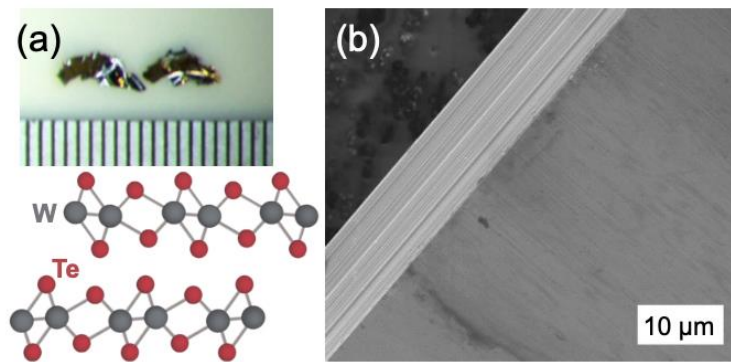
Figure 3.1. (a) Bulk WTe_2 crystals grown by CVT, with mm increments for scale, and cartoon profile of 1T'- (T_d-) layered crystal structure. (b) SEM micrograph of bulk crystal displaying layered structure at edge.

We then mechanically exfoliated few-layer WTe_2 flakes onto 90 nm SiO_2 on p^{++} Si substrates under an inert atmosphere (a nitrogen-purged glovebox with O_2 and H_2O below 3 ppm at their highest levels) and initially capped them with a 300 nm film of poly(methyl methacrylate) (PMMA), serving both as protective coating and resist for electron-beam (e-beam) lithography. Contacts were lithographically defined, developed and metalized with 20 nm Ti / 20 nm Au, such that exposed flake surfaces at the contact interface saw cleanroom air for less than 5 min. before transfer into a load-locked e-beam evaporator (base chamber pressure $\sim 10^{-8}$ Torr). To mitigate the possibility of channel

oxidation, we performed resist and metal lift-off in another nitrogen glovebox connected

to a thermal ALD chamber where, after lift-off, we immediately deposited ~15 nm of

amorphous AlO_x *in situ via* alternating trimethylaluminium (TMA) and H_2O pulses at

150 °C.
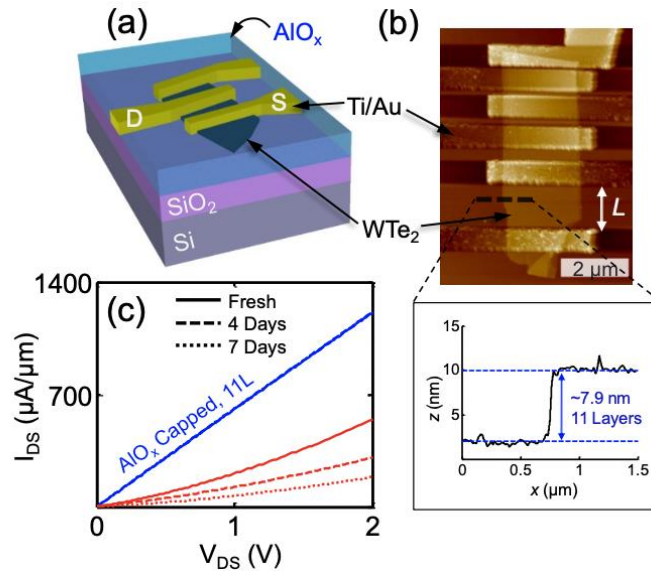
Figure 3.2. (a) Schematic of AlO_x-capped WTe_2 Transfer Line Method (TLM) structures on 90 nm SiO_2 (on Si) with Ti/Au contacts. (b) AFM micrograph of fabricated WTe_2 TLM structures showing 5 device channel lengths (from 85 to 1500 nm) and 6 electrodes, capped with ~15 nm AlO_x by ALD. AFM height profile (lower inset) was extracted along the dotted line. (c) Time-dependent degradation of current vs. voltage (I–V_{DS}) in AlO_x capped (11-layer, $L = 0.5$ μm) and uncapped (7 layers, $L = 0.46$ μm) devices. The ALD-capped devices are stable for over one week, whereas the bare (uncapped) devices degrade within hours or days.

Inspection by optical and atomic force microscopy (AFM) revealed uniform nucleation of

this capping dielectric (Figure 3.2), with identical RMS roughness on flakes and the

surrounding oxide (< 0.4 nm). The smoothness of the capping film facilitated layer

counting in flakes directly from AFM height profiles, uniformly measured as integer

multiples of the interlayer spacing ~0.704 nm[188, 189] with an additional ~0.2 nm offset.

3.1.2 Oxidation and Capping Protection

We utilized the encapsulation to prevent ambient oxidation of ultrathin WTe_2, and ALD alumina was chosen for its compatibility with standard microfabrication and effectiveness as an oxygen and moisture barrier (also recently applied for environmental stability of few-layer black phosphorous [205,206]). Grown on devices whose channels had only seen an inert nitrogen atmosphere, 15 nm AlO_x films were found to significantly improve device yield and preserve Ohmic response with no noticeable current degradation after one week (Figure 3.3(a)). In comparison, uncapped devices measured immediately after in-air metal lift-off manifested current non-linearity at moderate source-drain biases, and significant decline in performance over several days - even when stored in partially deoxygenated environments (*e.g.* a tabletop drybox). Such degradation is consistent with increased charge trap density from the progressive oxidation of top-most WTe_2 layers, which we evaluated by high resolution X-Ray Photoelectron Spectroscopy (XPS) in Figure 3.3(b).
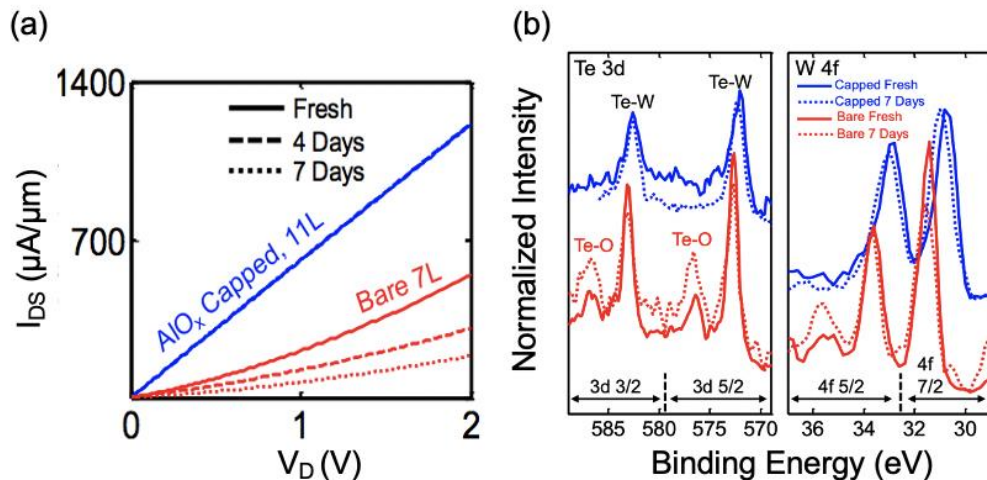
Figure 3.3. (a) Time-dependent degradation of current vs. voltage (I–V_{DS}) in AlO_x capped (11-layer, $L = 0.5$ μm) and uncapped (7 layer, $L = 0.46$ μm) devices. The ALD-capped devices are stable for over one week, whereas the bare (uncapped) devices degrade within hours or days. (b) High-resolution XPS of ALD-capped and bare multilayer WTe_2 flakes on SiO_2/Si substrates; ambient degradation is visible in the

formation of Te-O sub-peaks and a binding energy shift of W-4f peaks suggesting partial WO_3 bonding character.

Oxidation of uncapped crystals is evident in the Te 3d spectra of both freshly cleaved and aged multilayers on SiO_2/Si, most prominently in the appearance of secondary peaks across the 3d 3/2 and 5/2 energy range matching reference values for Te (IV)-O binding in TeO_2.[207,208] These features increase in intensity with time relative to Te-W bonds, matching a trend recently observed in Ref. 200, though are entirely absent on surfaces probed through the AlO_x capping. There, only W bonding is measured even after 7 days of storage. Ancillary evidence is provided in the upward energetic shift of W-4f peaks in uncapped samples, by an average ~0.8 eV relative to capped flakes, and appearance of a high-energy shoulder suggesting a partial WO_3 bonding character induced through atmospheric exposure. Layered WO_3 is the oxide most readily formed on W dichalcogenide crystals,[209,210] producing XPS W-4f reference peaks measured an average 2-3 eV higher [211,212] in binding energy than those of comparatively closely spaced WS_2 and WSe_2 [212-214] used here as analogues for WTe_2. Our findings indicate significant chemical degradation of uncapped layers during the ~ 1 hour period of ambient exposure between glovebox-based exfoliation and XPS measurement, despite prior studies observing constant optical contrast for exposed few-layer samples on the order of 1 day.[203] This supports the conjecture of oxidation-induced disorder driving a metal-to-insulator transition in resistivity as WTe_2 thickness is decreased below 6-layers,[203] a regime avoided through careful encapsulation in all our thinner samples discussed below.

3.1.3 Semimetallic I-V behavior

Figure 3.4 shows the lack of gate voltage dependence for an AlO_x capped 14-layer WTe_2

flake on 90 nm SiO_2 and p++ Si global back-gate, showing negligible source-drain

current modulation, which indirectly proves the semimetallic property of this material.

Figure 3.5 shows the band diagrams of both bulk and monolayer WTe_2. The overlap

between conduction band and valence band indicates that WTe_2 is semimetallic.
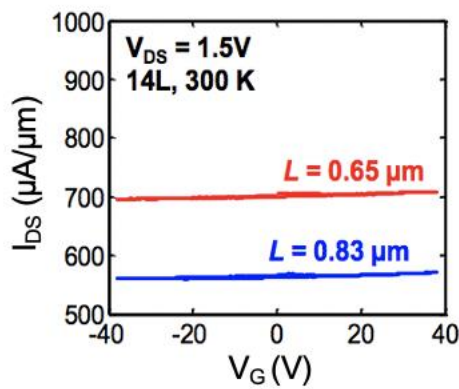
Figure 3.4. Lack of gate voltage dependence for an AlO_x capped 14 layer WTe_2 flake on 90 nm SiO_2 and p++ Si global back-gate, showing negligible source-drain current modulation.
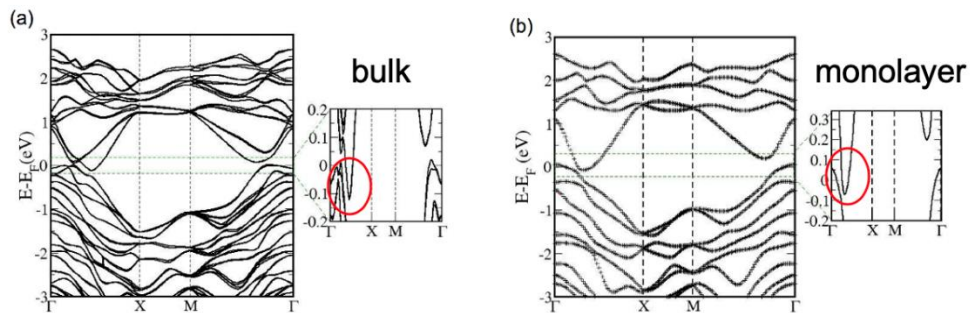
Figure 3.5. Calculated band structures of 1T' WTe_2 (a) bulk and (b) monolayer.[215]

3.1.4 Electrical Properties

We performed electrical characterization *via* two-terminal and transfer line method

(TLM) test structures, with channel lengths L from 80 nm to 2 µm. As expected for

carrier-rich semimetallic devices, the Si back-gate had a negligible effect on current

modulation and the remainder of electrical measurements were carried out at zero gate bias. Figure 3.6(a) shows the linear fits for a TLM test structure, over the 80-300 K temperature range. Plotting the measured resistance normalized by width, $RW = R_SL + 2R_C$, yields a slope R_S as the intrinsic sheet resistance and the intercept $2R_C$ as the total contact resistance (L and W are the length and width of WTe$_2$ channel).
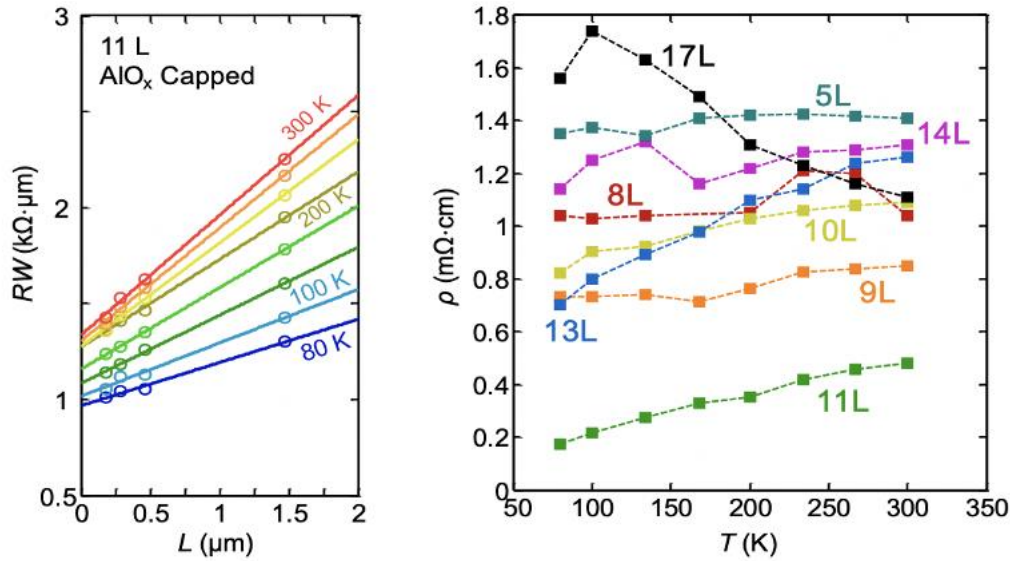
Figure 3.6. (a) Sample TLM plot of AlO$_x$ capped, 11-layer WTe$_2$ devices presenting the total resistance (normalized by width) vs. channel length L; lines are a numerical fit to measured values (symbols). The vertical intercept yields $2R_C$ and the slope yields R_S. (b) Measured temperature dependence of resistivity for AlO$_x$ capped WTe$_2$ devices with 5–17 layers, derived from TLM sheet resistance.

Figure 3.6(b) presents a summary of TLM-extracted resistivity ρ in the range 0.4–1.4 mΩ cm (at room temperature) for WTe$_2$ devices of different layer thicknesses. Most ultra-thin devices display metallic behavior (ρ increasing with T), consistent with prior reports of bulk resistivity for synthetic WTe$_2$.[202,216,217] Only the 14L and 17L devices exhibit some decline in ρ with increasing T; however, we note these were the two most resistive TLM structures probed, thus their temperature-dependent behavior is more indicative of defect-limited hopping rather than phonon-limited transport (as for the devices with lower ρ).

Interestingly, no clear layer dependence of resistivity emerges for the thickness range probed here; this could be due to different crystalline orientations of the devices, as buckled W chains break the 2D symmetry of the layer plane with a preferred directionality.[188-190] This has been noted in scanning tunneling microscopy (STM) measurements of aligned zigzag features on cleaved WTe_2 surfaces,[218] and a strong variation on magneto transport in bulk ribbons with the angle of the applied field.[195] Thickness invariance in this range is also consistent with recent measurements of an effectively 3-dimensional (3D) electronic structure in WTe_2,[219,220] with only moderate Fermi surface anisotropy in 2D layers attributed to increased interlayer coupling from the described lattice distortion. Room-temperature resistivity remains an order of magnitude greater than that of layered band metals in bulk,[193,216] including most Group V (V, Nb, Ta) disulfides, selenides and tellurides. It nonetheless remains comparable to that of bulk WTe_2,[202, 217] unlike the 10-fold or greater increase of ρ in metals like $1T\text{-}TaS_2$ in the few-nanometer thickness regime.[221, 222]

Extracted contact resistances for 20 nm Ti / 20 nm Au leads also show no clear dependence on layer number, with mean R_C spanning a range of 500-600 $\Omega\cdot\mu m$ across 80-300 K. The contact resistance to ultra-thin WTe_2 found here is near the lower end of reported resistances for evaporated metals on Group VI layered semiconductors (0.5–2 $k\Omega\cdot\mu m$) without chemical doping or lattice-level modification.[223,224] Averaged R_C values were then used to estimate the effective field along channels on thinner flakes (3-7 layers), for which full TLM structures were not available, enabling extraction of overall current density J at set field values. Despite the aforementioned variability obscuring an

explicit layer dependence, the current density J appears to increase for devices up to 9-11 layers thick, beyond which J saturates. A gradual fall-off in current density is expected for thicker, metallic layered crystals with top contacts due to interlayer resistance limiting current flow to the top-most layers. In contrast, the cross-plane current distribution in few-layer graphene or semiconducting 2D materials is determined by competing effects from electrostatic gating, top-down charge-injection, and interlayer electrostatic screening.[225,226] For a carrier-rich (semi-) metallic 2D crystal, dielectric screening limits the charge injected into lower layers from top contacts as the thickness is increased, effectively confining current to the upper-most layers in the absence of direct edge-injection. Underlying strata serve primarily to screen-out any substrate (*e.g.* oxide) charge fluctuations in approaching bulk transport limits.[225] Absence of this screening in the thinnest, most sensitive samples ($\leq$ 5L) explains the lower measured current densities and higher TLM-extracted contact resistance.

3.1.5 High Field Electrical Measurement

We next examine high-field coupled electrical and thermal transport in our WTe$_2$ devices, as summarized in this section. Figure 3.7 displays several measured *I–V* curves up to breakdown of our WTe$_2$ devices, with high lateral V_{DS} (the higher resistivity at 80 K is due to inter-sample variability of particular 5-layer and 10-layer flake). We find that AlO$_x$-capped WTe$_2$ devices can reach up to 30–50 MA/cm^2 current densities, in excess of the 10-20 MA/cm^2 benchmark for VLSI interconnect stress-testing.[181-183] This current density range is larger than typical values for Al and Cu, which are several MA/cm^2, and is similar to bulk W films at several tens of MA/cm^2.[227-229] However, among atomically

thin semimetallic layers only graphene can withstand higher current densities, typically hundreds of MA/cm^2 and approaching 1 GA/cm^2 for aggressively scaled nanoribbons.[230] SEM imaging of failed devices showed breakdown near the device mid-points, with metal contacts fully intact, suggesting WTe$_2$ failure at the point of maximum temperature and good contact resistance up to high bias. Incomplete breakdown in our thinnest devices (3-5L) suggests improved heat-sinking with reduced interlayer thermal resistance. Moreover, ohmic response and comparable breakdown densities (15-50 MA/cm^2) are consistent across this thickness range, despite the previously discussed reduction in low-field current density. This is contrasted with a reportedly distinct insulating regime in uncapped <6L samples,[203] demonstrating the importance of avoiding channel exposure to oxygen/moisture during processing. For comparison, the less-resistive band metal TaSe$_2$ supports peak current densities of 36 MA/cm^2 in conventionally fabricated devices at body thickness $t \sim 12$ nm, degrading to negligible levels in the few-layer limit under ambient conditions.[231]
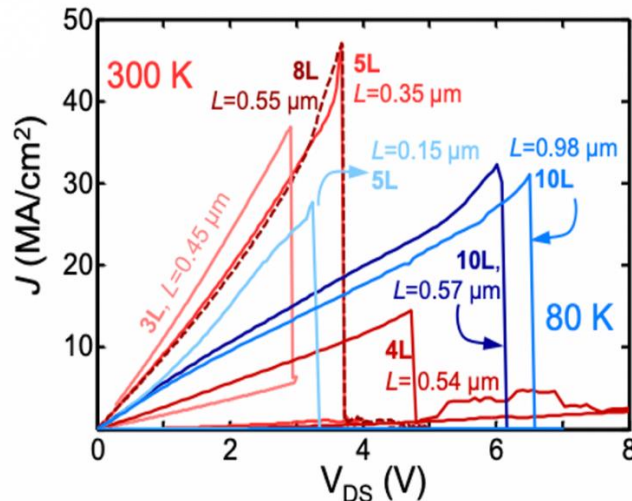
Figure 3.7. Current vs. voltage up to breakdown of ALD-capped WTe$_2$ devices at 80 K (blue) and 300 K (red) ambient in vacuum probe station (~10^{-5} Torr), demonstrating self-heating behavior and thermal breakdown. The maximum current density approaches 50 MA/cm^2, almost an order of magnitude higher than typical 3D metal (*e.g.* Al, Cu) interconnects.
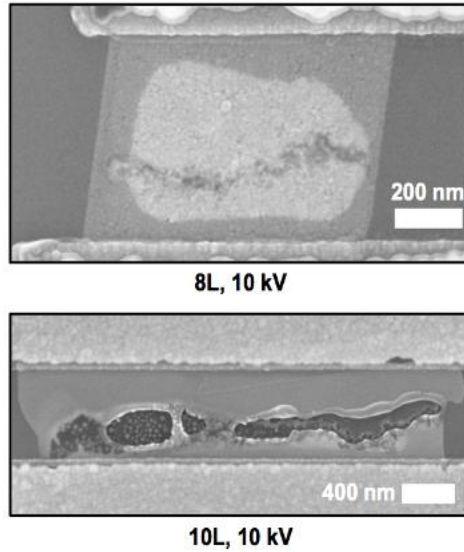
Figure 3.8. SEM micrographs of AlO_x-capped WTe_2 channels following high-current thermal breakdown, imaged at 10 kV. Uniform breakdown in channel centers signifies uniform heating during operation and negligible contact resistance.

Figure 3.8 shows SEM images of the devices after high-current breakdown. Breakdown in channel centers indicated that the contacts are good, and channel has uniform heating during operation. Also, breakdown around channel centers is consistent with measured metallic conduction, failing at the center where has the highest temperature in the channel. Near-complete rupture is observed across the entire width of flakes, with apparent local disruption of the capping dielectric layer in some devices (bottom figure). The failure temperature is 1300 K, which is melting temperature of WTe_2. It happens with several secondary phenomena, including the formation of Al-Te glasses. Volume expansion may explain the oxide stress visible around the failed device show in the top figure.

We also obtain current densities of >30 MA/cm^2 (shown in Figure 3.9) in two WTe$_2$

nanoribbons ($\sim$50 nm wide). These current densities are larger than typical values for Al

and Cu nanowire, which are only several MA/cm^2, and are similar to bulk W films at

several tens of MA/cm^2. Maximum current of these nanoribbons is almost the same with

the values of larger devices.

This is unlike short graphene nanoribbons which show higher current density than large

graphene devices due to their larger thermal healing length which facilitates heat sinking

to the contacts. This highlights that the current density limitation of short WTe$_2$ NRs is

intrinsic, due to their low in-plane thermal conductivity.
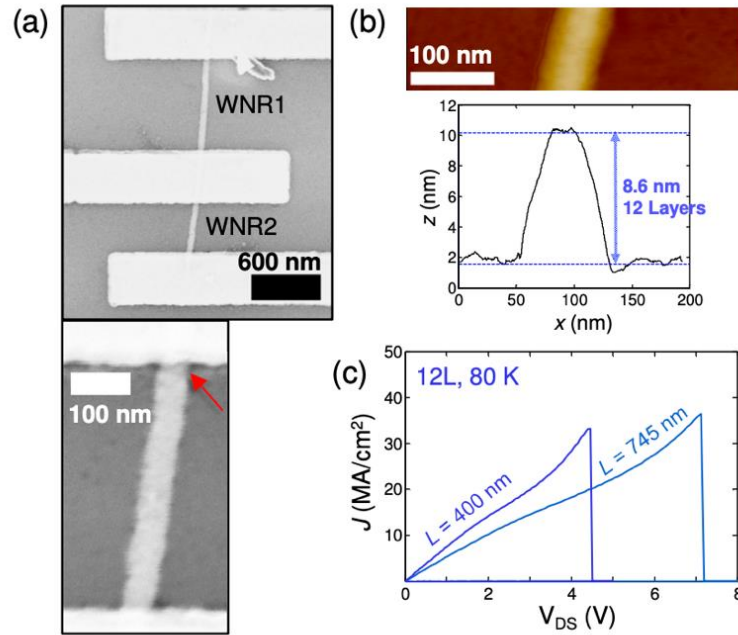
Figure 3.9. (a) SEM micrographs and (b) AFM micrographs and height profile of a ~50 nm wide, 12L thick exfoliated WTe$_2$ nanoribbon (WNR), capped with AlO$_x$. Red arrow indicates point of failure. (c) Breakdown current densities of the two WNRs (at 80 K ambient) are comparable to the large WTe$_2$ device current densities.

3.2 Theoretical Calculation

We use high field electrical data to extract thermal properties. First, we note that for modeling purposes $\rho(T)$ can be fit as a function of temperature by a cubic polynomial (shown Figure 3.10). This facilitates current calculation as a function of temperature, $I(T) = V/R(T)$, self-consistently with a self-heating (SH) model.
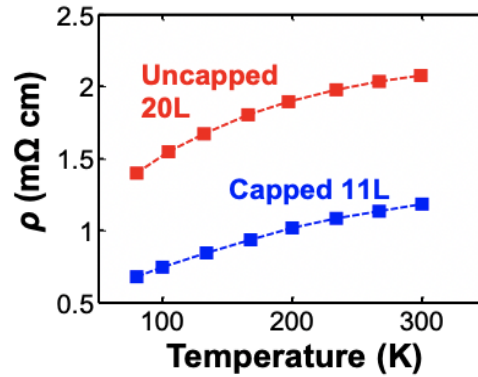
Figure 3.10. Comparative temperature-dependent resistivity of newly made capped and uncapped flakes, fit with a cubic polynomial model (dashed lines).

3.2.1 Analytical Model

To estimate the average temperature rise, we can express the thermal resistance per unit length from the WTe$_2$ channel to the substrate as:[230]

$$g^{-1} = \frac{R_{Cox}}{W} + \left\{ \frac{\pi k_{ox}}{\ln[6(t_{ox}/W+1)]} + \frac{k_{ox}W}{t_{ox}} \right\}^{-1} + \frac{1}{2k_{Si}}\sqrt{\frac{L}{W_{eff}}} \qquad (3.1)$$

where t_{ox} is the SiO$_2$ thickness, k_{ox} and k_{Si} are the thermal conductivities of SiO$_2$ and Si (including their temperature dependence[232]) and W_{eff} is an effective width of the heat dissipation path through the Si substrate.[230] The equation above represents the series combination of three terms: the thermal resistance of the WTe$_2$–SiO$_2$ interface $\mathcal{R}_{Cox}$, the spreading thermal resistance into the SiO$_2$,[57] and the spreading thermal resistance into the Si substrate (Figure 3.11).
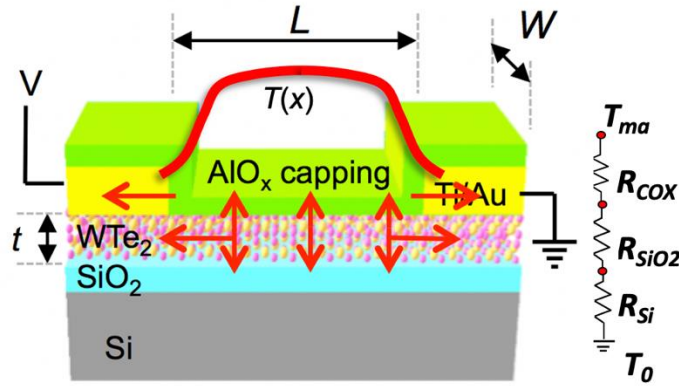
Figure 3.11. Device schematic showing pathways for heat sinking with arrows through metal contacts, capping layer (laterally) and through the substrate (vertically). Inset shows thermal resistance pathways for vertical heat flow which dominates in longer devices.

The average temperature rise due to Joule heating is $T = T_0 + I(T)V\mathcal{R}_{th}$, where T_0 is the ambient temperature and $\mathcal{R}_{th} \approx 1/(gL)$ is the total thermal resistance for "long" devices, much longer than the thermal healing length L_H along our WTe$_2$ devices. Here $L_H = (kWt/g)^{1/2} \approx 70$ to 150 nm (as we will see in the following discussion), where t is the thickness and k is the lateral thermal conductivity of WTe$_2$. Figure 3.12 shows that this model with SH can correctly reproduce the decrease in current at high field, whereas the model without SH cannot capture this behavior, for a "long" device with $L \approx 750$ nm. The WTe$_2$–SiO$_2$ thermal interface resistance was used as a fitting parameter here, yielding an estimated $\mathcal{R}_{Cox} \approx 3\times10^{-8}$ m^2 KW^{-1}, which is similar to the values of $\mathcal{R}_{Cox}$ for graphene–SiO$_2$ interfaces.[41]
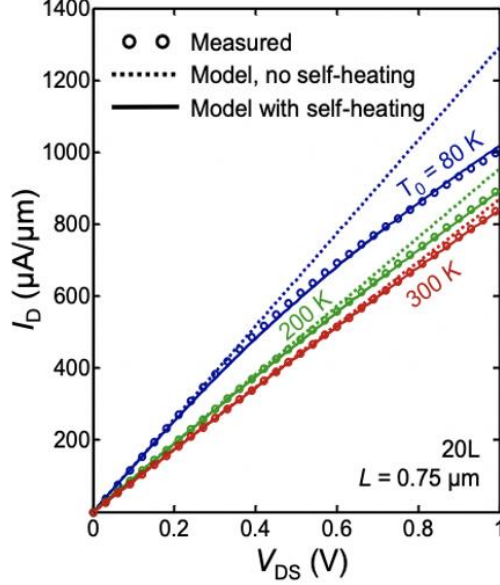
Figure 3.12. Measured (symbols) and simulated (lines) current vs. voltage for an uncapped 20-layer WTe$_2$ device on 90 nm SiO$_2$ (on Si). Solid lines modeled with self-heating (SH), fit with $\mathcal{R}_{Cox} = 3\times10^{-8}$ m^{2}K/W; dashed lines are calculated without SH.

We utilize these self-heating studies at high field to estimate the lateral thermal conductivity k of WTe$_2$, with the model of Liao *et al*.[57] This is primarily applicable to our "shorter" devices (compared to L_H) where more heat flows laterally into the metal contacts. We can express the peak (maximum) temperature along the WTe$_2$ device as a function of the input power and other thermal parameters as:

$$T_{max} = T_0 + P\left(\frac{1}{gL}\right)\left(\frac{1 + gL_H R_T x - 1/\cosh[L/(2L_H)]}{1 + gL_H R_T x}\right)$$
(3.2)

where $x = \tanh[L/(2L_H)]$. Similarly, we can also express the average temperature (T_{avg}) along the WTe$_2$:

$$T_{avg} = T_0 + P\left(\frac{1}{gL}\right)\left(\frac{1 + gL_H R_T x - 2x L_H /L}{1 + gL_H R_T x}\right)$$
(3.3)

where $R_T = L_{HM} / [k_m t_m(W+2L_{HM})]$ is the thermal resistance of the metal contacts, $L_{HM} = (t_m t_{ox} k_m/k_{ox})^{1/2}$ represents the thermal healing length into metal contacts of thickness t_m

and thermal conductivity k_m, and $T_0 = 80$ K or 300 K. The input power is $P = I(V_\text{DS} -$

$2IR_\text{C})$, where R_C is the electrical contact resistance, and $T_\text{max} \approx 1300$ K is the WTe_2

breakdown temperature (the melting temperature of WTe_2).[11] For devices capped by

AlO_x, we must be careful to account for partial lateral heat sinking through this capping

layer. Thus, we modify the lateral healing length to $L_\text{H} = (k_\text{eff}Wt/g)^{1/2}$ where the effective

thermal conductivity k_eff is the parallel combination of lateral heat flow along the WTe_2

and the AlO_x capping ($t_\text{cap} \approx 15$ nm and $k_\text{cap} \approx 4$ $Wm^{-1}K^{-1}$ at high temperature near

T_max).[233, 234] Once k_eff is estimated from our SH model, the thermal conductivity of WTe_2

can be deduced from $k = k_\text{eff} - k_\text{cap}(t_\text{cap}/t)$.

We note that in this high-temperature breakdown model we cannot fit the thermal

conductivity k and $\mathcal{R}_\text{Cox}$ independently; nonetheless, values consistent with all our

measured device breakdowns are fit at $k = 2.5\text{-}3.5$ $Wm^{-1}K^{-1}$ for $\mathcal{R}_\text{Cox}$ of 5×10^{-9} $m^2\,KW^{-1}$,

up to $k = 9\text{-}11$ $Wm^{-1}K^{-1}$ for $\mathcal{R}_\text{Cox} = 10^{-8}$ $m^2\,KW^{-1}$. $\mathcal{R}_\text{Cox}$ values are expected to be smaller

at high temperatures (near $T_\text{max} \approx 1300$ K) than the earlier 3×10^{-8} m^2KW^{-1} estimate at 80-

150 K, due to higher phonon occupation.

The lateral thermal conductivity estimated here is greater than that measured by Jana *et*

al. on bulk polycrystalline samples of WTe_2 (~1 $Wm^{-1}K^{-1}$),[202] suggesting higher material

quality in exfoliated mono-crystalline flakes, within the range computed by Liu *et al*.[235]

The electronic contribution is 10 to 30% of the overall thermal conductivity, based on

estimates with the Wiedemann-Franz Law. The lower bound of our estimated k is less

than half the maximum lattice conductivity of ~9 $Wm^{-1}K^{-1}$ along the [100] (in-plane)

WTe$_2$ direction, from first-principles calculations.[235] Its magnitude and variation between devices is nonetheless consistent with the anisotropy expected between multiple in-plane (*i.e.* relative to W-W dimer chain orientation) and cross-plane k values, suggesting a strong role of structural asymmetry on thermal transport in 1T'/T$_d$-distorted crystals. Orientation-mapping of devices and ancillary measurement techniques (*e.g.* time-dependent thermoreflectance across flakes of varying thickness) are needed to elucidate the directional-dependence of this parameter.[236] Finally, such low thermal conductivity may act set intrinsic limits on current density, unlike graphene wherein high in-plane k facilitates longer healing length and boundary-limited thermal transport. Whereas scaling to short, narrow nano-ribbons improves peak J of graphene by over an order of magnitude,[230] no improvement was observed in the breakdown density across a 12L WTe$_2$ ribbon with $W = 50.5 \pm 1$ nm.

3.2.2 Finite Element Simulation

To validate the analytic model, we have also used COMSOL simulation results as comparison. And we also explore different type of capping layers on WTe$_2$ devices. boron nitride is a 2D insulator with very high thermal conductivity up to a few hundreds.

Finite element simulations confirm the predictions of our analytic model, and also confirms the ranges of thermal conductivity and interface thermal resistance. We also find that the device temperature can be further reduced by using h-BN capping, which provides excellent heat spreading due to its large in-plane thermal conductivity, shown in Figure 3.13. Figure 3.13(a) uses AlO$_x$ capping and the maximum temperature is around

1300 K while there is no capping layer in Figure 3.13 (b). Figure 3.13(c) uses BN, and

maximum temperature is 1100 K. In addition, the peak temperature can also be reduced

by decreasing the SiO2 substrate thickness, shown in Figure 3.13(d).
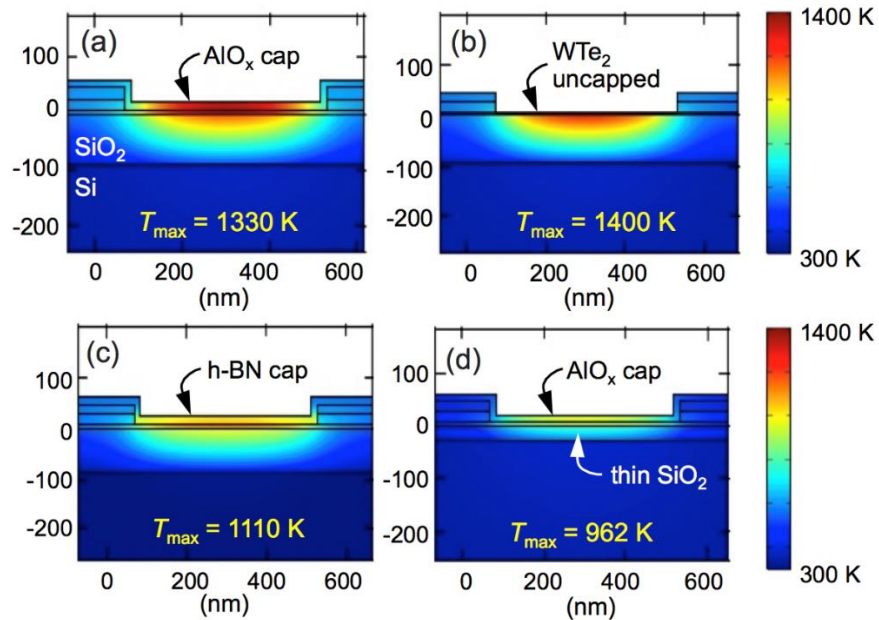
Figure 3.13. Temperature distribution from finite element (FE) simulation with 3.55 V applied to a WTe$_2$ device (dimensions $L = 465$ nm, $W = 1.1$ μm and $t = 6.3$ nm). (a) capped with 15 nm AlO$_2$ as in the experiments, (b) uncapped, (c) capped with 15 nm h-BN (all on 90 nm SiO$_2$ on Si substrate). (d) capped with 15 nm AlO$_x$ on 30 nm SiO$_2$ substrate. (a) has T_{max} around the melting temperature of WTe$_2$, consistent with experiments (FE simulations use temperature dependent thermal conductivities of Si, SiO$_2$ and h-BN.)

Figure 3.14 compares the maximum temperature (T_{max}) in the channel of several different

device structures. Temperature can be reduced by using h-BN capping (shown in black

dashed line), and it can be further reduced by thinning the oxide layer thickness from 90

nm to 30 nm.
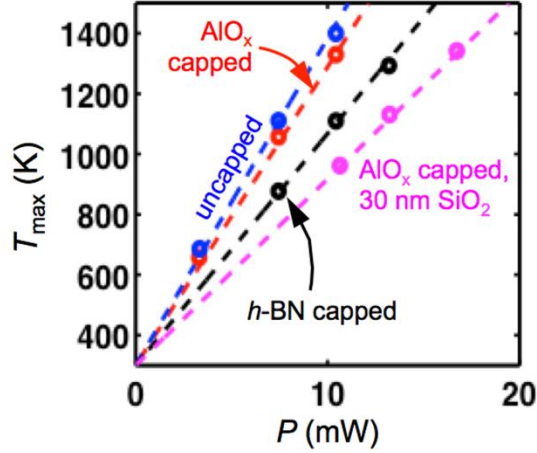
Figure 3.14. T_{max} vs P. Comparing analytical model (dashed lines) and simulation results (symbols). We use an effective thermal conductivity for anisotropic h-BN in the analytical model, $k_{BN} = (k_{\parallel} k_{\perp})^{1/2} \sim 15$ W/m/K.

With significant reduction of temperature, we can improve max current density to around

50 MA/cm^2 in BN capped device and thin oxide device (shown in Table 3.1)

Capping material	t_{cap} (nm)	t_{SiO2} (nm)	k_{cap} (W/m/K)	V_{max} (V)	J_{max} (MA/cm^2)
h-BN	15	90	~150 (in-plane) ~1.5 (cross-plane)	4	48
AlO$_x$	15	90	~4	3.55	43
AlO$_x$	15	30	~4	4.5	54
none				3.4	41

Table 3.1. Summary of FE simulations, using $k=10$Wm^{-1}K^{-1} and $R_{Cox} = 10^{-8}$ m^{2}KW^{-1} for WTe$_2$. Comparing maximum achievable voltages and current densities of h-BN capped, AlO$_x$ capped and uncapped WTe$_2$ devices at $T_{max} \sim 1300$ K (breakdown). The h-BN capped device has the highest current density (J_{max}). Thermal conductivity values are used at high temperature, where data are available, including the anisotropy of $k_{\parallel}$ and $k_{\perp}$ in h-BN.

3.3 Electronic Contribution of Thermal Conductivity

The electronic contribution k_e to the net thermal conductivity k of few-layer WTe$_2$ flakes is calculated by the Wiedemann-Franz Law as $k_e = \sigma LT$, where σ is electrical conductivity, T is temperature, and $L = 2.44 \times 10^{-8}$ W Ω K^{-2} is the Lorenz number. Estimated k_e values for WTe$_2$ devices of varying thickness are shown in Figure 3.15, extracted for AlO$_x$-capped few-layer films. This electronic contribution in ultrathin devices is consistent with prior measurements on bulk, polycrystalline samples through a similar Wiedemann-Franz interpretation of crystal resistivity.[215] Combining these observations with our estimates above, we surmise that total thermal conductivity of WTe$_2$ is dominated by phonons, but with a non-negligible (10-30%) electronic contribution.
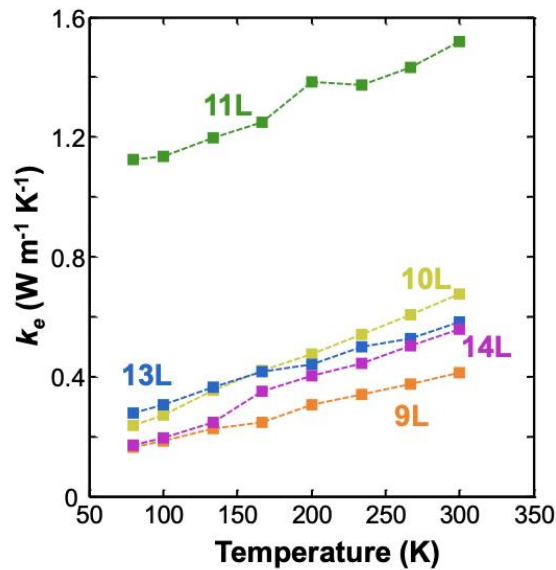
Figure 3.15. Electronic contribution (k_e) to the lateral thermal conductivity of WTe$_2$ multilayers vs. temperature. Estimates were made with the Wiedemann-Franz Law from the resistivity directly measured on our TLM structures.

3.4 Conclusion

Fitting a self-heating current model against experimental data, we extrapolated comparatively low thin-film thermal conductivities for WTe_2, down to ~3 $Wm^{-1}K^{-1}$. WTe_2 breakdown occurred at large current densities, nearly 50 MA/cm^2 for encapsulated, air-stable devices, suggesting technological viability of this 2D semimetal with low electronic work function and record magnetoresistance down to the ultimate thickness limit. Nanostructured WTe_2 thus emerges a promising candidate for multiple applications, including as 2D contacts to layered transistors and phase-change memory,[198,199,237] magnetic memory,[195,203] sensors and spintronics.[238,239]

Chapter 4

Thermal Properties of Crystalline AlN

Wide band gap (WBG) semiconductors such as GaN, Ga_2O_3 and AlN have attracted much interest due to their potential applications in power and radio-frequency (RF) electronics,[240, 241, 242] as well as deep ultraviolet (UV) photonics.[4,5] In these contexts, heat dissipation is important during high-power and high-temperature operation.[243, 244, 245] For example, power devices handle hundreds or even thousands of Volts, and the high power density leads to high operating temperature due to Joule heating, potentially diminishing the device performance and lifetime. Thermal cycling also causes fatigue and eventual failure in such devices.[246, 247]

Among WBG materials, AlN has a large direct band gap (~6.1 eV, almost twice that of SiC and GaN)[248, 249, 250] and one of the largest thermal conductivities. In this respect, as shown in Figure 4.1, AlN is among a rare class of materials that have both a large electronic band gap and a large thermal conductivity. AlN is widely used as buffer for GaN growth or as capping layer[251, 252] in power high-electron mobility transistors (HEMTs). However, many questions remain about the role of intrinsic defects and impurities which can occur during AlN growth. The contribution of individual phonon modes to thermal transport in AlN is also not well understood, which is important in establishing the dependence of AlN thermal conductivity on film thickness. (The contribution of electrons to thermal transport is negligible in WBG materials.)

Here, we elucidate these features of AlN thermal transport, by combining 3ω thermal measurements from 100 to 400 K, with thermal modeling using both analytical and *ab initio* techniques. We uncover that Al vacancies play an important role in limiting the thermal conductivity of present samples, and that phonons with long mean free paths (MFPs > 0.3 μm) contribute over 50% of the thermal conductivity at room temperature. This implies that the effective crystalline AlN thermal conductivity is strongly reduced in sub-micron films, and could be as low as ~25 $Wm^{-1}K^{-1}$ in a 10 nm thin film.

Results in this section were published in R. Xu, et al., (2019). "Thermal conductivity of crystalline AlN and the influence of atomic-scale defects", Journal of Applied Physics, **126**, (18), 185105, 2019

4.1 Summary of Thermal Conductivity of WBG

Figure 4.1 summarizes the room temperature thermal conductivities of several representative bulk solids with respect to their electronic band gaps. In this plot, a few trends emerge: First, among conducting, zero band gap materials, Cu and graphite (parallel to the basal plane) have the highest thermal conductivity.[15] (Cu is the only material on this plot whose thermal conductivity is dominated by electrons.) Second, among crystalline semiconductors the thermal conductivity weakly scales with the electronic band gap,[253,254,255] as both depend on the strength of the interatomic bonds and (inversely) on the atomic mass. Crystalline boron arsenide (BAs) is somewhat of an exception, with high thermal conductivity despite a relatively moderate electronic band gap, due to its unusual optical-acoustic phononic gap.[256,257] However, polycrystalline and

amorphous semiconductors (e.g. poly-Si and a-Si) have much reduced thermal

conductivity due to grain boundary and disorder scattering, respectively.[16,17] Third, many

electrical insulators, like sapphire, SiO_2 or SiN_x, have low thermal conductivity.[258,259,260]

Thus, only few materials have both large thermal conductivity and large electronic gap,

i.e. diamond,[15] hexagonal boron nitride (*h*-BN)[23] (parallel to the basal plane) and AlN, as

circled in Figure 4.1.
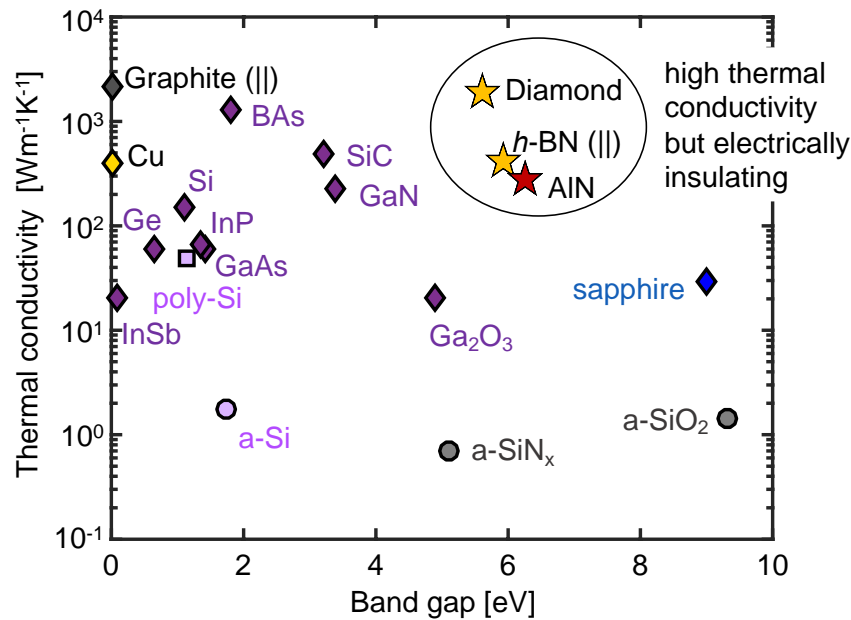
Figure 4.1. Room temperature thermal conductivities of different materials vs. their electronic band gaps. These include electrical conductors (e.g., graphite and Cu),[15] semiconductors (e.g., Si,[15-17] Ge,[15] InSb,[253] InP,[261] GaAs,[253] BAs,[256,257] SiC,[255] GaN,[21,22] and Ga_2O_3[262]), and some electrical insulators (e.g., diamond,[15] *h*-BN,[23] AlN,[24,25] sapphire,[258] amorphous SiO_2[259] and amorphous SiN_x[260]). The plot reveals that AlN lies in the same range as diamond and *h*-BN (star symbols), with both wide band gaps and high thermal conductivities. Isotopically purified samples may have higher thermal conductivity (values displayed are for natural isotopes). Diamonds are for crystalline, squares for polycrystalline, and circles for amorphous materials.

These three materials can provide excellent heat dissipation, especially in power

electronics where large amounts of heat is generated. These materials can also be doped,

to be used within or as parts of active device regions. The fundamental properties that

lead to their high thermal conductivity are small atomic mass, strong inter-atomic bonds, and simple crystal structure. However, the thermal properties of AlN have been studied relatively less[24,25] compared to other WBG materials, and details regarding the role of defects and phonon MFPs, particularly as a function of temperature and sample thickness, are still missing and thus the subject of this work.

4.2 Sample Preparation

The 3ω heater lines used in this work are 20 μm wide and 2 mm long (between the inner voltage probes). The lines were fabricated using photo-lithography. First, the AlN sample was spin-coated with a lift-off layer, LOL 2000, at 3000 rpm for 60 seconds, and pre-baked at 170°C for 7 minutes. Then, a photoresist, SPR 3612, was spin-coated on top at 5500 rpm for 40 s and pre-baked at 90°C for 60 seconds. A photomask was used to pattern the heater lines after 3 s exposure with an ultraviolet (UV) mask aligner lithography tool (Karl Suss). Afterwards, we carried out a post-exposure bake at 115°C for 60 s. We developed our sample by immersing it in MF-26A developer for 60 s. This was followed up by a soaking process in distilled water for 1 min and a gentle dry with compressed air. Then, we evaporated 5 nm Ti and 60 nm Pd using an e-beam evaporator (KJ-Lesker). Finally, the lift-off process was done by soaking the sample for 20 min in remover PG at 60°C.

4.3 3ω Method

The AlN bulk crystals (500 μm thick) were grown using physical vapor transport (PVT).[263] These samples have some imperfections, including Al vacancies and substitutional point defects[264] of oxygen (O), carbon (C) and silicon (Si) atoms, all in the

range of 0.4×10^{19} to 2×10^{19} cm^{-3}. Figure 4.2 shows a schematic of the 3ω setup, which is

a method for thermal conductivity measurements using AC-heated electrical lines that

also serve as thermometers, well described elsewhere.[259,265,266] Here, four-probe metal

lines (5 nm Ti followed by 60 nm Pd) are patterned by optical lithography and lift-off on

the AlN sample surface, serving as both heaters and thermometers, as shown in Figure

4.2(a). The electrical schematic of the 3ω measurement is displayed in Figure 4.2(b).
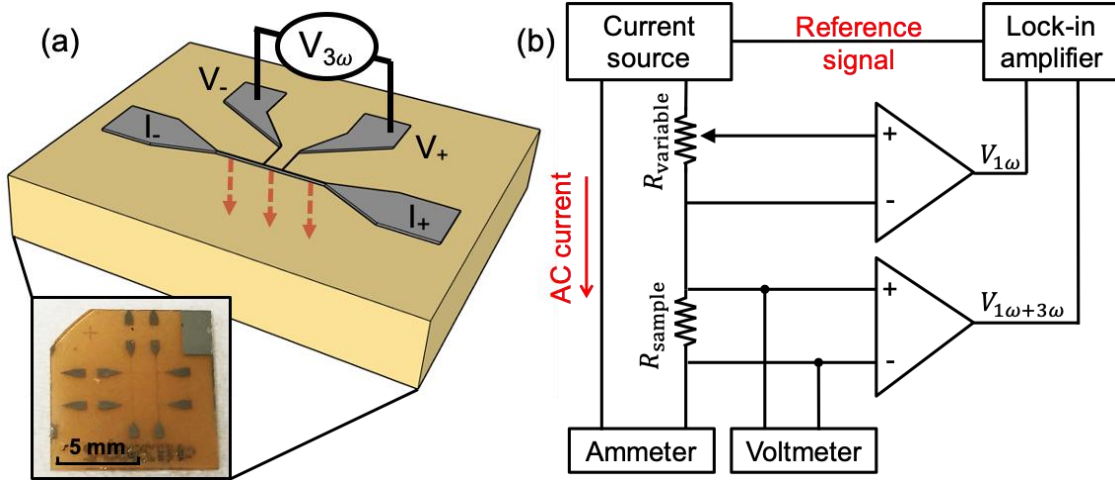
Figure 4.2. (a) Schematic of four-probe 3ω metal heater line on AlN single crystal sample. Heater consists of 5 nm Ti and 60 nm Pd, 20 μm wide and 2 mm long between the inner voltage probes. Arrows indicate heat flow direction. Inset shows an optical image of one of the AlN samples with patterned 3ω heaters. (b) Electronic circuit and instrument setup of the 3ω measurement.

As shown in Figure 4.3(a), an AC current ($I_{1\omega}$) at frequency ω is passed through the

heater, which causes a second harmonic temperature rise ($\Delta T_{2\omega}$) in the sample due to

Joule heating. The metal heater line resistance scales linearly with temperature from 100

K to 400 K, as $R = R_0[1 + \alpha(T - T_0)]$, where $\alpha = (5.5 \pm 0.2) \times 10^{-3}$ K^{-1} is the temperature

coefficient of resistance (TCR) and $T_0 = 100$ K, as in Figure 4.3(b). Due to this linear

relationship, the measured line resistance will also have a component ($R_{2\omega}$) that is a

second harmonic of the frequency. According to Ohm's Law, the heater output voltage has both 1ω and 3ω components, $V_{1\omega+3\omega} = R_{2\omega}I_{1\omega} = V_{1\omega} + V_{3\omega}$. We use a custom-built circuit board, schematically displayed in Figure 4.2(b), to separate $V_{3\omega}$ from $V_{1\omega+3\omega}$.[267] A potentiometer ($R_{variable}$) which has a low TCR of 50 ppm/K is adjusted to match the resistance of the sample heater (R_{sample}). When these two resistance values are matched, the voltage drop across the potentiometer is $V_{1\omega}$. Both $V_{1\omega}$ and $V_{1\omega+3\omega}$ are input to a lock-in amplifier, as shown in Figure 4.2(b), and $V_{3\omega}$ of the sample is the difference of these two voltage signals.

After collecting the 3ω voltage data, we analytically extract the thermal conductivity of the AlN sample as follows. The 3ω voltage $V_{3\omega}$ vs. frequency $f = \omega/(2\pi)$ is shown in Figure 4.3(c). The real part of $V_{3\omega}$ is plotted vs. $\ln(f)$ in Figure 4.3(d), displaying a linear variation whose slope S leads to the thermal conductivity k of the sample:

$$k = \frac{R\frac{dR}{dT}I_{1\omega}{}^3}{4\pi LS} \tag{4.1}$$

where L is the length and R is the resistance of the heater, $dR/dT = \alpha R_0$, and $I_{1\omega}$ is the magnitude of the AC current. We used heater dimensions that were 2 mm long (between inner voltage probes) and 20 μm wide, allowing us to treat the heater as a one-dimensional line.[265] Thus, heat flow is perpendicular to the top sample surface, which is in the same direction as the (few) dislocation line defects. The density of dislocation lines provided by the manufacturer[263] is in the range of 10^2 to 10^4 cm^{-2}, which is expected to have a small impact on the thermal conductivity.[268]
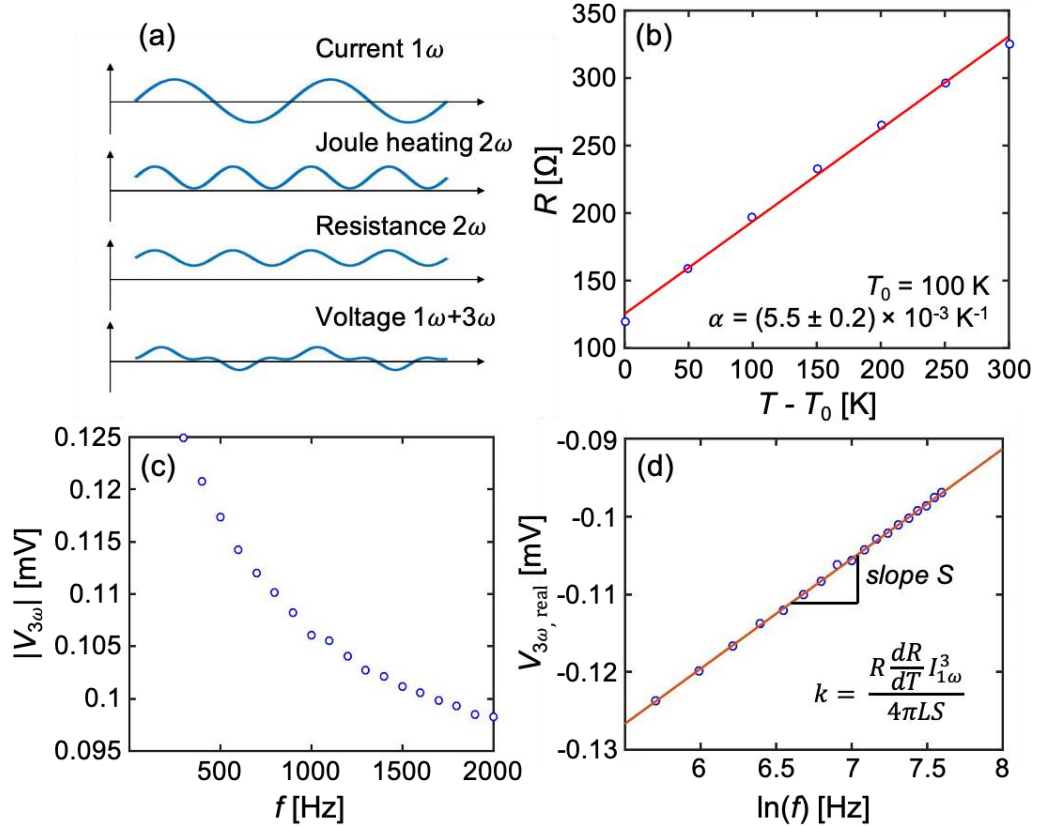
Figure 4.3. Analysis of 3ω measurement. (a) An AC current of frequency 1ω is passed through the heater line. Joule heating causes a second harmonic temperature rise, at 2ω, in the AlN sample underneath the heater. The metal heater resistance varies linearly with temperature as $R = R_0[1 + \alpha(T - T_0)]$, where α is the TCR and T_0 is the background temperature. Due to this linear relationship, the measured heater resistance will also have a 2ω component dependent on the sample temperature. Multiplied by the AC current input, the output voltage will have a component at 3ω. (b) TCR measurement fitting of sample I. Symbols are experimental data, solid line is the fit. (c) Measured $|V_{3\omega}|$ vs. frequency f. The real part of $V_{3\omega}$ is linear with $\ln(f)$, as shown in (d). Blue circles are measured data, and the thermal conductivity k is calculated using the slope of the linear fit (solid line).

The extracted temperature-dependent thermal conductivities of two single crystal AlN samples are plotted in Figure 4.4(a), from 100 K to 400 K. (Sample I shown in red diamonds and sample II shown in blue diamonds.) All measurements were performed in a vacuum probe station ($< 10^{-4}$ Torr). As a cross-check, we also used time-domain thermoreflectance (TDTR)[27,269,270] to measure the thermal conductivity of sample II at

67

room temperature [white diamond in Figure 4.4(a)], confirming the accuracy of our

measurements. The average thermal conductivity of these AlN samples ranges from 674

$\pm$ 56 Wm^{-1}K^{-1} at 100 K to 186 $\pm$ 7 Wm^{-1}K^{-1} at 400 K. At room temperature, the average

thermal conductivity is 237 $\pm$ 6 Wm^{-1}K^{-1} measured by the 3ω method and 247 $\pm$ 20 Wm^{-1}K^{-1} by TDTR (for sample II), these values being consistent with each other and similar

to others reported in the literature.[25,24]
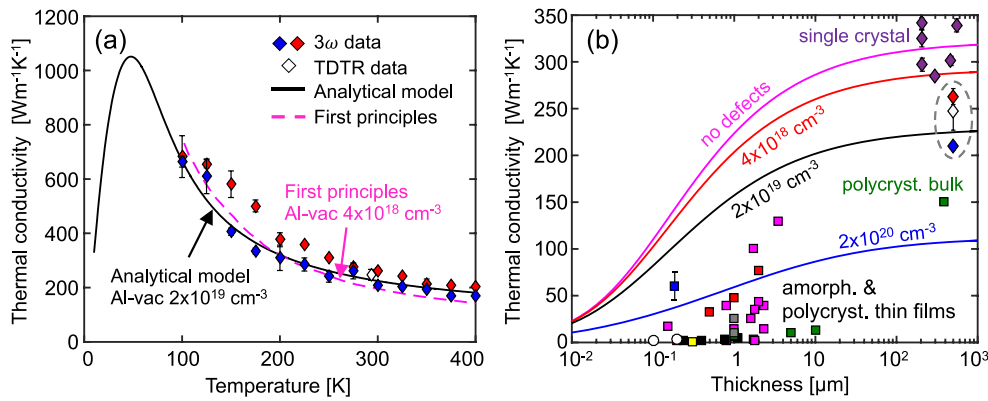
Figure 4.4. (a) Thermal conductivity of AlN vs. temperature. Square symbols are experimental data measured by our 3ω method. Diamond symbol is measured using TDTR. Dashed line is the model calculated by first principles simulation. Solid line is the thermal conductivity calculated by the analytical model. (b) Thermal conductivity of AlN vs. sample thickness, at room temperature. Solid lines are the theoretical calculation using different AlN defect densities. Diamond symbols are single crystal samples measured in this work [circled, colors matching panel (a)], those by Slack et al.,[24] and Rounds et al.[25] Square symbols are a polycrystalline bulk sample[271] (in green) and various polycrystalline films (grey: Kuo et al.,[272] purple: Duquenne et al.,[273] black: Zhao et al.,[274] red: Choi et al.,[275] blue: Yalon et al.,[32] yellow: Jacquot et al.,[276] green: Bian et al.[277]). White round symbols correspond to amorphous thin films by Zhao et al.[274] and Gaskins et al.[278]

We also report the thermal boundary conductance (TBC), $G_b \approx 117$ MWm^{-2}K^{-1} at room

temperature between AlN and the Al metal pad used in TDTR. The uncertainty due to this

TBC during 3ω measurements is negligible due to the large thermal diffusion length at

our frequencies (100 to 250 μm) but could play a role in thinner AlN films and devices.

(The Kapitza length of AlN corresponding to this TBC is $k/G_b \sim 2.2$ μm at room

temperature, meaning that heat flow across AlN films thinner than this value could be partly limited by the thermal resistance of their interfaces, $1/G_b$.)

4.4 Analytical Model

To analyze the contributions of different phonons and understand the underlying phonon scattering mechanisms in AlN, we turn to computational modeling, using two approaches: (1) we fit the measured data to an analytical model based on the Boltzmann Transport Equation (BTE), and (2) we perform full ab initio calculations. The analytical model [black solid line in Figure 4.4(a)] is calculated based on the simplified BTE, using the Debye approximation for the phonon dispersion of the acoustic modes:[268, 279]

$$k = \frac{1}{3} Cv\lambda = \frac{1}{3} \sum_s \int_0^{\omega_{max}} \hbar \omega g(\omega) \frac{df(\omega,T)}{dT} v^2 \tau(\omega) d\omega \qquad (4.2)$$

where λ is the phonon MFP, v is the phonon group velocity, C is the heat capacity, ω is the phonon frequency, ω_{max} is the Debye cutoff frequency, $g(\omega)$ is the phonon density of states, $f(\omega, T)$ is the Bose-Einstein distribution, $\tau(\omega)$ is the phonon scattering time, and s includes two transverse acoustic (TA) phonon modes and one longitudinal acoustic (LA) mode of AlN. The scattering rate is

$$\frac{1}{\tau} = \frac{1}{\tau_N} + \frac{1}{\tau_U} + \frac{1}{\tau_D} + \frac{1}{\tau_B} \qquad (4.3)$$

where the subscripts correspond to normal-process (N), Umklapp (U), defect (D), and boundary (B) scattering, respectively. Point defect scattering arises from impurity atoms of C, Si, and O, and from Al vacancies. As it turns out, the latter plays an important role in the reduction of thermal conductivity in this study, and the point defect scattering rate can be written as[280]

$$\frac{1}{\tau_D} = \frac{V}{4\pi v^3}\omega^4 \sum_i f_i \left(\frac{m-m_i}{m}\right)^2 \tag{4.4}$$

where V is the unit volume for wurtzite AlN given by $V = \sqrt{3}a^2c/8$, $a = 3.11$ Å and $c = 4.98$ Å are lattice constants,[281] f_i is the fractional concentration of the i-th impurity atom, m and m_i are the masses of original and i-th impurity atoms, respectively. In point defect scattering, Al vacancies play a dominant role because the mass difference is the atomic mass of the Al atom, which is much larger than the mass difference between Si and Al atoms or the difference among O, C, and N atoms. In AlN, C atoms often substitute for N atoms, while Si substitutes for Al.[264] In our analytical model, the Al vacancy density is used as a fitting parameter, with a fitted value of $\sim 2\times 10^{19}$ cm^{-3}, which is within the range quoted by the sample manufacturer.[263] An important "shortcut" used here for treating vacancy scattering relies on a previous study by Katcho *et al.*[282] which showed good agreement with first principles calculations if the vacancy mass difference is taken as six times the mass of the missing atom. This is justified because vacancies lead to larger local distortion in the crystal compared to substitutional defects, due to bond breaking and atomic rearrangements, and these distortions contribute to enhanced phonon scattering.

4.5 First Principles Calculations

We also employ a second modeling approach, using first principles calculations, based on the BTE coupled with density functional theory (DFT). This method has previously shown good agreement with experiments for a range of other materials.[283,284,285] The phonon frequencies and anharmonic phonon scattering rates for AlN are computed using harmonic (2nd order) and anharmonic (3rd order) interatomic force constants (IFCs) for a

5×5×5 supercell of AlN wurtzite structure (space group P6$_3$mc). We follow the finite

displacement method as implemented in phonopy[286] and thirdorder.py,[287] extracting the

2nd and 3rd order IFCs respectively from interatomic forces. These interatomic forces

and the optimized structural parameters for wurtzite AlN are calculated using the DFT

package VASP.[288] Similar to the analytic approach described earlier, the phonon

scattering rate with Al vacancies is computed using Eq. 4.4, where the mass difference is

six times the original atomic mass.[282] All contributions to phonon scattering rates and

finally the thermal conductivity are calculated using the almaBTE package,[289] where the

BTE is solved using an iterative scheme, and the obtained thermal conductivity is shown

with a purple dashed line in Figure 4.4(a), displaying good agreement with the

experiments.

We note that the analytic and first-principles calculations fit the thermal conductivity data

with different Al vacancy concentrations, i.e. 2×10^{19} cm^{-3} and 4×10^{18} cm^{-3},

respectively, although both are in the range quoted by the sample manufacturer.[263] This

difference is due to the different anharmonic scattering rates implemented in the two

approaches. In the analytical model, anharmonic scattering rates for both normal and

Umklapp processes follow the simple ω^2 behavior.[24] The anharmonic scattering rates in

the ab initio calculations show deviation from this behavior at both low and high

frequencies.[284, 290] However, we note that the five-fold difference in vacancy

concentration causes only about ~25% change of expected bulk thermal conductivity

[Figure 4.4(b)], illustrating the relative (in)sensitivity of this parameter in this range.

4.7 Thickness Dependence of Thermal Conductivity

Figure 4.4(b) examines the AlN thermal conductivity dependence on vacancy concentration and film thickness. The thickness dependence with different vacancy concentrations has not been previously analyzed before, although (as we will see) AlN is subject to strong phonon-boundary scattering effects due to the large phonon MFP in this material. In other words, the thermal conductivity of sub-micron thin AlN films is strongly reduced, and thin buffer films of this material are expected to have much lower effective thermal conductivity than the bulk material. This is an *intrinsic* effect, in addition to the earlier observation of *extrinsic* thermal impedance contribution from interfaces (like Al/AlN) of sub-micron thin films.

Figure 4.4(b) displays the calculated thickness-dependent thermal conductivity with different defect densities using solid lines, all at room temperature. For comparison, experimental data on various single crystal films are shown in diamond symbols, including this work and Refs. [25,272,291]. Square symbols correspond to one bulk polycrystalline AlN measured with TDTR[271] and other polycrystalline films measured by various groups. [32,272,273,274,275, 276,277] Round symbols correspond to amorphous thin films by Zhao *et al.*[274] and Gaskins *et al.*[278] Due to significant disorder scattering, amorphous films have much lower thermal conductivity than (poly-)crystalline films, as expected. Thus, when using AlN thin films as buffer or capping layers[251,252] in power devices, highly crystalline, low-defect films provide better heat dissipation.

However, Figure 4.4(b) also reveals that the thermal conductivity of all films ~10 μm or thinner is expected to be decreased by ~10% or more from the bulk value. The effective thermal conductivities of 10 nm and 100 nm thin AlN films are predicted to be just ~25 Wm^{-1}K^{-1} and ~110 Wm^{-1}K^{-1} at room temperature (less than 1/12 and 1/3 of the best bulk material values), respectively, even in defect-free films, due to strong phonon-boundary scattering.

4.8 Accumulated Thermal Conductivity

To understand the physical origin of the strong phonon-boundary scattering in AlN thin films, we turn to Figure 4.5. First, in Figure 4.5(a) we plot the calculated thermal conductivity as a function of the cumulative contributions of phonons across the range of MFPs expected in such crystals. The accumulated thermal conductivity is the thermal conductivity contribution from all phonons with MFP below a given value:[292]

$$k_{\text{accum}}(\lambda_0) = \frac{1}{3}\sum_s \int_0^{\lambda_0} C(\lambda)\, v(\lambda)\lambda d\lambda \qquad (4.5)$$

where C is the heat capacity as a function of MFP, since $C(\omega) = \hbar\omega g(\omega)\, df(\omega, T)/dT$ and $\lambda = v\tau(\omega)$. The integral is taken from 0 to λ_0, and thus k_{accum} is the thermal conductivity of phonons with MFP $\leq \lambda_0$, here at room temperature. The contributions of both LA and TA modes are shown in Figure 4.5(a), the LA mode contribution being larger due to its larger phonon group velocity. The total thermal conductivity is the sum of contributions from one LA and two TA modes.

To gain additional insight, we normalize the accumulated thermal conductivity by the bulk value ($k_{\text{accum}}/k_{\text{bulk}}$) in Figure 4.5(b), for the "perfect crystal" with zero defects. Our

calculations estimate that 50% of the AlN bulk thermal conductivity is contributed by phonons with MFPs > 0.3 µm, and 10% is contributed by phonons with very long MFPs > 7 µm, at room temperature. These values are comparable to the median MFP ~ 2.5 µm of Freedman *et al.*,[292] obtained by broadband frequency domain thermoreflectance (BB-FDTR) which considered only Umklapp phonon scattering (vs. the four scattering mechanisms included here). Taken together, these findings explain why "size effects" on the thermal conductivity of AlN are expected to be strong in sub-micron films at room temperature, and noticeable even in sub-10 µm thin films. In other words, the effective thermal conductivity of AlN is strongly reduced in films with thickness comparable to or smaller than such long phonon MFPs, as illustrated earlier in Figure 4.4(b).

We define the phonon MFP corresponding to 50% or 90% of the cumulative heat conduction as MFP(50% or 90%), plotting it at higher temperatures in Figure 4.5(c). As the temperature increases, phonon occupation and phonon-phonon scattering increase, thus MFP(50% or 90%) decreases. This implies that "size effects" on the thermal conductivity of AlN become somewhat less important at elevated temperature, i.e. the reduction of thermal conductivity in thin films of this material will be less pronounced vs. the bulk value at that temperature. The thermal conductivity of thin films at high temperatures will also experience a competition between phonon-phonon and phonon-boundary scattering. This is illustrated in Figure 4.5(d), which shows the expected temperature dependence of thermal conductivity from bulk to 1 µm, 0.1 µm, and 10 nm thin films. The increasing role of phonon-boundary scattering lowers the thermal conductivity, but also renders it less temperature-sensitive in the thinnest films, and less dependent on film thickness at the highest temperatures. The exact details of boundary

scattering processes will depend, in part, on the particular surface roughness of such AlN films. These details were previously studied for Si, Ge and GaAs thin films and nanowires,[293,294] and should be the subject of future work for AlN.
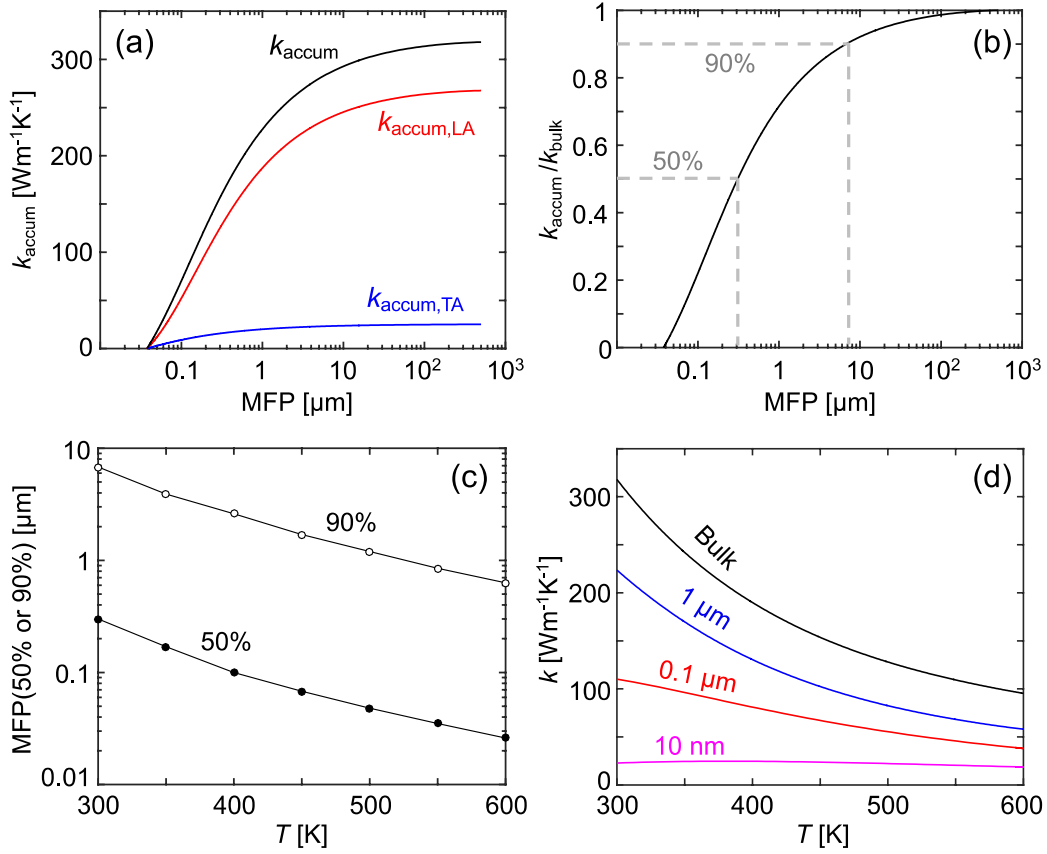
Figure 4.5. (a) Calculated accumulated thermal conductivity vs. phonon MFP for AlN bulk at room temperature, comparing the total and its longitudinal acoustic and transverse acoustic phonon contributions, $k_{accum} = k_{accum,LA} + 2k_{accum,TA}$. (b) Normalized accumulated thermal conductivity k_{accum} / k_{bulk} at room temperature, where k_{bulk} is the maximum value of k_{accum}. Phonons with MFP larger than 0.3 μm (or 7 μm) are estimated to contribute 50% (or 10%) of the heat conduction, as shown by dashed lines. (c) Calculated temperature dependence of MFP(50% or 90%) for AlN. (d) Expected temperature dependence of thermal conductivity for different film thicknesses, as labeled. Thinner films have weaker temperature dependence, due to the predominance of boundary scattering. All calculations (a-d) in this figure assume defect-free samples.

4.9 Conclusion

In summary, we have performed 3ω measurements of thermal conductivity in single crystal AlN samples, from 100 K to 400 K. We compared these results with analytic and ab initio simulations, to estimate the impurity defect densities. Aluminum vacancies play the most important role among all atomic scale defects, due to the large atomic mass mismatch, which can be analytically captured by modeling phonon-vacancy scattering using six times the mass of the missing atom. The accumulated thermal conductivity shows that phonons with MPFs larger than 0.3 μm (or 7 μm) contribute to 50% (or 10%) of heat conduction at room temperature. This implies that AlN thin films and devices with sub-micron features will exhibit strongly reduced effective thermal conductivity compared to the bulk value, even in the absence of point defects. These results are essential for the understanding of thermal transport in AlN thin films and devices over a broad temperature range, for applications in power electronics and deep-UV lasers.

Chapter 5

Raman Thermometry of GaN Devices with Diamond Heat Spreaders

GaN high electron mobility transistors (HEMTs) have been widely used in power electronics due to its high critical breakdown field and 2DEG density.[241, 242] Radio frequency (RF) HEMTs based on GaN have also been commercialized and deployed in cellular base stations.[295] GaN bulk has a thermal conductivity around 230 $Wm^{-1}K^{-1}$ at room temperature.[21,22] However, when used in HEMT devices, GaN thickness is usually reduced to a few hundred nanometers.[242] Due to boundary scattering, its thermal conductivity is expected to be reduced significantly. One important application of GaN HEMTs is in the field of power electronics. Power electronics are operated at high temperature due to high input power and Joule heating.[241] Therefore, it is crucial to provide better heat dissipations in order to achieve and maintain good device behaviors. To this end, here we use polycrystalline diamond layers as heat spreaders on top of GaN devices. This poly-diamond layer provides additional heat paths to reduce the channel temperature. Raman thermometry is used to monitor temperature when devices are under electrical bias.

5.1 Device Structure

A two-terminal device structure (shown in Figure 5.1) is used in this work to study the thermal properties of the diamond-integrated GaN device.[296] This device structure from

top to bottom includes 20 nm SiN / 320 nm n-GaN / 120 nm unintentionally doped (UID) GaN / 400 μm sapphire substrate. The channel layer is n-type GaN doped by Si with a dopant density of 10^{18} cm^{-3}. A 650 nm thick polycrystalline diamond layer is grown by chemical vapor deposition (CVD) on top of SiN layer. Growth temperature is around 650 °C.[297] Ohmic contact is formed by a stack of evaporated metals (from bottom to top): 20 nm Ti / 120 nm Al / 20 nm Ni / 50 nm Au.
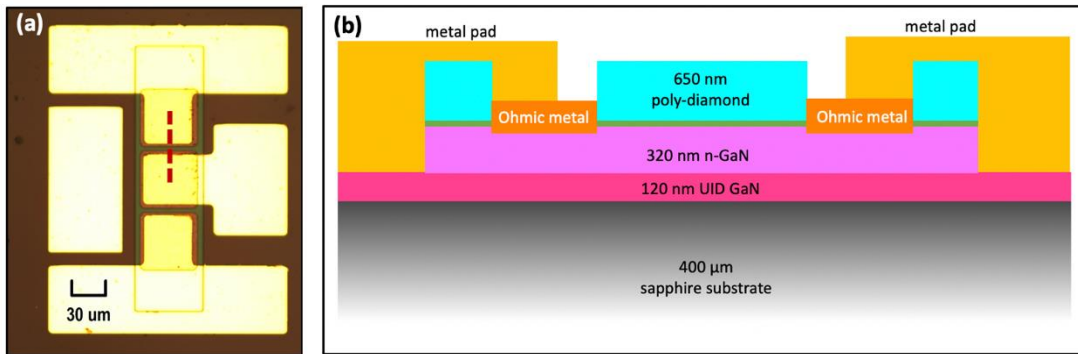
Figure 5.1. (a) Top-down optical image of two identical devices ($L = 7$ μm, $W = 50$ μm), (b) Cross-section schematic of GaN 2-terminal device along the red dashed line direction in (a). From top to bottom: 650 nm poly-diamond (blue) / 20 nm SiN (green) / 320 nm n-GaN (purple) / 120 nm unintentionally doped (UID) GaN (pink) / 400 μm sapphire substrate (grey). Ohmic metal is formed by a stack of metals (from bottom to top): 20 nm Ti / 120 nm Al / 20 nm Ni / 50 nm Au. Metal pad is 200 nm Au.

5.2 Raman Thermometry Measurement

Raman spectroscopy can be used to determine the temperature of a material. At high temperature, Raman peaks red shift due to thermal expansion. With Raman thermometry, the temperature is measured optically, and the power is applied electrically. The input power in electrical heating experiments is well defined. Calibration curves (peak position *versus* temperature) are obtained before the measurements under electrical bias. When the

devices are under electrical bias, Raman peak positions are measured again and then compared to the calibration curves to extract temperature.

Raman thermometry has already been widely used in Si,[298,299] TMDs[33,44,13] and WBG materials.[300,301,302] In this study, we perform Raman thermometry on GaN devices. In order to extract accurate temperature information, the power dissipation in the channel needs to be known. Total power input (P) includes the power dropped in the channel ($P_{channel}$) and the power dissipated at the contacts ($P_{contact}$). TLM extraction (shown in Figure 5.2) is done to obtain contact resistance ($2R_C$). Plotting the measured resistance, $RW = R_S L + 2R_C$, yields a slope R_S as the intrinsic sheet resistance and the y-axis intercept $2R_C$ as the total contact resistance (here, adjusted by width). Thus, the power dropped in the channel is calculated as

$$P_{channel} = I \times (V - I \times 2R_C/W) \qquad (5.1)$$

where I is input current, V is input voltage and W is channel width.
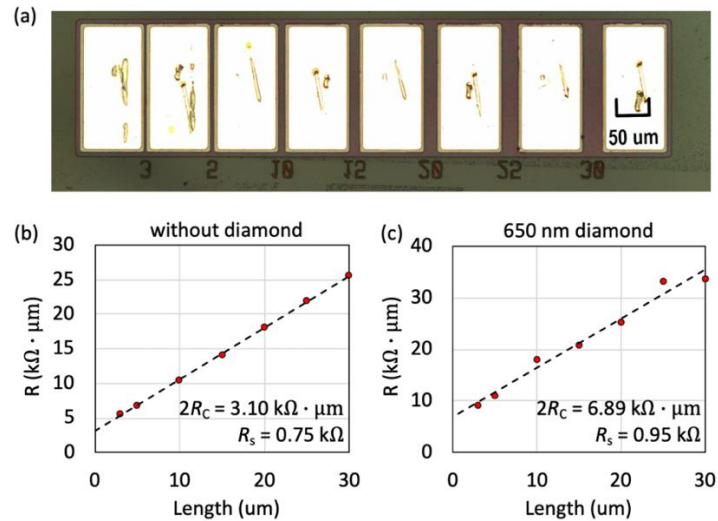
Figure 5.2. (a) Top-down optical image of the TLM structure. Channel lengths are 3 μm, 5 μm, 10 μm, 15 μm, 25 μm and 30 μm. TLM extraction on GaN devices: (b) without diamond capping layer and (c) with 650 nm poly-diamond capping layer. Y-axis intercept is the total contact resistance ($2R_C$).

79

Temperature dependent Raman spectra (Figure 5.3) of GaN and the diamond capping are simultaneously obtained using a Horiba LabRam Raman system. Samples are set on a Linkam hot stage during temperature calibration, in air. GaN and diamond Raman peak positions are plotted against temperature with linear fitting, shown in Figure 5.4.
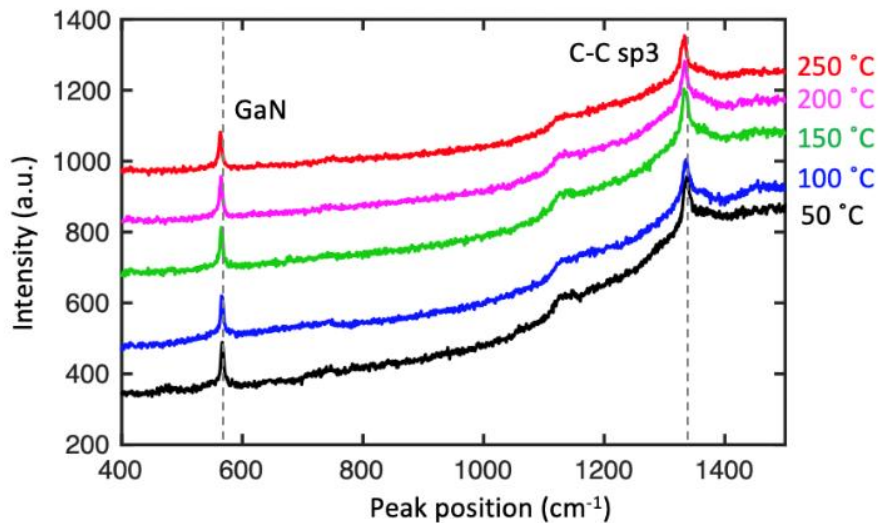
Figure 5.3. Temperature dependent Raman spectra of GaN peak and C-C sp^3 in polycrystalline diamond from 50 °C too 250 °C. Data are vertically offset to allow easier distinction. Note: raw data are shown, but baseline was subtracted for peak fitting and temperature calibration.
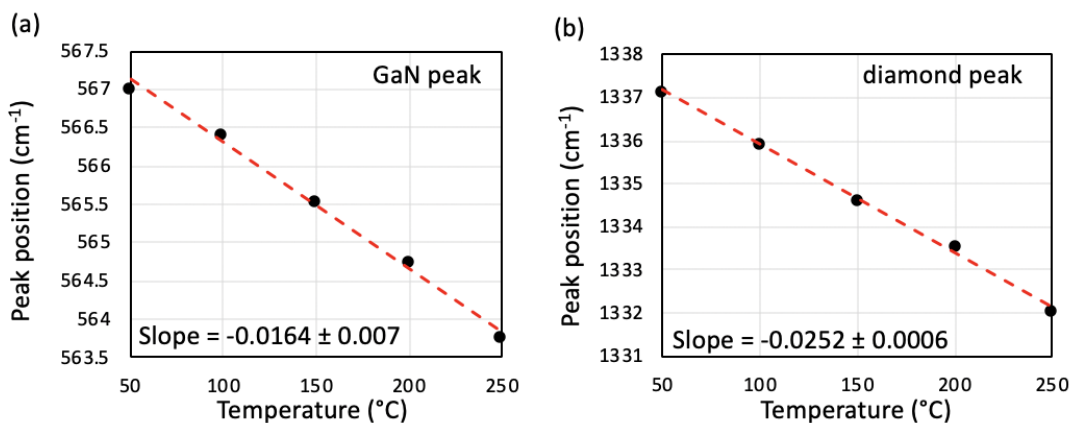
Figure 5.4. Peak position *versus* temperature with linear fitting of (a) GaN and (b) poly-diamond.

After temperature calibration, Raman measurements are done with the devices under

electrical bias. Temperature rise (ΔT) of the reference device (without diamond capping)

and the one with 650 nm poly-diamond layer are plotted *versus* the power dissipation in

the channel ($P_{channel}$), shown in Figure 5.5. Raman peaks are measured at the center of the

channel. Temperature values are extracted using the calibration curves in Figure 5.4.

Under the same power input, the device with poly-diamond capping has lower

temperature than the device without diamond capping. This is due to the additional heat

dissipation paths between the diamond layer and metals, as well as lateral heat spreading

in the device width direction. The error bars in measured temperatures are from the

uncertainty in Raman measurements and peak fitting. For the device with poly-diamond

capping, the GaN layer and diamond layer have no detectable temperature difference,

within the error bars of the measurement.
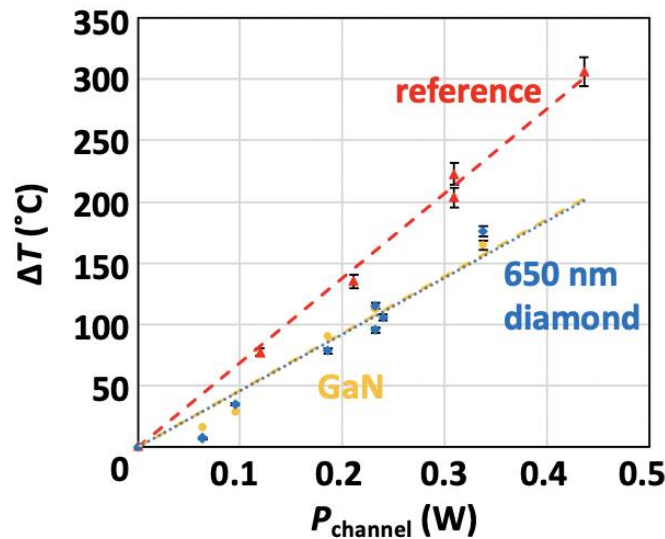
Figure 5.5. Temperature rise versus power dissipated in the middle of the GaN channel
(device dimensions: $L = 7$ μm, $W = 50$ μm). Red dots show the temperature values of the
reference sample (without diamond layer), which are extracted from the GaN peak. Blue
and yellow dots show the temperature of the diamond and GaN layers, from the device
with 650 nm diamond capping layer.

Another application of Raman thermometry could be to verify fabrication variability. The total contact resistance ($2R_C$) is extracted in TLM measurement, but we cannot separate the values of two contacts in TLM extraction. However, we are able to use Raman thermometry to monitor the temperature near each contact. Metal contacts are heated up by Joule heating under electrical bias. With the same current flow, the hotter contact has higher electrical contact resistance. We measure three positions in the GaN channel (at the center and near each contact) on the reference sample (without diamond capping) to extract temperature values. We also change the polarization of voltage bias to observe whether there is thermoelectric effect at the contacts.[303]

Figure 5.6 shows the extracted results of a 5 µm long and 200 µm wide device measured at 70 °C (ambient temperature). The right contact is always hotter than the left contact regardless of the direction of current flow and the power input level (shown in Figure 5.6(c)), which indicates that there is no observable thermoelectric effect at these contacts, and Joule heating dominates in this device structure. Thus, for the device shown in Figure 5.6, the right contact has higher electrical resistance than the left one. From Figure 5.6(c), we estimate that the temperature of the right contact is ~14% higher than the temperature of the left contact (averaged over all measurements), which indicates that the resistance of the right contact of this device is also ~14% higher than the left. The total contact resistance of this device ($L = 5$ µm, $W = 200$ µm) is 15.5 Ω. Thus, the right contact resistance is around 7.2 Ω and the left contact resistance is around 8.3 Ω. We have measured three devices and observed uneven contacts in all of them with a range of 7% to 16% differences between contacts. The possible reasons of uneven contacts might be

fabrication variability, e.g. defects in the metal contacts, poor adhesion during metal deposition, or defects in the GaN channel layer.
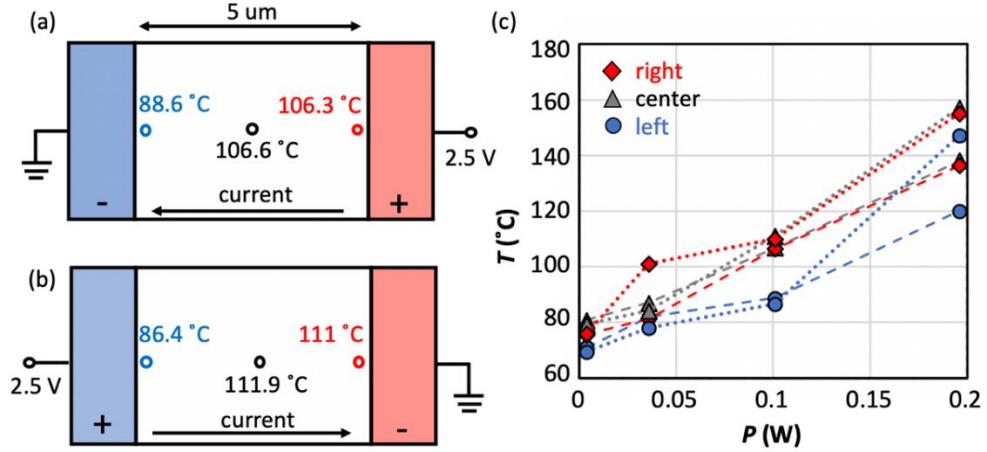
Figure 5.6. Extracted temperatures of a two-terminal GaN device ($L = 5$ μm, $W = 200$ μm) at 2.5 V bias with reverse and forward current flow direction, shown in (a) and (b). Ambient temperature is 70 °C. The right contact was always hotter for this device, regardless of current flow direction. (c) Measured temperature vs. total power: right contact temperatures are shown in red diamond symbols, center temperatures are shown in grey triangular symbols, and left contact temperatures are shown in blue round symbols. Symbols connected by dashed lines represent current flowing from right to left as shown in (a). Symbols connected by dotted lines represent current flowing from left to right as shown in (b). All lines are guides to the eye. Some variability is introduced by the positioning of the laser spot near the metal-GaN contact.

5.3 Analytical Model

To understand the experimental results, we use an analytical model for comparison. Equivalent thermal circuit is shown in Figure 5.7(a). Maximum temperature (T_{max}) is at the top surface of n-GaN layer and ambient temperature (T_0) is at the bottom of the sapphire substrate. Total thermal conductance of the reference device is calculated as:

$$g^{-1} = \frac{R_n}{W} + \frac{R_{UID}}{W} + \frac{R_{int}}{W} + \frac{1}{2k_{sub}}\sqrt{\frac{L}{W_{eff}}} \tag{5.2}$$

The equation above represents the series combination of four terms: the thermal resistance of n-type GaN, the thermal resistance of UID GaN, the thermal resistance of the UID GaN–sapphire interface, and the spreading thermal resistance into the sapphire substrate. In this simple model, the interface thermal resistance is $R_{int} = 10^{-8}$ m^{2}K/W, the thermal conductivity of the sapphire substrate is $k_{sub} = 34$ Wm^{-1}K^{-1},[258] thermal conductivity of $t_n = 120$ nm GaN layer is $k_n = 30$ Wm^{-1}K^{-1}, and the thermal conductivity of $t_{UID} = 320$ nm GaN is $k_{UID} = 60$ Wm^{-1}K^{-1},[304] which are significantly reduced from the bulk value due to strong boundary scattering. The thermal resistances (per unit area) are $R_n = t_n / k_n$ and $R_{UID} = t_{UID} / k_{UID}$. The effective width of the heat dissipation path through the sapphire substrate is $W_{eff} \approx W + 2(t_n + t_{UID}) \approx W$, because the thickness of n-GaN layer and UID-GaN layer are negligible compared to device width. The result of this simple analytical model is shown with the grey dashed line in Figure 5.7(b), which is consistent with the measured data.
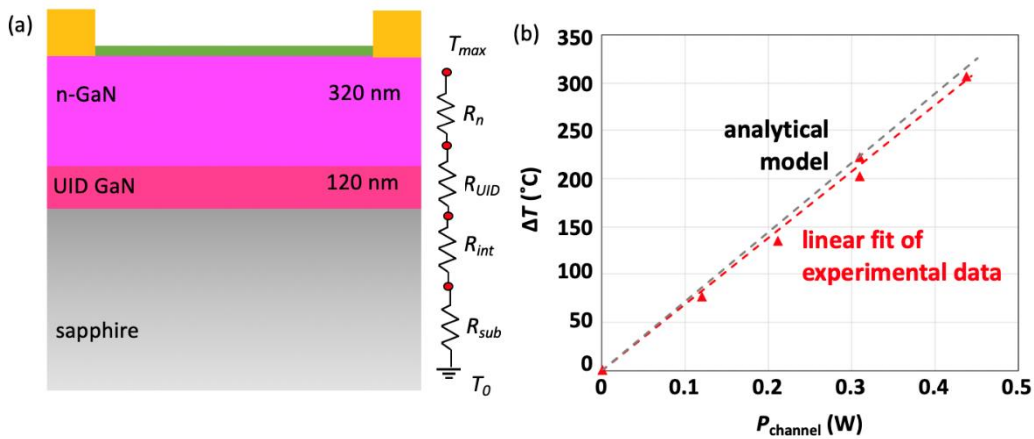
Figure 5.7. (a) Equivalent thermal circuit of the reference sample without diamond capping. (b) Temperature rise (ΔT) of the reference sample (without diamond) *versus* power dissipated in the channel ($P_{channel}$). ΔT is the difference between the maximum temperature in the channel (T_{max}) and ambient temperature (T_0). Analytical model is shown in grey dashed line. Red symbols show experimental results of the reference sample and red dashed line is the linear fit of the experimental data.

5.4 Finite Element Simulation

To validate the experimental results and analytic model, we have also used COMSOL simulation results as comparison (shown in Figure 5.8). With input electrical power at 0.2 W, the maximum channel temperature is shown for the reference sample (without diamond) and the poly-diamond integrated device. The polycrystalline diamond in our sample is expected to have non-negligible anisotropy, due to its grain structure.[296] We compare our diamond film with the poly-diamond films measured by Sood *et al.*, which has similar grain size and thickness, and we choose to use thermal conductivity with an in-plane value ~77 $Wm^{-1}K^{-1}$ and a cross-plane value ~210 $Wm^{-1}K^{-1}$.[27] The Ohmic contact is a stack of metals (20 nm Ti / 120 nm Al / 20 nm Ni / 50 nm Au). Thermal conductivities of thin metal films are significantly reduced compared to the bulk due to boundary scattering. Therefore, we use 2 $Wm^{-1}K^{-1}$, 225 $Wm^{-1}K^{-1}$, 45 $Wm^{-1}K^{-1}$ and 120 $Wm^{-1}K^{-1}$ for Ti,[305] Al,[306] Ni[307] and Au thin films,[308] respectively.
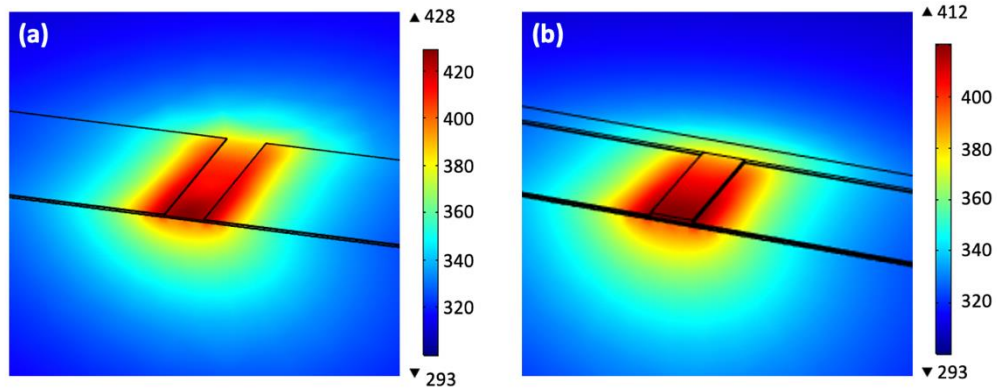
Figure 5.8. Temperature distribution from COMSOL simulation with 0.2 W electrical power applied to a 2-terminal GaN device (dimensions $L = 7$ μm, $W = 50$ μm, same with the measured device). Ambient temperature is 293 K. (a) reference sample without poly-diamond capping, (b) capped with 650 nm poly-diamond. All simulations are done on half of a device (one device is divided into halves along the channel length direction).

Other parameters including device dimensions, thermal conductivities of n-GaN and UID-GaN, and TBC are the same with the input values of the analytical model. In our COMSOL simulation, the bottom surface of the sapphire is set to be ambient temperature (293 K). The top, left and right boundaries of the device are set to be adiabatic condition, because the heat loss through convection and radiation is negligible. The reference device has a maximum temperature (T_{max}) of 428 K and its temperature rise (ΔT) is 135 K, while the diamond-capped device has a maximum temperature of 412 K which corresponds to $\Delta T = 119$ K. Finite element simulation confirms the temperature reduction by adding a poly-diamond top capping layer. This diamond structure helps to dissipate heat from the GaN channel into the contacts. It also spreads the heat laterally along the width direction. This diamond heat spreader layer helps to reduce T_{max} by ~13%. Therefore, our diamond integrated GaN device has better heat dissipation capability compared to the traditional GaN device without top diamond capping layer.

5.5 Conclusion and Future Outlook

Poly-diamond top capping layer reduces GaN device channel temperature by adding additional heat paths. Raman thermometry measurement results are verified by analytical model and COMSOL simulation. However, this device is based on a simplified 2-terminal device structure. Future study should be focused on GaN HEMT structure under AC bias.

Chapter 6

Conclusions and Perspectives

This chapter summarizes the contributions of this dissertation and discusses future research ideas.

6.1 Conclusions

In this dissertation, we investigated thermal transport in 2D materials and WBG materials, with a focus on WTe_2, AlN and GaN. We combined experimental measurements, finite element simulations and analytical models to perform a comprehensive study. We also summarized thermal conductivity, thermal boundary conductance and thermoelectric properties of 2D materials, including graphene, TMDs, h-BN and etc.

We have summarized the thermal properties of 2D materials and we found that the thermal conductivities of 2D materials have strong anisotropy which is given by the structure of such materials and have a very large range (3 ~ 4 orders of magnitude) which is partly due to the huge difference of the molecule masses. These may lead to different potential applications, such as heat spreader (e.g. graphene), heat isolation layer (e.g. amorphous or disordered WSe_2). 2D materials also have a large range of band gaps, from metal (graphene), semimetal (WTe_2), semiconductors (e.g. MoS_2, $MoSe_2$, $MoTe_2$, WS_2) to electrical insulators (BN). By stacking those materials, we can further engineer their

thermal (as well as electrical) properties, which do not exist in other 3D bulk materials in nature. TBC plays a much important role in 2D materials and devices comparing to conventional 3D material. Seebeck coefficient can be increased by gating the material and minimizing electrical conductivity, but these will harm the figure of merit (*ZT*). To realize 2D material based thermoelectrics, stacking will be important.

We investigated the thermal conductivity of WTe_2 by fitting a self-heating current model against experimental data. We extrapolated comparatively low thin-film thermal conductivities for WTe_2, which is as low as ~3 $Wm^{-1}K^{-1}$ in-plane, at room temperature. We found that WTe_2 breakdown occurred at large current densities, nearly 50 MA/cm^2 for encapsulated, air-stable devices, suggesting technological viability of this 2D semimetal with low electronic work function and record magnetoresistance down to the ultimate thickness limit.

We studied the thermal limitations of current density in WTe_2 devices, using experiments, analytical model, and finite element simulations. The low thermal conductivity of WTe_2 limits heat spreading in such devices, but using higher thermal conductivity capping layers or decreasing SiO_2 substrate thickness can improve the maximum current density of WTe_2.

To study the thermal properties of WBGs, we performed 3ω measurements on single crystal AlN samples. We compared these results with analytic and ab initio simulations, to estimate the impurity defect densities. Aluminum vacancies play the most important

role among all atomic scale defects, due to the large atomic mass mismatch, which can be analytically captured by modeling phonon-vacancy scattering using six times the mass of the missing atom. The accumulated thermal conductivity shows that phonons with MPFs larger than 0.3 μm (or 7 μm) contribute to 50% (or 10%) of heat conduction at room temperature. This implies that AlN thin films and devices with sub-micron features will exhibit strongly reduced effective thermal conductivity compared to the bulk value, even in the absence of point defects. These results are essential for the understanding of thermal transport in AlN thin films and devices over a broad temperature range, for applications in power electronics and deep-UV lasers.

To further our study on WBG materials, we also performed Raman thermometry measurements on 2-terminal GaN devices. We use both experimental results, analytical model and finite element simulation to show that poly-diamond capping layer reduces GaN channel temperature.

6.2 Future Work

To continue our study on WTe_2, future work should focus on device level experimental measurements and electro-thermal simulations, including using WTe_2 as 2D contact to layered transistors, or electrodes in phase change memory. Besides studying a single 2D materials, it becomes increasingly interesting to investigate the effective thermal conductivity and Seebeck coefficient of a stacked layer using different 2D materials. Both experimental measurements and theoretical calculations are needed in this area.

For WBG study, future work should focus on the thickness dependency of thermal conductivity, in order to gain higher confidence in the obtained data and further "fill in" the missing data in sub-micro regime. While 3ω method was used to obtain cross-plane thermal conductivity of AlN, in-plane thermal conductivity measurements could be pursued using a suspended membrane platform. We note this is an important measurement as well, because the grain structure of the AlN thin films is expected to be different in the "vertical" vs. "lateral" direction, thus the thermal conductivity will also be anisotropic. Those future measurement will provide a complete study of the anisotropic thermal conductivity of AlN.

System-level simulations to estimate the improvement in reliability of AlN and h-BN heat spreaders could be another future area. This could be done by both finite element simulations and analytical models.

Future work should also be carried out to study GaN HEMTs. Those devices will be used in RF applications. Novel thermal measurement should be designed to measurement device operation temperature under AC bias.

References

1   G. E. Moore, (McGraw-Hill New York, NY, USA:, 1965).
2   C. Jacoboni, C. Canali, G. Ottaviani, and A. A. Quaranta, Solid-State Electronics **20** (2), 77 (1977).
3   B. Monemar, Physical Review B **10** (2), 676 (1974).
4   S. Islam, V. Protasenko, K. Lee, S. Rouvimov, J. Verma, H. Xing, and D. Jena, Appl. Phys. Lett. **111** (9), 091104 (2017).
5   D. Bayerl, S. Islam, C. M. Jones, V. Protasenko, D. Jena, and E. Kioupakis, Appl. Phys. Lett. **109** (24), 241102 (2016).
6   C. H. Kim, K.-S. Sohn, and J. Jang, Journal of applied physics **81** (12), 8084 (1997).
7   M. Pedram and S. Nazarian, Proceedings of the IEEE **94** (8), 1487 (2006).
8   G. Chen, *Nanoscale energy transport and conversion: a parallel treatment of electrons, molecules, phonons, and photons*. (Oxford University Press, 2005).
9   T. M. Tritt, *Thermal conductivity: theory, properties, and applications*. (Springer Science & Business Media, 2005).
10 M. Kaviany, *Heat transfer physics*. (Cambridge University Press, 2014).
11 D. R. Lide, *Handbook of Chemistry and Physics*, 87 ed. (CRC Press, Boca Raton, FL, 1988).
12 E. Pop, Nano Research **3** (3), 147 (2010).
13 E. Yalon, O. B. Aslan, K. K. Smithe, C. J. McClellan, S. V. Suryavanshi, F. Xiong, A. Sood, C. M. Neumann, X. Xu, and K. E. Goodson, ACS Applied Materials & Interfaces **9** (49), 43013 (2017).
14 R. L. Xu, M. Muñoz Rojo, S. Islam, A. Sood, B. Vareskic, A. Katre, N. Mingo, K. E. Goodson, H. G. Xing, and D. Jena, Journal of Applied Physics **126** (18), 185105 (2019).
15 C. Y. Ho, R. W. Powell, and P. E. Liley, J. Phys. Chem. Ref. Data **1** (2), 279 (1972).
16 H. Wada and T. Kamijoh, Japanese J. of Appl. Phys. **35** (5B), L648 (1996).
17 A. D. McConnell, S. Uma, and K. E. Goodson, Journal of Microelectromechanical Systems **10** (3), 360 (2001).
18 E. Bozorg-Grayeli, J. P. Reifenberg, M. A. Panzer, J. A. Rowlette, and K. E. Goodson, IEEE electron device letters **32** (9), 1281 (2011).
19 J. Kang, W. Cao, X. Xie, D. Sarkar, W. Liu, and K. Banerjee, presented at the Micro-and Nanotechnology Sensors, Systems, and Applications VI, 2014 (unpublished).
20 H. Jin, C. Guo, X. Liu, J. Liu, A. Vasileff, Y. Jiao, Y. Zheng, and S.-Z. Qiao, Chemical reviews **118** (13), 6337 (2018).
21 A. Jeżowski, P. Stachowiak, T. Plackowski, T. Suski, S. Krukowski, M. Boćkowski, I. Grzegory, B. Danilchenko, and T. Paszkiewicz, Physica Status Solidi **240** (2), 447 (2003).
22 C. Mion, J. Muth, E. Preble, and D. Hanser, Appl. Phys. Lett. **89** (9), 092123 (2006).

23   E. Sichel, R. Miller, M. Abrahams, and C. Buiocchi, Phys. Rev. B **13** (10), 4607 (1976).

24   G. A. Slack, R. A. Tanzilli, R. Pohl, and J. Vandersande, J. Phys. Chem. Solids **48** (7), 641 (1987).

25   R. Rounds, B. Sarkar, D. Alden, Q. Guo, A. Klump, C. Hartmann, T. Nagashima, R. Kirste, A. Franke, M. Bickermann, Y. Kumagai, Z. Sitar, and R. Collazo, J. Appl. Phys. **123** (18), 185107 (2018).

26   See https://www.nobelprize.org/prizes/physics/2014/press-release/ for more information.

27   A. Sood, J. Cho, K. D. Hobart, T. I. Feygelson, B. B. Pate, M. Asheghi, D. G. Cahill, and K. E. Goodson, J. of Appl. Phys. **119** (17), 175103 (2016).

28   A. Sood, F. Xiong, S. Chen, H. Wang, D. Selli, J. Zhang, C. J. McClellan, J. Sun, D. Donadio, and Y. Cui, Nature communications **9** (1), 1 (2018).

29   E. Yalon, C. J. McClellan, K. K. Smithe, M. Muñoz Rojo, R. L. Xu, S. V. Suryavanshi, A. J. Gabourie, C. M. Neumann, F. Xiong, and A. B. Farimani, Nano Letters **17** (6), 3429 (2017).

30   T. Kodama, M. Ohnishi, W. Park, T. Shiga, J. Park, T. Shimada, H. Shinohara, J. Shiomi, and K. E. Goodson, Nature materials **16** (9), 892 (2017).

31   Z. Li, M.-H. Bae, and E. Pop, Applied Physics Letters **105** (2), 023107 (2014).

32   E. Yalon, O. B. Aslan, K. K. Smithe, C. J. McClellan, S. V. Suryavanshi, F. Xiong, A. Sood, C. M. Neumann, X. Xu, K. E. Goodson, T. F. Heinz, and E. Pop, ACS Appl. Mater. Interfaces **9** (49), 43013 (2017).

33   E. Yalon, C. McClellan, K. Smithe, Y. Shin, R. Xu, and E. Pop, IEEE Device Research Conference (DRC) (2016).

34   D. Tuschel, Spectroscopy **31** (12), 8 (2016).

35   M. H. Cho, J. Ju, S. J. Kim, and H. Jang, Wear **260** (7), 855 (2006).

36   H. Petroski, *The pencil: A history of design and circumstance*. (Alfred a Knopf Incorporated, 1992).

37   K. Novoselov, D. Jiang, F. Schedin, T. Booth, V. Khotkevich, S. Morozov, and A. Geim, Proceedings of the National Academy of Sciences of the United States of America **102** (30), 10451 (2005).

38   S. Bae, H. Kim, Y. Lee, X. Xu, J.-S. Park, Y. Zheng, J. Balakrishnan, T. Lei, H. R. Kim, and Y. I. Song, Nature nanotechnology **5** (8), 574 (2010).

39   K. K. H. Smithe, C. D. English, S. V. Suryavanshi, and E. Pop, arXiv preprint arXiv:1608.00987 (2016).

40   A. C. Neto and K. Novoselov, Reports on Progress in Physics **74** (8), 082501 (2011).

41   E. Pop, V. Varshney, and A. K. Roy, MRS Bull. **37** (12), 1273 (2012).

42   A. Sood, F. Xiong, S. Chen, R. Cheaito, F. Lian, M. Asheghi, Y. Cui, D. Donadio, K. E. Goodson, and E. Pop, Nano Letters **19** (4), 2434 (2019).

43   C. Chiritescu, D. G. Cahill, N. Nguyen, D. Johnson, A. Bodapati, P. Keblinski, and P. Zschack, Science **315** (5810), 351 (2007).

44   S. Vaziri, E. Yalon, M. Muñoz Rojo, S. V. Suryavanshi, H. Zhang, C. J. McClellan, C. S. Bailey, K. K. H. Smithe, A. J. Gabourie, V. Chen, S. Deshmukh, L. Bendersky, A. V. Davydov, and E. Pop, Science Advances **5** (8), eaax1325 (2019).

45 J.-Y. Kim, S.-M. Choi, W.-S. Seo, and W.-S. Cho, Bulletin of the Korean Chemical Society **31** (11), 3225 (2010).
46 C. Jeong, S. Datta, and M. Lundstrom, J. Appl. Phys. **109** (7), 073718 (2011).
47 J. M. Ziman, *Electrons and Phonons: The Theory of Transport Phenomena in Solids*. (Oxford University Press, Oxford, 2001), p.568.
48 C. Yuan, W. M. Waller, and M. Kuball, Review of Scientific Instruments **90** (11), 114903 (2019).
49 Y. Xu, Z. Li, and W. Duan, Small **10** (11), 2182 (2014).
50 J.-U. Lee, D. Yoon, H. Kim, S. W. Lee, and H. Cheong, Physical Review B **83** (8), 081419 (2011).
51 W. Lee, K. D. Kihm, H. G. Kim, S. Shin, C. Lee, J. S. Park, S. Cheon, O. M. Kwon, G. Lim, and W. Lee, Nano Letters **17** (4), 2361 (2017).
52 S. Chen, Q. Wu, C. Mishra, J. Kang, H. Zhang, K. Cho, W. Cai, A. A. Balandin, and R. S. Ruoff, Nature Materials **11** (3), 203 (2012).
53 J. H. Seol, I. Jo, A. L. Moore, L. Lindsay, Z. H. Aitken, M. T. Pettes, X. Li, Z. Yao, R. Huang, and D. Broido, Science **328** (5975), 213 (2010).
54 M. M. Sadeghi, I. Jo, and L. Shi, Proc. Natl. Acad. Sci. USA **110** (41), 16321 (2013).
55 M. Rahman, M. Shahzadeh, and S. Pisana, Journal of Applied Physics **126** (20), 205103 (2019).
56 W. Y. Jang, Z. Chen, W. Z. Bao, C. N. Lau, and C. Dames, Nano Lett. **10** (10), 3909 (2010).
57 A. D. Liao, J. Z. Wu, X. Wang, K. Tahy, D. Jena, H. Dai, and E. Pop, Phys. Rev. Lett. **106** (25), 256801 (2011).
58 M.-H. Bae, Z. Li, Z. Aksamija, P. N. Martin, F. Xiong, Z.-Y. Ong, I. Knezevic, and E. Pop, Nat. Commun. **4**, 1734 (2013).
59 Z. Li, M.-H. Bae, and E. Pop, Appl. Phys. Lett. **105** (2), 023107 (2014).
60 E. K. Sichel, R. E. Miller, M. S. Abrahams, and C. J. Buiocchi, Phys. Rev. B **13** (10), 4607 (1976).
61 C. Yuan, J. Li, L. Lindsay, D. Cherns, J. W. Pomeroy, S. Liu, J. H. Edgar, and M. Kuball, Communications Physics **2** (1), 43 (2019).
62 P. Jiang, X. Qian, R. Yang, and L. Lindsay, Physical Review Materials **2** (6), 064005 (2018).
63 I. Jo, M. T. Pettes, J. Kim, K. Watanabe, T. Taniguchi, Z. Yao, and L. Shi, Nano Lett. **13** (2), 550 (2013).
64 H. Zhou, J. Zhu, Z. Liu, Z. Yan, X. Fan, J. Lin, G. Wang, Q. Yan, T. Yu, P. M. Ajayan, and J. M. Tour, Nano Res. **7** (8), 1232 (2014).
65 C. Wang, J. Guo, L. Dong, A. Aiyiti, X. Xu, and B. Li, Scientific reports **6** (2016).
66 J. Liu, G.-M. Choi, and D. G. Cahill, J. Appl. Phys. **116** (23), 233107 (2014).
67 G. Zhu, J. Liu, Q. Zheng, R. Zhang, D. Li, D. Banerjee, and D. G. Cahill, Nature Communications **7** (1), 13211 (2016).
68 P. Jiang, X. Qian, X. Gu, and R. Yang, Advanced Materials **29** (36), 1701068 (2017).

69   A. Pisoni, J. Jacimovic, O. S. Barišić, A. Walter, B. Náfrádi, P. Bugnon, A. Magrez, H. Berger, Z. Revay, and L. Forró, The Journal of Physical Chemistry C **119** (8), 3918 (2015).

70   R. S. Yan, J. R. Simpson, S. Bertolazzi, J. Brivio, M. Watson, X. F. Wu, A. Kis, T. F. Luo, A. R. H. Walker, and H. G. Xing, ACS Nano **8** (1), 986 (2014).

71   X. Zhang, D. Sun, Y. Li, G.-H. Lee, X. Cui, D. Chenet, Y. You, T. F. Heinz, and J. C. Hone, ACS Applied Materials & Interfaces **7** (46), 25923 (2015).

72   S. Sahoo, A. P. S. Gaur, M. Ahmadi, M. J. F. Guinel, and R. S. Katiyar, J. Phys. Chem. C **117** (17), 9042 (2013).

73   I. Jo, M. T. Pettes, E. Ou, W. Wu, and L. Shi, Appl. Phys. Lett. **104** (20), 201902 (2014).

74   J. J. Bae, H. Y. Jeong, G. H. Han, J. Kim, H. Kim, M. S. Kim, B. H. Moon, S. C. Lim, and Y. H. Lee, Nanoscale **9** (7), 2541 (2017).

75   M. Yarali, X. Wu, T. Gupta, D. Ghoshal, L. Xie, Z. Zhu, H. Brahmi, J. Bao, S. Chen, T. Luo, N. Koratkar, and A. Mavrokefalos, Advanced Functional Materials **27** (46), 1704357 (2017).

76   A. Aiyiti, S. Hu, C. Wang, Q. Xi, Z. Cheng, M. Xia, Y. Ma, J. Wu, J. Guo, Q. Wang, J. Zhou, J. Chen, X. Xu, and B. Li, Nanoscale **10** (6), 2727 (2018).

77   A. Aiyiti, X. Bai, J. Wu, X. Xu, and B. Li, Science Bulletin **63** (7), 452 (2018).

78   N. Peimyoo, J. Shang, W. Yang, Y. Wang, C. Cong, and T. Yu, Nano Res. **8** (4), 1210 (2015).

79   A. Pisoni, J. Jacimovic, R. Gaál, B. Náfrádi, H. Berger, Z. Revay, and L. Forró, Scripta Materialia **114**, 48 (2016).

80   N. Morell, S. Tepsic, A. Reserbat-Plantey, A. Cepellotti, M. Manca, I. Epstein, A. Isacsson, X. Marie, F. Mauri, and A. Bachtold, Nano Letters **19** (5), 3143 (2019).

81   M. Yarali, H. Brahmi, Z. Yan, X. Li, L. Xie, S. Chen, S. Kumar, M. Yoon, K. Xiao, and A. Mavrokefalos, ACS applied materials & interfaces **10** (5), 4921 (2018).

82   H. Zobeiri, R. Wang, T. Wang, H. Lin, C. Deng, and X. Wang, International Journal of Heat and Mass Transfer **133**, 1074 (2019).

83   R. Wang, T. Wang, H. Zobeiri, P. Yuan, C. Deng, Y. Yue, S. Xu, and X. Wang, Nanoscale **10** (48), 23087 (2018).

84   A. Mavrokefalos, N. T. Nguyen, M. T. Pettes, D. C. Johnson, and L. Shi, Applied Physics Letters **91** (17), 171912 (2007).

85   Y. Liu, J. Liu, X. Tan, Y. Li, R. Liu, Y. Lin, and C. Nan, Journal of the American Ceramic Society (2017).

86   M. J. Mleczko, R. Xu, K. Okabe, H.-H. Kuo, I. R. Fisher, H.-S. P. Wong, Y. Nishi, and E. Pop, ACS Nano **10**, 7507 (2016).

87   M. K. Jana, A. Singh, D. J. Late, C. R. Rajamathi, K. Biswas, C. Felser, U. V. Waghmare, and C. Rao, Journal of Physics: Condensed Matter **27** (28), 285401 (2015).

88   Y. Zhou, H. Jang, J. M. Woods, Y. Xie, P. Kumaravadivel, G. A. Pan, J. Liu, Y. Liu, D. G. Cahill, and J. J. Cha, Advanced Functional Materials **27** (8) (2017).

89   X. Qian, P. Jiang, P. Yu, X. Gu, Z. Liu, and R. Yang, Applied Physics Letters **112** (24), 241901 (2018).

90	H. Jang, C. R. Ryder, J. D. Wood, M. C. Hersam, and D. G. Cahill, Advanced Materials **29** (35) (2017).
91	S. Lee, F. Yang, J. Suh, S. Yang, Y. Lee, G. Li, H. Sung Choe, A. Suslu, Y. Chen, C. Ko, J. Park, K. Liu, J. Li, K. Hippalgaonkar, J. J. Urban, S. Tongay, and J. Wu, Nat. Commun. **6**, 8573 (2015).
92	Z. Luo, J. Maassen, Y. Deng, Y. Du, R. P. Garrelts, M. S. Lundstrom, D. Y. Peide, and X. Xu, Nat. Commun. **6**, 8572 (2015).
93	H. Jang, J. D. Wood, C. R. Ryder, M. C. Hersam, and D. G. Cahill, Adv. Mater. **27** (48), 8017 (2015).
94	L. Su and Y. Zhang, Appl. Phys. Lett. **107** (7), 071905 (2015).
95	J. Zhu, H. Park, J. Y. Chen, X. Gu, H. Zhang, S. Karthikeyan, N. Wendel, S. A. Campbell, M. Dawber, and X. Du, Advanced Electronic Materials **2** (5) (2016).
96	B. Sun, X. Gu, Q. Zeng, X. Huang, Y. Yan, Z. Liu, R. Yang, and Y. K. Koh, Advanced Materials **29** (3) (2017).
97	B. Smith, B. Vermeersch, J. Carrete, E. Ou, J. Kim, N. Mingo, D. Akinwande, and L. Shi, Advanced Materials **29** (5) (2017).
98	A. Islam, A. van den Akker, and P. X. L. Feng, Nano Letters **18** (12), 7683 (2018).
99	S. Hu, J. Xiang, M. Lv, J. Zhang, H. Zhao, C. Li, G. Chen, W. Wang, and P. Sun, Physical Review B **97** (4), 045209 (2018).
100	Y. Wang, G. Xu, Z. Hou, B. Yang, X. Zhang, E. Liu, X. Xi, Z. Liu, Z. Zeng, W. Wang, and G. Wu, Appl. Phys. Lett. **108** (9), 092102 (2016).
101	H. Liu, J. Liu, R. Jing, and C. You, MRS Communications **9** (4), 1311 (2019).
102	S. G. Jeon, H. Shin, Y. H. Jaung, J. Ahn, and J. Y. Song, Nanoscale **10** (13), 5985 (2018).
103	Y. Zhao, G. Zhang, M. H. Nai, G. Ding, D. Li, Y. Liu, K. Hippalgaonkar, C. T. Lim, D. Chi, B. Li, J. Wu, and J. T. L. Thong, Advanced Materials **30** (50), 1804928 (2018).
104	Z. Li, Y. Liu, L. Lindsay, Y. Xu, W. Duan, and E. Pop, unpublished (2016).
105	Q. Fu, J. K. Yang, Y. F. Chen, D. Y. Li, and D. Y. Xu, Appl. Phys. Lett. **106** (3), 031905 (2015).
106	H. Zhang, X. Chen, Y.-D. Jho, and A. J. Minnich, Nano Lett. **16** (3), 1643 (2016).
107	A. Taube, J. Judek, A. Łapińska, and M. Zdrojek, ACS Applied Materials & Interfaces **7** (9), 5061 (2015).
108	A. Simpson and A. D. Stuckes, J. Phys. C: Solid St. Phys. **4** (13), 1710 (1971).
109	C. Muratore, V. Varshney, J. J. Gengler, J. J. Hu, J. E. Bultman, T. M. Smith, P. J. Shamberger, B. Qiu, X. Ruan, A. K. Roy, and A. A. Voevodin, Appl. Phys. Lett. **102** (8), 081604 (2013).
110	C. Monachon, L. Weber, and C. Dames, Annual Review of Materials Research **46**, 433 (2016).
111	E. T. Swartz and R. O. Pohl, Reviews of modern physics **61** (3), 605 (1989).
112	P. L. Kapitza, Journal of Physics USSR **4** (1941).
113	A. Giri and P. E. Hopkins, Advanced Functional Materials **n/a** (n/a), 1903857.
114	M.-H. Bae, S. Islam, V. E. Dorgan, and E. Pop, ACS Nano **5** (10), 7936 (2011).

115 S. Islam, Z. Li, V. E. Dorgan, M.-H. Bae, and E. Pop, IEEE Electron Device Lett. **34** (2), 166 (2013).

116 F. Lian, J. P. Llinas, Z. Li, D. Estrada, and E. Pop, Appl. Phys. Lett. **108** (10), 103101 (2016).

117 Y. K. Koh, M.-H. Bae, D. G. Cahill, and E. Pop, Nano Lett. **10** (11), 4363 (2010).

118 Z. Chen, W. Jang, W. Bao, C. Lau, and C. Dames, Appl. Phys. Lett. **95** (16), 161910 (2009).

119 P. E. Hopkins, M. Baraket, E. V. Barnat, T. E. Beechem, S. P. Kearney, J. C. Duda, J. T. Robinson, and S. G. Walton, Nano Lett. **12** (2), 590 (2012).

120 A. J. Schmidt, K. C. Collins, A. J. Minnich, and G. Chen, J. Appl. Phys. **107** (10), 104907 (2010).

121 J. P. Feser and D. G. Cahill, Review of Scientific Instruments **83** (10), 104901 (2012).

122 K. F. Mak, C. H. Lui, and T. F. Heinz, Appl. Phys. Lett. **97** (22), 221904 (2010).

123 M. Freitag, M. Steiner, Y. Martin, V. Perebeinos, Z. Chen, J. C. Tsang, and P. Avouris, Nano Letters **9** (5), 1883 (2009).

124 C.-C. Chen, Z. Li, L. Shi, and S. B. Cronin, Applied Physics Letters **104** (8), 081908 (2014).

125 B. Liu, F. Meng, C. D. Reddy, J. A. Baimova, N. Srikanth, S. V. Dmitriev, and K. Zhou, Rsc Advances **5** (37), 29193 (2015).

126 Z. Ding, Q.-X. Pei, J.-W. Jiang, W. Huang, and Y.-W. Zhang, Carbon **96**, 888 (2016).

127 J. Judek, A. P. Gertych, M. Świniarski, A. Łapińska, A. Dużyńska, and M. Zdrojek, Scientific reports **5** (2015).

128 E. Pop, Nano Res. **3** (3), 147 (2010).

129 P. E. Hopkins, J. C. Duda, and P. M. Norris, Journal of Heat Transfer **133** (6), 062401 (2011).

130 W.-P. Hsieh, A. S. Lyons, E. Pop, P. Keblinski, and D. G. Cahill, Physical Review B **84** (18), 184107 (2011).

131 V. N. Popov, Phys. Rev. B **66** (15), 153408 (2002).

132 A. Behnam, A. S. Lyons, M.-H. Bae, E. K. Chow, S. Islam, C. M. Neumann, and E. Pop, Nano Lett. **12** (9), 4424 (2012).

133 J. Yu, G. Liu, A. V. Sumant, V. Goyal, and A. A. Balandin, Nano Letters **12** (3), 1603 (2012).

134 M. M. Shulaker, J. Van Rethy, T. F. Wu, L. S. Liyanage, H. Wei, Z. Y. Li, E. Pop, G. Gielen, H. S. P. Wong, and S. Mitra, ACS Nano **8** (4), 3434 (2014).

135 G. J. Snyder and E. S. Toberer, Nature Materials **7** (2), 105 (2008).

136 J. Pu, K. Kanahashi, N. T. Cuong, C.-H. Chen, L.-J. Li, S. Okada, H. Ohta, and T. Takenobu, Physical Review B **94** (1), 014312 (2016).

137 M. Buscema, M. Barkelid, V. Zwiller, H. S. van der Zant, G. A. Steele, and A. Castellanos-Gomez, Nano Lett. **13** (2), 358 (2013).

138 S. K. Srivastava and B. N. Avasthi, Synth. Met **11** (4), 193 (1985).

139 R. Mansfield and S. Salam, Proceedings of the Physical Society. Section B **66** (5), 377 (1953).

140   K. Hippalgaonkar, Y. Wang, Y. Ye, H. Zhu, Y. Wang, J. Moore, and X. Zhang, arXiv preprint arXiv:1505.06779 (2015).

141   J. Wu, H. Schmidt, K. K. Amara, X. Xu, G. Eda, and B. Özyilmaz, Nano letters **14** (5), 2730 (2014).

142   Y. Zhang, H. Li, L. Wang, H. Wang, X. Xie, S.-L. Zhang, R. Liu, and Z.-J. Qiu, Scientific reports **5** (2015).

143   K. Hippalgaonkar, Y. Wang, Y. Ye, D. Y. Qiu, H. Zhu, Y. Wang, J. Moore, S. G. Louie, and X. Zhang, Physical Review B **95** (11), 115407 (2017).

144   S. G. Thakurta and A. Dutta, Journal of Physics and Chemistry of Solids **44** (5), 407 (1983).

145   T. Wang, C. Liu, J. Xu, Z. Zhu, E. Liu, Y. Hu, C. Li, and F. Jiang, Nanotechnology **27** (28), 285703 (2016).

146   G. Solanki, D. Gujarathi, M. Deshpande, D. Lakshminarayana, and M. Agarwal, Crystal Research and Technology **43** (2), 179 (2008).

147   J. Patel, M. Parmar, M. Deshpande, G. Solanki, and M. Agarwal, Indian journal of Pure and Applied Physics **43** (7), 527 (2005).

148   G. Yakovleva, A. Romanenko, A. Berdinsky, A. Y. Ledneva, V. Kuznetsov, M. Han, S. Kim, and V. E. Fedorov, presented at the Information and Communication Technology, Electronics and Microelectronics (MIPRO), 2016 39th International Convention on, 2016 (unpublished).

149   Z. Huang, T. Wu, S. Kong, Q.-L. Meng, W. Zhuang, P. Jiang, and X. Bao, Journal of Materials Chemistry A **4** (26), 10159 (2016).

150   L. Brixner, Journal of Inorganic and Nuclear Chemistry **24** (3), 257 (1962).

151   J. Champion, British Journal of Applied Physics **16** (7), 1035 (1965).

152   E. Revolinsky and D. Beerntsen, Journal of Applied Physics **35** (7), 2086 (1964).

153   S. Gawale, R. Mane, S. Mane, R. Kharade, S. Patil, and P. Bhosale, Archives of Physics Research **1** (3), 72 (2010).

154   L. Brixner and G. Teufer, Inorganic Chemistry **2** (5), 992 (1963).

155   L. Ruan, H. Zhao, D. Li, S. Jin, S. Li, L. Gu, and J. Liang, Journal of Electronic Materials **45** (6), 2926 (2016).

156   D. Suri and R. Patel, Applied Physics Letters **110** (23), 233108 (2017).

157   M. Yoshida, T. Iizuka, Y. Saito, M. Onga, R. Suzuki, Y. Zhang, Y. Iwasa, and S. Shimizu, Nano letters **16** (3), 2061 (2016).

158   A. Conan, A. Bonnet, A. Amrouche, and M. Spiesser, Journal de Physique **45** (3), 459 (1984).

159   D. Shi, G. Wang, C. Li, X. Shen, and Q. Nie, Vacuum **138**, 101 (2017).

160   M. K. Jana, A. Singh, A. Sampath, C. Rao, and U. V. Waghmare, Zeitschrift für anorganische und allgemeine Chemie **642** (23), 1386 (2016).

161   L.-D. Zhao, S.-H. Lo, Y. Zhang, H. Sun, G. Tan, C. Uher, C. Wolverton, V. P. Dravid, and M. G. Kanatzidis, Nature **508** (7496), 373 (2014).

162   H.-Q. Leng, M. Zhou, J. Zhao, Y.-M. Han, and L.-F. Li, Rsc Advances **6** (11), 9112 (2016).

163   L.-D. Zhao, C. Chang, G. Tan, and M. G. Kanatzidis, Energy & Environmental Science **9** (10), 3044 (2016).

164   N. K. Singh, S. Bathula, B. Gahtori, K. Tyagi, D. Haranath, and A. Dhar, Journal of Alloys and Compounds **668**, 152 (2016).

165 Y. Fu, J. Xu, G.-Q. Liu, J. Yang, X. Tan, Z. Liu, H. Qin, H. Shao, H. Jiang, and B. Liang, Journal of Materials Chemistry C **4** (6), 1201 (2016).

166 M. Gharsallah, F. Serrano-Sánchez, N. Nemes, F. Mompeán, J. Martínez, M. Fernández-Díaz, F. Elhalouani, and J. Alonso, Scientific reports **6**, srep26774 (2016).

167 M.-J. Lee, J.-H. Ahn, J. H. Sung, H. Heo, S. G. Jeon, W. Lee, J. Y. Song, K.-H. Hong, B. Choi, and S.-H. Lee, Nature communications **7** (2016).

168 E. Flores, J. R. Ares, A. Castellanos-Gomez, M. Barawi, I. J. Ferrer, and C. Sánchez, Applied Physics Letters **106** (2), 022102 (2015).

169 Y. Saito, T. Iizuka, T. Koretsune, R. Arita, S. Shimizu, and Y. Iwasa, Nano Letters (2016).

170 T. Low, M. Engel, M. Steiner, and P. Avouris, Phys. Rev. B **90** (8), 081408 (2014).

171 S. J. Choi, B.-K. Kim, T.-H. Lee, Y. H. Kim, Z. Li, E. Pop, J.-J. Kim, J. H. Song, and M.-H. Bae, Nano letters (2016).

172 D. Warschauer, Journal of Applied Physics **34** (7), 1853 (1963).

173 P. Bridgman, presented at the Proceedings of the American Academy of Arts and Sciences, 1921 (unpublished).

174 Y. M. Zuev, W. Chang, and P. Kim, Phys. Rev. Lett. **102** (9), 096807 (2009).

175 X. Li, J. Yin, J. Zhou, Q. Wang, and W. Guo, Appl. Phys. Lett. **100** (18), 183108 (2012).

176 K. Kobayashi, K. Sugihara, H. Oshima, and T. Tsuzuku, Journal of the Physical Society of Japan **62** (12), 4393 (1993).

177 C. Wan, X. Gu, F. Dang, T. Itoh, Y. Wang, H. Sasaki, M. Kondo, K. Koga, K. Yabuki, and G. J. Snyder, Nature materials **14** (6), 622 (2015).

178 C. Wan, Y. Wang, N. Wang, W. Norimatsu, M. Kusunoki, and K. Koumoto, Journal of electronic materials **40** (5), 1271 (2011).

179 M. Kayyalha, J. Maassen, M. Lundstrom, L. Shi, and Y. P. Chen, Journal of Applied Physics **120** (13), 134305 (2016).

180 H. Zou, D. M. Rowe, and G. Min, Journal of Crystal Growth **222** (1), 82 (2001).

181 J. Tao, N. W. Cheung, and C. M. Hu, IEEE Electron Device Lett. **14** (5), 249 (1993).

182 R. G. Filippi, P. C. Wang, A. Brendler, P. S. McLaughlin, J. Poulin, B. Redder, J. R. Lloyd, and J. J. Demarest, 2009 IEEE Int. Reliab. Phys. Symp. Proc. **1**, 444 (2009).

183 X. Y. Chen, D. H. Seo, S. Seo, H. Chung, and H. S. P. Wong, IEEE Electron Device Lett. **33** (11), 1604 (2012).

184 K. S. Novoselov, A. K. Geim, S. V. Morozov, D. Jiang, Y. Zhang, S. V. Dubonos, I. V. Grigorieva, and A. A. Firsov, Science **306** (5696), 666 (2004).

185 M. Chhowalla, H. S. Shin, G. Eda, L.-J. Li, K. P. Loh, and H. Zhang, Nature Chemistry **5** (4), 263 (2013).

186 G. Fiori, F. Bonaccorso, G. Iannaccone, T. Palacios, D. Neumaier, A. Seabaugh, S. K. Banerjee, and L. Colombo, Nature Nanotechnology **9** (10), 768 (2014).

187 B. E. Brown, Acta Crystallographica **20**, 268 (1966).

188 B. E. Brown, Acta Crystallogr. **20**, 268 (1966).

189 W. G. Dawson and D. W. Bullett, J. Phys. C: Solid State Phys. **20** (36), 6159 (1987).
190 A. Mar, S. Jobic, and J. A. Ibers, J. Am. Chem. Soc. **114** (23), 8963 (1992).
191 D. H. Keum, S. Cho, J. H. Kim, D.-H. Choe, H.-J. Sung, M. Kan, H. Kang, J.-Y. Hwang, S. W. Kim, H. Yang, K. J. Chang, and Y. H. Lee, Nat. Phys. **11** (6), 482 (2015).
192 K.-A. N. Duerloo, Y. Li, and E. J. Reed, Nat. Commun. **5**, 4214 (2014).
193 J. A. Wilson and A. D. Yoffe, Adv. Phys. **18** (73), 193 (1969).
194 L. H. Brixner, J. Inorg. Nucl. Chem. **24**, 257 (1962).
195 M. N. Ali, J. Xiong, S. Flynn, J. Tao, Q. D. Gibson, L. M. Schoop, T. Liang, N. Haldolaarachchige, M. Hirschberger, N. P. Ong, and R. J. Cava, Nature **514** (7521), 205 (2014).
196 I. Pletikosic, M. N. Ali, A. V. Fedorov, R. J. Cava, and T. Valla, Phys. Rev. Lett. **113** (21), 216601 (2014).
197 H. Y. Lv, W. J. Lu, D. F. Shao, Y. Liu, S. G. Tan, and Y. P. Sun, Europhys. Lett. **110** (3), 37004 (2015).
198 Y. Liu, P. Stradins, and S.-H. Wei, Sci. Adv. **2** (4), 1600069 (2016).
199 C. McClellan, M. J. Mleczko, K. H. Smithe, Y. Nishi, and E. Pop, in *74th Device Research Conference* (IEEE, Newark, DW, 2016), p. (in press).
200 C.-H. Lee, E. Cruz-Silva, L. Calderin, M. A. T. Nguyen, M. J. Hollander, B. Bersch, T. E. Mallouk, and J. A. Robinson, Sci. Rep. **5** (2015).
201 Y. C. Jiang, J. Gao, and L. Wang, Sci. Rep. **6**, 19624 (2016).
202 M. K. Jana, A. Singh, D. J. Late, C. R. Rajamathi, K. Biswas, C. Felser, U. V. Waghmare, and C. N. R. Rao, J. Phys. Condens. Matter **27** (28), 285401 (2015).
203 L. Wang, I. Gutierrez-Lezama, C. Barreteau, N. Ubrig, E. Giannini, and A. F. Morpurgo, Nat. Commun. **6**, 7 (2015).
204 B. Chen, H. Sahin, A. Suslu, L. Ding, M. I. Bertoni, F. M. Peeters, and S. Tongay, ACS Nano **9** (5), 5326 (2015).
205 J. D. Wood, S. A. Wells, D. Jariwala, K.-S. Chen, E. Cho, V. K. Sangwan, X. Liu, L. J. Lauhon, T. J. Marks, and M. C. Hersam, Nano Lett. **14** (12), 6964 (2014).
206 J.-S. Kim, Y. Liu, W. Zhu, S. Kim, D. Wu, L. Tao, A. Dodabalapur, K. Lai, and D. Akinwande, Sci. Rep. **5**, 8989 (2015).
207 M. K. Bahl, R. L. Watson, and K. J. Irgolic, J. Chem. Phys. **66** (12), 5526 (1977).
208 T. S. Sun, S. P. Buchner, and N. E. Byer, J. Vac. Sci. Technol. **17** (5), 1067 (1980).
209 H. Li, G. Lu, Y. L. Wang, Z. Y. Yin, C. X. Cong, Q. Y. He, L. Wang, F. Ding, T. Yu, and H. Zhang, Small **9** (11), 1974 (2013).
210 M. Yamamoto, S. Dutta, S. Aikawa, S. Nakaharai, K. Wakabayashi, M. S. Fuhrer, K. Ueno, and K. Tsukagoshi, Nano Lett. **15** (3), 2067 (2015).
211 G. E. McGuire, Schweitz.Gk, and T. A. Carlson, Inorg. Chem. **12** (10), 2450 (1973).
212 L. Salvati, L. E. Makovsky, J. M. Stencel, F. R. Brown, and D. M. Hercules, J. Phys. Chem. **85** (24), 3700 (1981).
213 G. Salitra, G. Hodes, E. Klein, and R. Tenne, Thin Solid Films **245** (1-2), 180 (1994).

214   O. Lang, R. Schlaf, Y. Tomm, C. Pettenkofer, and W. Jaegermann, J. Appl. Phys. **75** (12), 7805 (1994).

215   M. K. Jana, A. Singh, D. J. Late, C. R. Rajamathi, K. Biswas, C. Felser, U. V. Waghmare, and C. N. R. Rao, Journal of Physics-Condensed Matter **27** (28), 285401 (2015).

216   M. Chhowalla, H. S. Shin, G. Eda, L.-J. Li, K. P. Loh, and H. Zhang, Nat. Chem. **5** (4), 263 (2013).

217   S. Kabashima, J. Phys. Soc. Jpn. **21** (5), 945 (1966).

218   J. A. A. Crossley, C. J. Sofield, and S. Myhra, Surf. Sci. **380**, 568 (1997).

219   Z. W. Zhu, X. Lin, J. Liu, B. Fauque, Q. Tao, C. L. Yang, Y. G. Shi, and K. Behnia, Phys. Rev. Lett. **114** (17), 176601 (2015).

220   L. R. Thoutam, Y. L. Wang, Z. L. Xiao, S. Das, A. Luican-Mayer, R. Divan, G. W. Crabtree, and W. K. Kwok, Phys. Rev. Lett. **115** (4), 046602 (2015).

221   Y. Yu, F. Yang, X. F. Lu, Y. J. Yan, Y.-H. Cho, L. Ma, X. Niu, S. Kim, Y.-W. Son, D. Feng, S. Li, S.-W. Cheong, X. H. Chen, and Y. Zhang, Nat. Nanotechnol. **10** (3), 270 (2015).

222   M. J. Hollander, Y. Liu, W.-J. Lu, L.-J. Li, Y.-P. Sun, J. A. Robinson, and S. Datta, Nano Lett. **15** (3), 1861 (2015).

223   C. D. English, G. Shine, V. E. Dorgan, K. C. Saraswat, and E. Pop, Nano Lett. **16** (9), 3824 (2016).

224   A. Allain, J. Kang, K. Banerjee, and A. Kis, Nat. Mater. **14** (12), 1195 (2015).

225   Y. Sui and J. Appenzeller, Nano Lett. **9** (8), 2973 (2009).

226   S. Das and J. Appenzeller, Nano Lett. **13** (7), 3396 (2013).

227   W. P. Dyke, J. P. Barbour, E. E. Martin, and J. K. Trolan, Phys. Rev. **99** (4), 1192 (1955).

228   J. Tao, K. K. Young, C. A. Pico, N. W. Cheung, and C. M. Hu, IEEE Electron Device Lett. **12** (12), 646 (1991).

229   I. Ames, F. M. Dheurle, and Horstman.Re, IBM J. Res. Dev. **14** (4), 461 (1970).

230   A. Behnam, A. S. Lyons, M.-H. Bae, E. K. Chow, S. Islam, C. M. Neumann, and E. Pop, Nano Lett. **12** (9), 4424 (2012).

231   A. T. Neal, Y. C. Du, H. Liu, and P. D. D. Ye, ACS Nano **8** (9), 9137 (2014).

232   V. E. Dorgan, M. H. Bae, and E. Pop, Appl. Phys. Lett. **97** (8), 082112 (2010).

233   I. Stark, M. Stordeur, and F. Syrowatka, Thin Solid Films **226** (1), 185 (1993).

234   A. Cappella, J. L. Battaglia, V. Schick, A. Kusiak, A. Lamperti, C. Wiemer, and B. Hay, Adv. Eng. Mater. **15** (11), 1046 (2013).

235   G. Liu, H. Y. Sun, J. Zhou, Q. F. Li, and X.-G. Wan, New J. Phys. **18** (3), 033017 (2016).

236   Y. K. Koh, M. H. Bae, D. G. Cahill, and E. Pop, Nano Lett. **10** (11), 4363 (2010).

237   A. Behnam, F. Xiong, A. Cappelli, N. C. Wang, E. A. Carrion, S. Hong, Y. Dai, A. S. Lyons, E. K. Chow, E. Piccinini, C. Jacoboni, and E. Pop, Appl. Phys. Lett. **107** (12), 123508 (2015).

238   X. F. Qian, J. W. Liu, L. Fu, and J. Li, Science **346** (6215), 1344 (2014).

239   D. MacNeill, M. H. D. Stiehl, R. A. Guimaraes, J. Park , and D. C. Ralph, arXiv preprint, arXiv:1605.02712 (2016).

240 Z. Hu, K. Nomoto, W. Li, Z. Zhang, N. Tanen, Q. T. Thieu, K. Sasaki, A. Kuramata, T. Nakamura, D. Jena, and H. G. Xing, Appl. Phys. Lett. **113** (12), 122103 (2018).

241 J. Encomendero, R. Yan, A. Verma, S. Islam, V. Protasenko, S. Rouvimov, P. Fay, D. Jena, and H. G. Xing, Appl. Phys. Lett. **112** (10), 103101 (2018).

242 G. Li, B. Song, S. Ganguly, M. Zhu, R. Wang, X. Yan, J. Verma, V. Protasenko, H. Grace Xing, and D. Jena, Appl. Phys. Lett. **104** (19), 193506 (2014).

243 E. Pop, S. Sinha, and K. E. Goodson, Proc. of the IEEE **94** (8), 1587 (2006).

244 R. Gaska, A. Osinsky, J. Yang, and M. S. Shur, IEEE Elec. Dev. Lett. **19** (3), 89 (1998).

245 M. Kuball, S. Rajasingam, A. Sarua, M. Uren, T. Martin, B. Hughes, K. Hilton, and R. Balmer, Appl. Phys. Lett. **82** (1), 124 (2003).

246 H. Wang, M. Liserre, F. Blaabjerg, P. de Place Rimmen, J. B. Jacobsen, T. Kvisgaard, and J. Landkildehus, IEEE Journal of Emerging Selected Topics in Power Electronics **2** (1), 97 (2014).

247 G. Lang, B. Fehder, and W. Williams, IEEE Trans. on Electron Devices **17** (9), 787 (1970).

248 M. Feneberg, R. A. Leute, B. Neuschl, K. Thonke, and M. Bickermann, Phys. Rev. B **82** (7), 075208 (2010).

249 J. Li, K. Nam, M. Nakarmi, J. Lin, H. Jiang, P. Carrier, and S.-H. Wei, Appl. Phys. Lett. **83** (25), 5163 (2003).

250 W. Yim, E. Stofko, P. Zanzucchi, J. Pankove, M. Ettenberg, and S. Gilbert, J. Appl. Phys. **44** (1), 292 (1973).

251 H. Okumura, S. Suihkonen, J. Lemettinen, A. Uedono, Y. Zhang, D. Piedra, and T. Palacios, Japanese J. Appl. Phys. **57** (4S), 04FR11 (2018).

252 A. G. Baca, A. M. Armstrong, A. A. Allerman, E. A. Douglas, C. A. Sanchez, M. P. King, M. E. Coltrin, T. R. Fortune, and R. J. Kaplar, Appl. Phys. Lett. **109** (3), 033509 (2016).

253 M. Holland, Phys. Rev. **134** (2A), A471 (1964).

254 R. Carlson, G. Slack, and S. Silverman, J. of Appl. Phys. **36** (2), 505 (1965).

255 G. A. Slack, J. of Appl. Phys. **35** (12), 3460 (1964).

256 C. Dames, Science **361** (6402), 549 (2018).

257 S. Li, Q. Zheng, Y. Lv, X. Liu, X. Wang, P. Y. Huang, D. G. Cahill, and B. Lv, Science **361** (6402), 579 (2018).

258 A. M. Hofmeister, Phys. Chem. of Minerals **41** (5), 361 (2014).

259 D. G. Cahill, Rev. Sci. Instrum. **61** (2), 802 (1990).

260 S.-M. Lee and D. G. Cahill, J. of Appl. Phys. **81** (6), 2590 (1997).

261 I. Kudman and E. Steigmeier, Phys. Rev. **133** (6A), A1665 (1964).

262 Z. Guo, A. Verma, X. Wu, F. Sun, A. Hickman, T. Masui, A. Kuramata, M. Higashiwaki, D. Jena, and T. Luo, Appl. Phys. Lett. **106** (11), 111909 (2015).

263 See http://www.hexatechinc.com/aln-growth-process.html for more information about AlN grow process; accessed 7 December 2018.

264 B. E. Gaddy, Z. Bryan, I. Bryan, J. Xie, R. Dalmau, B. Moody, Y. Kumagai, T. Nagashima, Y. Kubota, T. Kinoshita, A. Koukitu, R. Kirste, Z. Sitar, R. Collazo, and D. L. Irving, Appl. Phys. Lett. **104** (20), 202106 (2014).

265 C. Dames, Annual Review of Heat Transfer **16** (16) (2013).

266 C. Dames and G. Chen, Rev. Sci. Instrum. **76** (12), 124902 (2005).
267 M. T. Barako, A. Sood, C. Zhang, J. Wang, T. Kodama, M. Asheghi, X. Zheng, P. V. Braun, and K. E. Goodson, Nano Letters **16** (4), 2754 (2016).
268 J. Zou, D. Kotchetkov, A. Balandin, D. Florescu, and F. H. Pollak, J. Appl. Phys. **92** (5), 2534 (2002).
269 D. G. Cahill, Rev. Sci. Instrum. **75** (12), 5119 (2004).
270 A. Sood, R. Cheaito, T. Bai, H. Kwon, Y. Wang, C. Li, L. Yates, T. Bougher, S. Graham, M. Asheghi, M. Goorsky, and K. E. Goodson, Nano Lett. **18**, 3466 (2018).
271 Y. Shen, J. Gaskins, X. Xie, B. M. Foley, R. Cheaito, P. E. Hopkins, and J. C. Campbell, Journal of Lightwave Technology **35** (19), 4242 (2017).
272 P. Kuo, G. Auner, and Z. Wu, Thin Solid Films **253** (1-2), 223 (1994).
273 C. Duquenne, M.-P. Besland, P. Tessier, E. Gautron, Y. Scudeller, and D. Averty, J. of Phys. D: Appl. Phys. **45** (1), 015301 (2011).
274 Y. Zhao, C. Zhu, S. Wang, J. Tian, D. Yang, C. Chen, H. Cheng, and P. Hing, J. Appl. Phys. **96** (8), 4563 (2004).
275 S. R. Choi, D. Kim, S.-H. Choa, S.-H. Lee, and J.-K. Kim, Int. J. Thermophys. **27** (3), 896 (2006).
276 A. Jacquot, B. Lenoir, A. Dauscher, P. Verardi, F. Craciun, M. Stölzer, M. Gartner, and M. Dinescu, Appl. Surf. Sci. **186** (1-4), 507 (2002).
277 Y. Bian, M. Liu, G. Ke, Y. Chen, J. DiBattista, E. Chan, and Y. Yang, Surf. Coat. Technol. **267**, 65 (2015).
278 J. T. Gaskins, P. E. Hopkins, D. R. Merrill, S. R. Bauers, E. Hadland, D. C. Johnson, D. Koh, J. H. Yum, S. Banerjee, and B. J. Nordell, ECS J. Solid State Sci. Technol. **6** (10), N189 (2017).
279 W. Liu and A. A. Balandin, J. Appl. Phys. **97** (7), 073710 (2005).
280 A. Sztein, J. Haberstroh, J. E. Bowers, S. P. DenBaars, and S. Nakamura, J. Appl. Phys. **113** (18), 183707 (2013).
281 D. Nilsson, E. Janzén, and A. Kakanakova-Georgieva, J. of Phys. D: Appl.Phys. **49** (17), 175108 (2016).
282 N. Katcho, J. Carrete, W. Li, and N. Mingo, Phys. Rev. B **90** (9), 094117 (2014).
283 A. Katre, J. Carrete, B. Dongre, G. K. Madsen, and N. Mingo, Phys. Rev. Lett. **119** (7), 075902 (2017).
284 A. Katre, J. Carrete, T. Wang, G. K. Madsen, and N. Mingo, Phys. Rev. Materials **2** (5), 050602 (2018).
285 L. Lindsay, D. Broido, and T. Reinecke, Phys. Rev. B **87** (16), 165201 (2013).
286 A. Togo, F. Oba, and I. Tanaka, Phys. Rev. B **78** (13), 134106 (2008).
287 W. Li, J. Carrete, N. A. Katcho, and N. Mingo, Computer Physics Communications **185** (6), 1747 (2014).
288 G. Kresse and D. Joubert, Phys. Rev. B **59** (3), 1758 (1999).
289 J. Carrete, B. Vermeersch, A. Katre, A. van Roekeghem, T. Wang, G. K. Madsen, and N. Mingo, Computer Physics Communications **220**, 351 (2017).
290 A. Katre, A. Togo, I. Tanaka, and G. K. Madsen, J. of Appl. Phys. **117** (4), 045102 (2015).
291 G. Slack, J. Phys. Chem. Solids **34** (2), 321 (1973).

292   J. P. Freedman, J. H. Leach, E. A. Preble, Z. Sitar, R. F. Davis, and J. A. Malen, Scientific Reports **3**, 2963 (2013).

293   P. N. Martin, Z. Aksamija, E. Pop, and U. Ravaioli, Nano Letters **10** (4), 1120 (2010).

294   J. Carrete, L. J. Gallego, L. M. Varela, and N. Mingo, Phys. Rev. B **84** (7), 075403 (2011).

295   J. Tsao, S. Chowdhury, M. Hollis, D. Jena, N. Johnson, K. Jones, R. Kaplar, S. Rajan, C. Van de Walle, and E. Bellotti, Advanced Electronic Materials **4** (1), 1600501 (2018).

296   M. Malakoutian, M. A. Laurent, and S. Chowdhury, Crystals **9** (10), 498 (2019).

297   T. Izak, O. Babchenko, V. Jirásek, G. Vanko, M. Vojs, and A. Kromka, presented at the Materials Science Forum, 2015 (unpublished).

298   E. Chávez-Ángel, J. S. Reparaz, J. Gomis-Bresco, M. R. Wagner, J. Cuffe, B. Graczykowski, A. Shchepetov, H. Jiang, M. Prunnila, and J. Ahopelto, APL Materials **2** (1), 012113 (2014).

299   G. S. Doerk, C. Carraro, and R. Maboudian, Physical Review B **80** (7), 073306 (2009).

300   S. Choi, E. R. Heller, D. Dorsey, R. Vetury, and S. Graham, IEEE Transactions on Electron Devices **60** (6), 1898 (2013).

301   T. Beechem, A. Christensen, S. Graham, and D. Green, Journal of Applied Physics **103** (12), 124501 (2008).

302   K. Sarkar, D. Datta, D. J. Gosztola, F. Shi, A. Nicholls, M. A. Stroscio, and M. Dutta, Superlattices and Microstructures **115**, 116 (2018).

303   E. Yalon, S. Deshmukh, M. M. Rojo, F. Lian, C. M. Neumann, F. Xiong, and E. Pop, Scientific reports **7** (1), 1 (2017).

304   E. Ziade, J. Yang, G. Brummer, D. Nothern, T. Moustakas, and A. J. Schmidt, Appl. Phys. Lett. **110** (3), 031903 (2017).

305   C. H. Henager and W. Pawlewicz, Applied optics **32** (1), 91 (1993).

306   H.-F. Lee, S. Kumar, and M. A. Haque, Acta materialia **58** (20), 6619 (2010).

307   Z. Li-Dan, S. Fang-Yuan, Z. Jie, T. Da-Wei, L. Yu-Hua, and G. Chao-Hong, Chinese Physics Letters **29** (6), 066301 (2012).

308   J. Lugo and A. Oliva, Journal of Thermophysics and Heat Transfer **30** (2), 452 (2016).